Thèse n° 9097

Heterostructure design and field management in III-N high-electron mobility electronic devices

Présentée le 29 octobre 2021

Faculté des sciences et techniques de l'ingénieur
Laboratoire de dispositifs semiconducteurs de puissance
Programme doctoral en microsystèmes et microélectronique

pour l'obtention du grade de Docteur ès Sciences

par

Catherine ERINE

Acceptée sur proposition du jury

Prof. E. Charbon, président du jury
Prof. E. D. N. Matioli, directeur de thèse
Prof. H. G. Xing, rapporteuse
Dr P. Moens, rapporteur
Prof. N. Grandjean, rapporteur

École
polytechnique
fédérale
de Lausanne

2021

If you have just measured a new physical phenomenon,
check the connection of the wires in your experimental setup.
— Vyacheslav Safarov

To all my teachers.....

Acknowledgements

First, I would like to thank Prof. Matioli for giving me the possibility to perform research in such an exciting field. His patience and optimism have helped me a lot through this difficult journey.
I would also like to thank Prof. Xing, Prof. Grandjean, Dr. Moens and Prof. Charbon for their time and attention dedicated to the revision of this thesis.
I would like to thank all the staff of CMi EPFL, iPHYS and CIME EPFL for all the help with clean room fabrication and characterization.
A great thanks goes to all my colleagues. In particular, I would like to thank our best secretary in the world, Muriel Bardet, for her immediate help in all possible questions concerning the survival of a PhD student in wild mountains of administrative papers. Then I would like to express all my appreciation to Giovanni Santoruvo who guided me and taught me everything about fabrication and measurements and was always ready to discuss and to help. I would like to thank Jun Ma for his practical engineering mind that taught me to be efficient and get the most of what you have. A special great thanks goes to Luca Nela for all the collaborations and endless discussions in search of the semiconductor-physics truth. It was a great pleasure and immense enriching experience to work with you. I am also extremely grateful to Remco van Erp for all the mechanical engineering he performed for me and all the discussions we had. And I would also like to thank all other people in our lab: Nirmana Perera, Minghua Zhu, Armin Jafari and Georgios Kampitsis for their help and fun time spent together.
I would also like to thank people who created a passion for physics and mathematics in my heart: my school physics teacher, Nafisa Koumacheva, my bachelor's thesis supervisor, Maria Skopina, my internship supervisors Henri Jaffrès, Henri-Jean Drouhin, Vyacheslav Safarov and Claude Weisbuch.
Finally, I would like to thank all my family for always supporting me in whatever I do.
And I don't forget to thank my boyfriend Pavel Yazhgur for all his patience in proofreading my papers and for all the physics discussions we had. That helped me to form a fresh view of my domain and develop a broad interdisciplinary vision of basic physics principles.

Lausanne, 26 Juillet 2021 Catherine Erine

Abstract

III-N family of materials has offered multiple groundbreaking technologies in the field of optoelectronics and high-power radio-frequency (RF) devices. Blue light-emitting diodes (LEDs), recompensed by the 2014 Nobel Prize, have revolutionized low-energy lighting. Gallium nitride (GaN) RF market is projected to reach 2 billion US$ by 2025, driven by the defense and telecom applications (namely, 5G).

Since a few years, a relatively new field of GaN power electronics is actively growing and just entering the consumer market. The main applications are fast smartphone chargers, automotive, data center, and aerospace. GaN high-electron-mobility (HEM) transistor (HEMT) is the major GaN-based power device commercially available nowadays.

The high breakdown field of GaN together with the enhanced mobility offered by the high-electron-mobility heterostructure offer numerous advantages over existing Si-based devices. GaN HEMTs are significantly smaller than their Si counterparts and, thus, switch faster. Increased switching frequency allows to drastically reduce the converter size as well as switching power loss. Thus, GaN-based power devices pave the way to future efficient power conversion technologies.

Multi-channel III-N heterostructures are the next step towards the ultimate optimization of a GaN HEMT. By vertically stacking multiple HEM channels one can significantly reduce the ON-resistance of the devices without sacrificing their voltage blocking performance, thus, surpassing the fundamental trade-off between ON-resistance and breakdown voltage.

In this thesis, we present a detailed analysis of the design principles of multi-channel high electron mobility heterostructures. We provide analytical tools allowing to fine-tune carrier concentrations in each of the multiple channels of the vertical stack to achieve the optimal carrier distribution profile for a given application.

Based on the analysis presented and previous ideas in the literature, we develop a novel device concept - intrinsic polarization super-junction (iPSJ) diode. By performing the detailed numerical and theoretical study of its properties we demonstrate that single-channel iPSJ fully decouples the ON-state conductivity from the OFF-state, alleviating the trade-off between the ON-resistance and breakdown voltage, yielding the ultimate optimization of the OFF-state field profile. Moreover, we apply the same concept to a multi-channel (MC) stack. We propose MC-iPSJ devices that surpass the existing GaN HEMT material limit. An extensive study of the physical principles behind the proposed devices allows us to propose a robust platform

compatible with current commercial fabrication techniques.
Furthermore, a multi-channel stack requires special 3D gating techniques to provide efficient gate control. Gate and access regions have to be patterned with nanowires to ensure efficient depletion by the gate and optimal field distribution in the access region. We perform a thorough experimental and analytical study of electrical properties of top-down etched GaN HEMT nanowires that shed light on the strategies to achieve normally-off behavior and optimize the passivation of tri-gated HEMTs.
Finally, we explore an alternative gating technique for the multi-channel stack - in-plane gate (IPG). In-plane gate offers advantages in terms of gate capacitance and can be potentially used for high-frequency RF applications. However, a single-channel IPG transistor is difficult to upscale due to the parasitics involved. We experimentally demonstrate a multi-channel in-plane gate transistor being 3.5-times more conductive than its single-channel counterpart, thus, opening the way to the up-scaled IPG-FET.
This thesis presents a complete overall study of multi-channel heterostructures, along with specific field-management and gating techniques required for this new technology. The experimental results and analytical tools presented provide a solid basis for the future optimization of MC-HEMTs.

Key words: GaN, HEMT, III-Nitride, Nanowires, In-plane gate, Polarization Super Junction

Résumé

La famille des matériaux III-N a offert de multiple technologies révolutionnaires dans les domaines de l'optoélectronique et de l'électronique de haute fréquence (HF) à haute puissance. La diode électroluminescente bleue, récompensée par le prix Nobel 2014, a révolutionne l'éclairage à faible consommation. Le marché des transistors haute fréquence à base de nitrure de gallium (GaN) est projeté d'atteindre 2 milliards de dollars à 2025, propulsé par les applications de défense et de télécommunications (en particulier, 5G).

Depuis quelques années, un domaine relativement nouveau de l'électronique de puissance à base de GaN est en pleine croissance et entre le marché de consommateurs. Les applications principales sont chargeurs de portable rapides, automobiles, centres de data et l'aérospatial. Le transistor à électrons à haute mobilité à base de GaN (GaN HEMT) est la principale composante de puissance à base de GaN sur le marché. Le champ de claquage élevé de GaN, ensemble avec la mobilité supérieure offerte par la structure à électrons à haute mobilité, offrent de nombreux avantages sur les composantes à base de silicium (Si). GaN HEMTs sont considérablement plus petits que leurs homologues à base de silicium, ce qui permet de commuter à une fréquence plus élevée. L'augmentation de fréquence de commutation réduit substantiellement la taille des convertisseurs et les pertes. Ainsi, les composantes de puissance à base de GaN ouvrent la voie à la future électronique pour la conversion d'énergie efficace.

Les hétérostructures III-N à multiple chenaux à haute mobilité présent le prochain pas vers l'optimisation ultime des GaN HEMTs. En stockant verticalement multiple chenaux à haute mobilité, il est possible de réduire considérablement la résistance en l'état ON sans sacrifier les performances en état OFF, ainsi surpassant le compromis fondamental entre la résistance dans l'état ON est la tension de claquage.

Dans cette thèse, nous présentons une analyse détaillée de principe de design des hétérostructures à électrons à haute mobilité à multiple chenaux. Nous fournissons les outilles analytiques de l'ajustement précis des concentrations des porteurs dans chaqun de multiples chenaux en vue d'obtenir la distribution des porteurs optimale pour une application désirée.

En se basant sur notre analyse ainsi, que les idées présentes dans la littérature, nous développons une nouvelle conception d'une composante – la diode intrinsèque à super jonction à base de polarisation (iPSJ). En performant une étude numérique et théorique approfondie de ses propriétés, nous démontrons que iPSJ à seul chenal découple la conductance en l'état ON de l'état OFF, ainsi enlevant la compromise entre la résistance dans l'état ON est la

tension de claquage, fournissant l'optimisation ultime du profile de champ électrique dans l'état OFF. De plus, nous appliquons le concept d'iPSJ à l'hétérostructure à chenaux multiples. Nous proposons des iPSJ à chenaux multiples qui surpassent la limite actuelle de GaN HEMT. Une étude approfondie des principes physiques à la base des composantes proposées, nous permet de proposer une plateforme robuste, compatible avec les techniques de fabrication commerciales existantes.
En outre, les hétérostructures à chenaux multiples exigent des techniques de grillage 3D spécifiques afin d'assurer le contrôle efficace des chenaux par la grille. Les régions d'accès et de la grille doivent être composées de nanofils afin d'assurer le contrôle efficace par la grille ainsi que la distribution de champ optimale dans l'état OFF. Nous performons une analyse expérimentale et analytique des propriétés électriques de nanofils GaN HEMT, ce qui met en évidence les stratégies pour achever le comportement normalement-OFF et pour optimiser la passivation des GaN HEMT à grille 3D.
En plus, nous explorons les techniques de grillage des hétérostructures à chenaux multiples alternatives – la grille dans le plan. La grille dans le plan offre des avantages au niveau de capacité de grille et est potentiellement intéressante pour les applications haute fréquence. Cependant le transistor à grille dans le plan à chenal unique est difficile de fabriquer en dimensions pratiques à cause des contributions parasites. Nous démontrons expérimentalement un transistor à grille dans le plan à chenaux multiples qui possède la conductivité 3.5 fois plus élevée que son homologue a chenal unique, ainsi ouvrant la voie vers les transistors à grille dans le plan avec les dimensions pratiques.
Cette thèse présente une étude complète et approfondie des hétérostructures à chenaux multiples, ainsi que des techniques de grillage et de gestion de champ électrique dans l'état OFF, exigés par cette nouvelle technologie. Les résultats expérimentaux et les outilles analytiques présentés donnent une base solide au futur développement des composantes à électrons à haute mobilité à multiples chenaux.

Mots clefs : GaN, HEMT, III-Nitride, Nanofils, Grille dans le plan, Super jonction à base de polarization

Contents

List of Figures

List of Tables

1 Introduction

1.1 Why III-N semiconductors?

III-N family of materials (GaN, AlN, InN, and their alloys) has offered multiple groundbreaking technologies in the field of optoelectronics and high-power radio-frequency (RF) devices. Blue light-emitting diodes (LEDs), recompensed by the 2014 Nobel Prize, have revolutionized low-energy lighting [1]. GaN RF market is projected to reach 2 billion US$ by 2025, driven by the defense and telecom applications (namely, 5G) [2].

Compared to mature and established optoelectronics and RF markets, GaN for power electronics is a relatively new field, actively growing and just entering the consumer market since few years. However, the GaN power market is already expected to reach 1.1 billion US$ by 2026 (Fig. 1.1). The main applications are fast smartphone chargers (Power Integration, Navitas), automotive (Texas Instruments), data center, and aerospace (EPC, Infineon, Transphorm) (Fig. 1.2) [3].

GaN family materials offer certain advantages over the universally used Si and the main power electronics material SiC for mid-range power applications (Table 1.1).

A large bandgap (E_g) of 3.39 eV compared to 1.1 eV for Si yields a critical electrical field (E_{BR}) of 3.3 MV/cm vs 0.3 MV/cm for Si [4] : more than 10-times increase! This means that one needs less than 10 times of material thickness to hold the same voltage in the off-state, reducing the drift region length and, thus, device resistance in the on-state (Si and GaN mobilities are similar [4]). Although SiC has very similar E_g and E_{BR} (3.26 eV and 3.0 MV/cm correspondingly), GaN can offer higher electron mobility, especially, in lateral devices, employing two-dimensional electron gas (2DEG). Altogether, high critical field and good electron mobility allows GaN as a material to surpass Si (~ 900x) and SiC (~ 400x) in terms of Baliga's figure-of-merit (FoM) - one of the main power transistor FoMs that reflects the fundamental trade-off between R_{on} and V_{br} (Fig. 1.3, Table 1.1).

A larger critical field for the same on-resistance enables the downsizing of GaN-based devices,

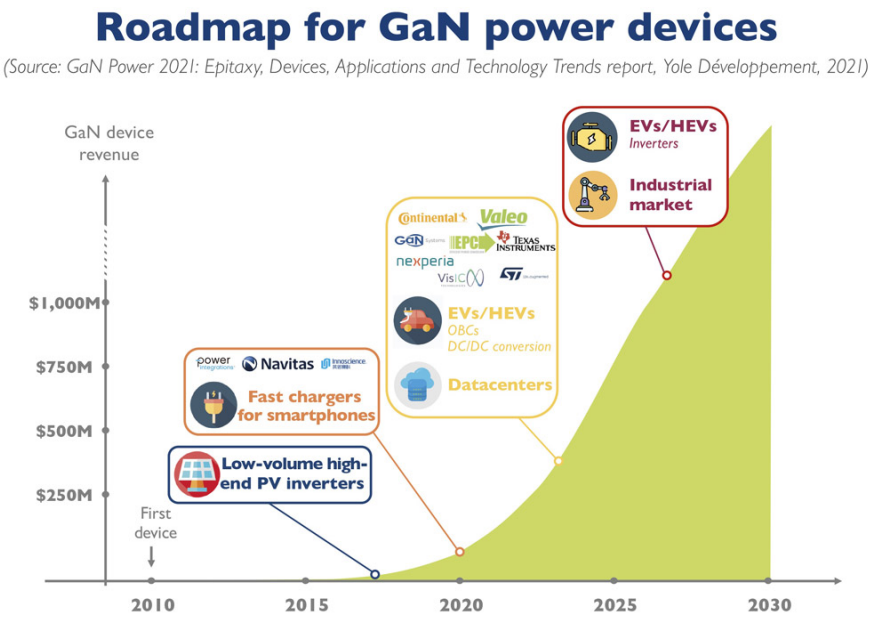

Figure 1.1 – Roadmap for GaN power devices [3]

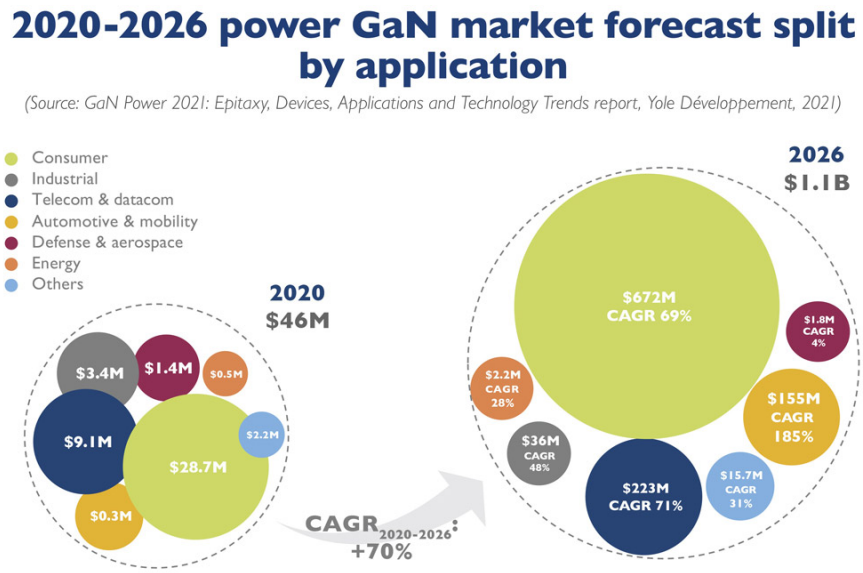

Figure 1.2 – GaN power electronics market forecast split by application [3]

Table 1.1 – Material properties of Si, SiC and GaN [4]

Material	E_g [eV]	E_{BR} [MV/cm]	μ [cm^2/V·s]	ϵ [1]	BFoM [BFoM (Si)]
Si	1.1	0.3	1350	11.8	1
SiC	3.26	3.0	700	10	439
GaN	3.39	3.3	1200 (bulk) 2000 (2DEG)	9	902

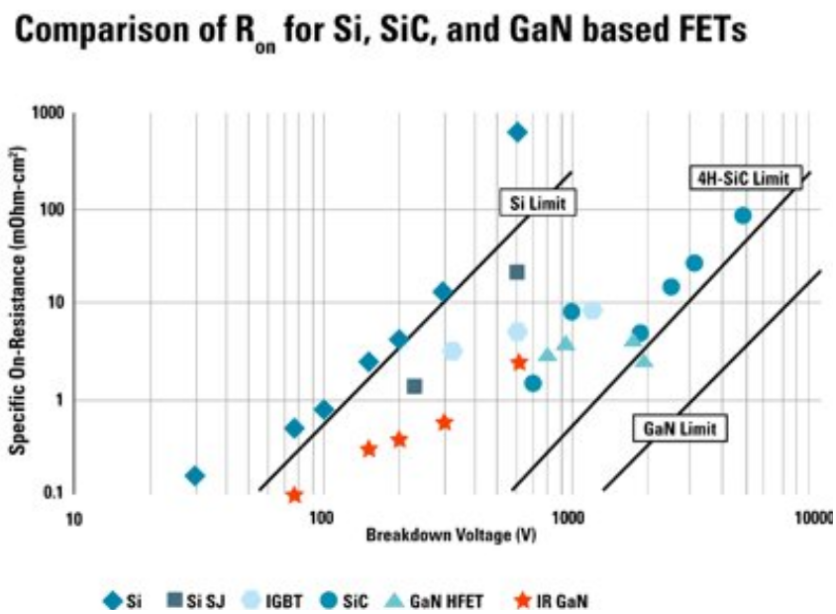

Figure 1.3 – GaN material limit in on-resistance vs breakdown trade-off is beyond Si and SiC. However, while Si devices are already at the theoretical limit, there is still a lot of room for improvement for GaN electronics. [5]

which, combined with the possibility to employ HEMT rather than MOSFET or JFET junction device architectures, leads to the increase in switching frequency (Fig. 1.4). Increased switching frequency in its turn allows shrinking the inductor size (usually, the biggest element of a converter), making GaN-based converters lighter and smaller (Fig. 1.4 (inset)). This makes GaN very attractive for automotive and airspace applications where size and weight play a crucial role. On the other side, if the size is not important, GaN can offer lower switching loss compared to Si at a given frequency (Fig. 1.4), thus, reducing the energy losses and making GaN technologies attractive for data center power supplies.

All those properties define GaN technology as the optimal one for medium power, high switching frequency power electronics applications (Fig. 1.5).

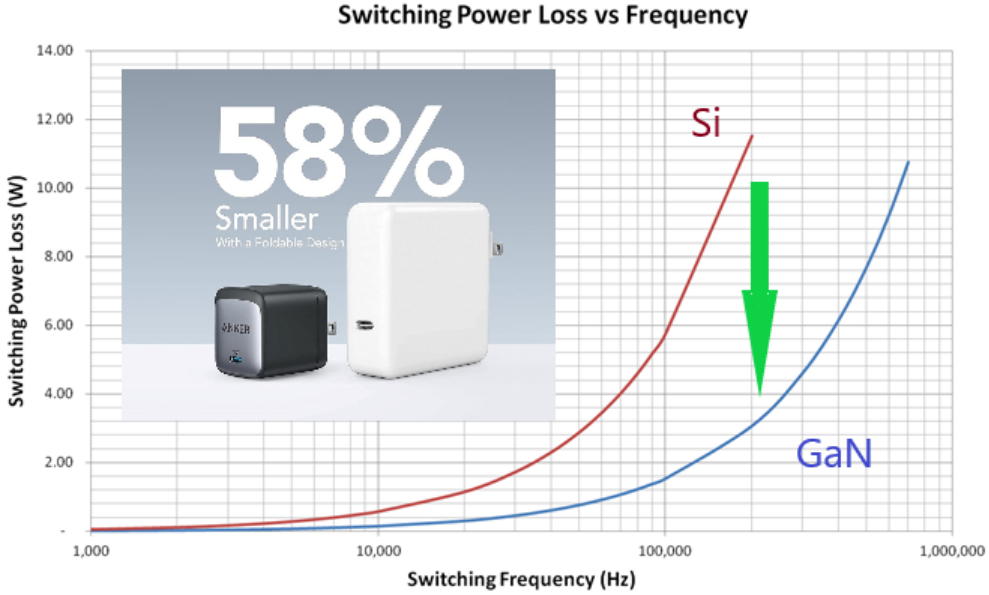

Figure 1.4 – Lower switching loss allows for switching frequency increase, yielding reduction in inductance necessary for converters and drastically reducing the converter size. [6] Inset: commercially available GaN-based charger from Anker 58% smaller than its Si-based counterpart. [7]

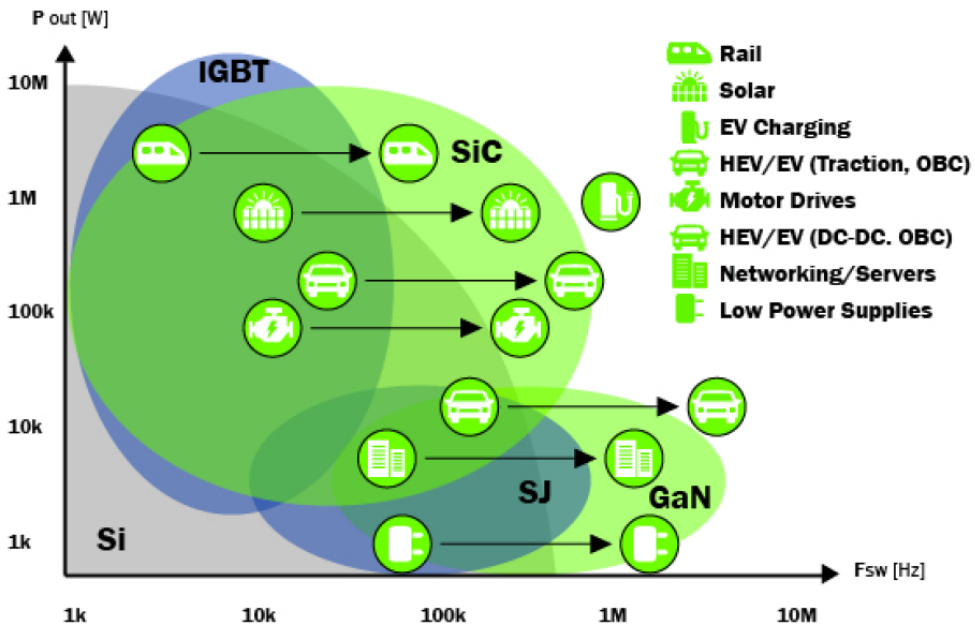

Figure 1.5 – Main application field of GaN power electronics is small size (= high-frequency switching) medium power converters for low power supplies, data centers and electric vehicle applications. [8]

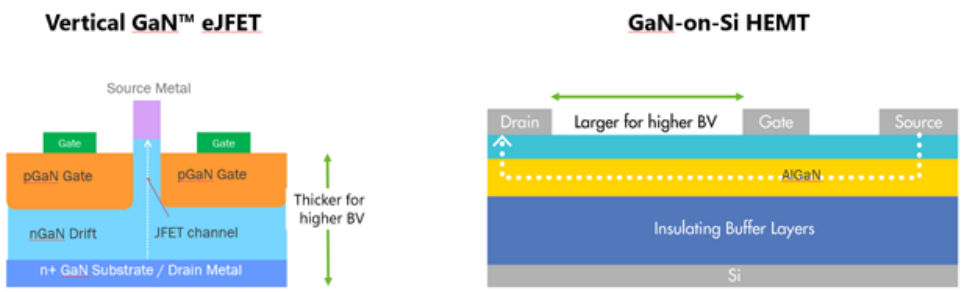

Figure 1.6 – Left: Vertical device (JFET) the drift region is determined by maximum epitaxy thickness; Right: lateral HEMT drift region length is determined by the gate-to-drain distance (L_{gd}), provided high enough buffer breakdown [9]

1.2 Why High-electron Mobility Transistors (HEMTs)?

Although GaN offers advantages over Si and SiC from the material point of view, even if usual vertical transistor architectures (JFET, trench MOSFET, CAVET) are employed, there is a practical limit in material quality and cost that hinders the full potential of usual vertical or quasi-vertical GaN devices. Native GaN substrates are very costly and limited in size, thus, foreign substrates are used for epitaxy (sapphire, silicon, silicon carbide). All of them present thermal and lattice mismatches with GaN, limiting the total thickness of epitaxial layers. Moreover, the best choice - SiC - is still costly and is usually employed in RF devices where the margin is higher and cost reduction is less important. In such a low-margin market as power electronics, one is mostly left with silicon and sapphire substrates that are cheap and large (up to 8 inches nowadays). Moreover, silicon is often preferred to sapphire due to its thermal properties and the possibility to ground the substrate. The absence of native substrates and restrictions on total epitaxy thickness pose limits on fully vertical transistor design. The drift region, which holds most of the voltage drop in the off-state, is restrained to few microns for vertical GaN-on-Si, reducing the maximum possible voltage rating.

However, the GaN family offers a unique (compared to Si and SiC) alternative to vertical architecture - a lateral device based on a heterojunction between GaN and a wider bandgap III-N (AlGaN, InAlN)- high electron mobility transistor (HEMT). In a HEMT the conduction occurs through a thin layer at the interface between the barrier (wider bandgap: AlGaN, InAlN) and the channel (narrower bandgap: usually, GaN) - a thin dense layer of highly mobile electrons called two-dimensional electron gas (2DEG). The length of the drift region is defined by the gate-drain distance (L_{gd}) which could, in principle, be as long as needed, contrary to vertical devices where epitaxial growth sets a practical limit of just a few microns (Fig. 1.6). High ($\sim 10^{13}$ cm^{-2}) sheet carrier concentration (N_s) in the 2DEG along with high ($\sim$ 2000cm^2/V$\cdot$s) electron mobility (μ) of this layer yields low ($\sim 300\ \Omega/\square$) sheet resistance (R_{sh}) and ,thus, low on resistance (R_{on}, typically, $6-10\ \Omega\cdot$mm).

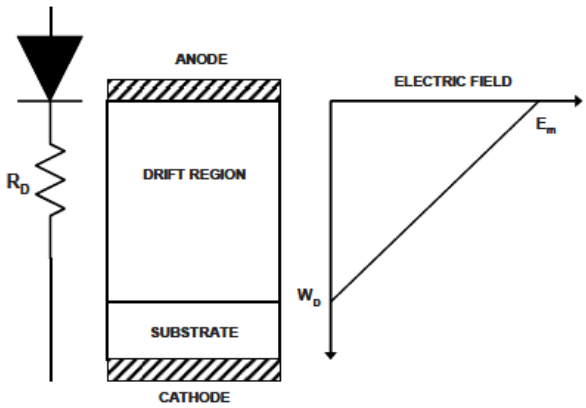

Figure 1.7 – Ideal uniformly doped drift region of a unipolar device and field distribution inside it [10]

In practice, L_{gd} can not be too long for lateral GaN-on-Si as the vertical breakdown of buffer layers limits the high-voltage performance of GaN HEMTs on Si to ~ 2000 V (grounded substrate), which is still higher than experimentally demonstrated (quasi) vertical GaN-on-Si devices (< 1000 V). Up to now, GaN HEMTs outperform their vertical counterparts on cost-effective Si substrates in terms of maximum achievable operation voltage and all commercial Ga-on-Si devices are HEMTs.

This thesis is focused on novel GaN HEMT heterostructures and device architectures for power electronics applications.

1.3 Trade-off between $R_{on,sp}$ and V_{br}: Baliga's Figure-of-Merit

To minimize conduction losses, a good power device should have low resistance in the on-state. On the other hand, it should be able to block high voltage when off. Unfortunately, those two requirements are mutually contradicting. To lower the resistance one would like to shorten the drift region. To enhance voltage blocking performance, on the contrary, one would like the voltage drop in the off-state to occur through a longer distance, thus, to increase the drift region length. To increase the conductivity one dopes more. However, the maximum field in the off-state increases with doping, decreasing the breakdown voltage. To quantify those trade-offs B. Jayant Baliga derived the following expression linking the specific on-resistance (resistance of unit area of the device on the wafer face, $R_{on,sp}$ [$\Omega \cdot \mathrm{cm}^2$]) to breakdown voltage (V_{br} [V]):

$$\frac{V_{br}^2}{R_{on,sp}} = \frac{\epsilon_s \mu_n E_C^3}{4} \tag{1.1}$$

where ϵ_s is permittivity of the semiconductor, μ_n - electron mobility, E_C - critical field. This expression is valid for an ideal uniformly doped drift region of a unipolar device (with any

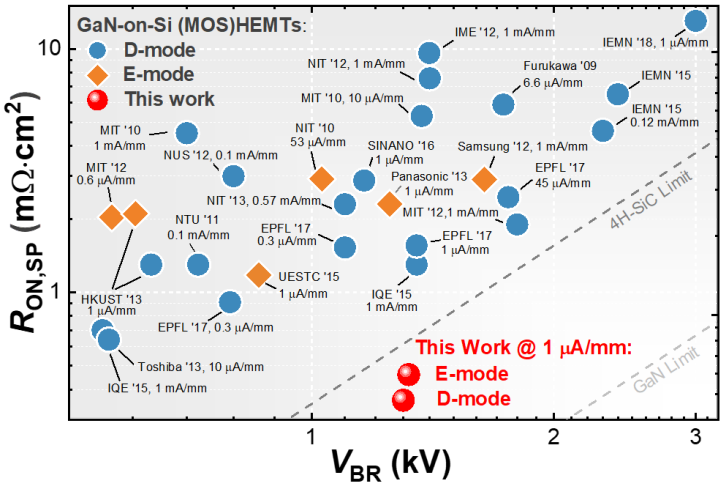

Figure 1.8 – Benchmark of GaN-on-Si HEMTs as of 2020: all the devices are still far from the theoretical limit [11]

doping N_D, see Fig. 1.7). The denominator of the right side is a material dependant constant (independent of doping) which is usually referred to as Baliga's figure of merit (FoM) for power devices [10]. It reflects the fundamental limitation in reduction of $R_{on,sp}$ of a device for a given breakdown voltage and sets material limits in Fig. 1.3. More detailed understanding of GaN HEMT breakdown voltage versus ON- resistance limit is given in Chapter 3.

However, one can see that most of current GaN devices, contrary to Si ones, are still far from the GaN material limit, leaving a lot of room for research and improvement (Fig. 1.3, Fig. 1.8). Correct understanding of the $R_{on,sp}$ vs V_{br} trade-off for a given device type and architecture is necessary to understand the mismatch between expected (theoretical) behavior and the one observed in real devices.

A big part of this thesis is dedicated to understanding the limits of GaN HEMT, examination of the origin of the mismatch between theoretical and real device performances, proposing strategies to approach the theoretical limit as well as exploration of possible ways around it.

1.4 Reduction $R_{on,sp}$ for a given V_{br} : multi-channel HEMT

The first approach to cross the limit line is to make a more conductive heterostructure with the same breakdown. One could achieve that by putting multiple devices in parallel without changing the footprint: the voltage drop on each of them would be the same while the resistance would be divided by the number of devices. While for vertical architecture this is geometrically impossible, in a HEMT structure one can vertically stack multiple parallel 2DEG channels by employing several periods of barrier/channel(Fig. 1.9), thus, enhancing conductivity within the same footprint. Such multi-channel heterostructures and devices based on them (MC-HEMT) are studied in details in this thesis. An extensive analytical,

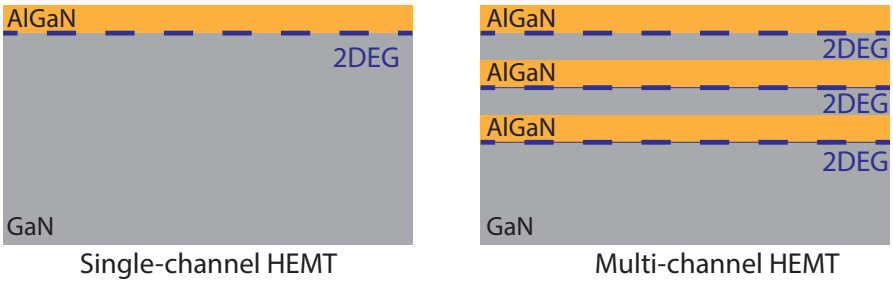

Figure 1.9 – Left: Single-channel HEMT Right: Multi-channel HEMT obtained by stacking multiple periods of barrier/channel in parallel within the same footprint

numerical and experimental study is presented and general design rules for a stack with given properties are proposed.

Although the integration of multiple channels to increase the conductivity seems to be quite obvious, the exact design of the device is more complicated. Indeed, a usual top gate won't be able to efficiently and simultaneously control all the channels. Thus, novel 3D gating techniques (tri-gate, in-plane gate) are required. All of those techniques imply etching nanowires (nanoribbons) in the gate area in such a way that the side gate contributes to the 2DEG depletion.

Moreover, classical field management strategies (planar field plates) fail in such devices. The gate-drain region has to be patterned by top-down-etched nanowires acting as 3D field-plates in order to prevent the premature breakdown.

Finally, normally-off behavior is desired for a power transistor. The transistor should be off when the gate is grounded so that there is no danger of a short path in the circuit in case of power supply failure. GaN HEMTs are intrinsically normally-on devices, as one has to apply negative gate voltage to deplete the 2DEG and turn off the transistor. While for single channel HEMTs it is possible to adjust the heterostructure or to make a recess under the gate (MOS-HEMT) in order to get a more positive threshold, for MC-HEMTs the easiest option is to fine-tune the nanowire width under the gate, adjusting the lateral depletion.

Hence, most of the properties of a multi-channel HEMT (MC-HEMT, Fig. 1.10) are governed by nanowires. Multi-channel power HEMT is necessarily a nanowire patterned HEMT. A detailed study of various physical properties (carrier concentration, mobility, temperature behavior) of top-down etched single- and multi-channel AlGaN/GaN HEMT nanowires is presented in this thesis. Particular attention is paid to the link between nanowire physical properties and resulting applications in different parts of the device.

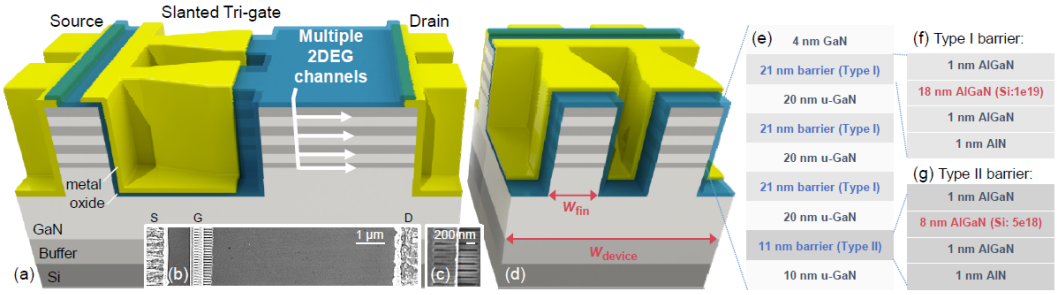

Figure 1.10 – Schematics of a typical multi-channel power HEMT with nano-patterned gate, access and contact regions (a); Top SEM overview (b); SEM zoom into the gate area (c); 90 degree turned schematics (d); one of possible multi-channel heterostructures (e) [12]

1.5 Increase of V_{br} for a given $R_{on,sp}$: super-junction-like HEMT

One of the main reasons for the premature breakdown in HEMTs is a non-uniform field distribution in the gate-drain area. In a typical HEMT, electric field peaks at the edge of the gate (or at the edge of the last field-plate). If one could achieve a uniform (ideal) or at least linear field distribution in the gate-drain region, the device breakdown would increase, as the maximum value of the field for a given voltage drop would decrease (see Fig. 1.11).

To achieve a uniform field distribution one could use a super-junction-like device where all the charges in the drift region are balanced in the off state, the drift region is neutral on average, and the field is constant. A small imbalance can be tolerated, leading to a linear field profile (provided the uniform distribution of the imbalance charges). Exact requirements on the heterostructure design in order to achieve the super junction behavior are studied in this thesis and a novel, robust platform for such devices, called intrinsic polarization super junctions (iPSJ-HEMT), is proposed.

Finally, iPSJ-HEMT concept can be applied to multi-channel structures, leading to ultimate op-

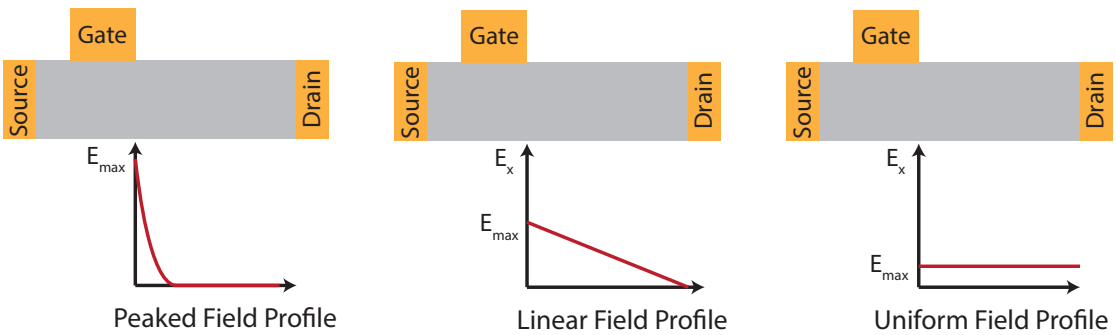

Figure 1.11 – Left: typical field profile in a HEMT; Middle: linear filed; Right: uniform field. For the same voltage drop (surface under the graph) the maximum field decreases from left to right.

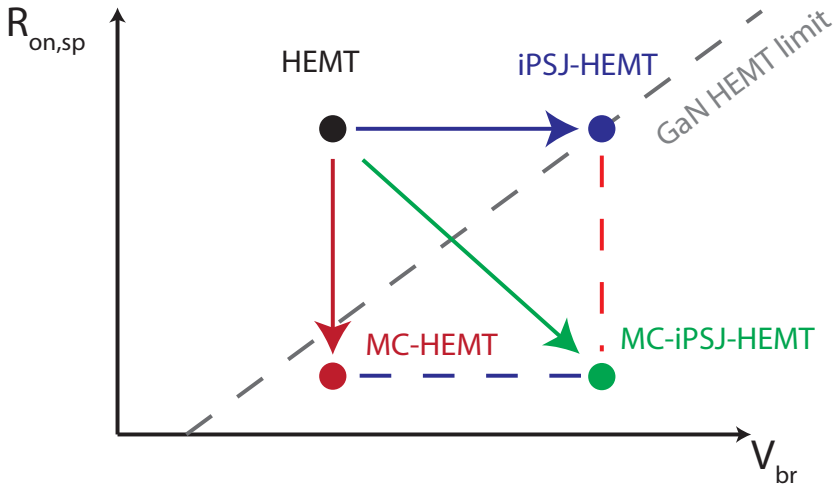

Figure 1.12 – $R_{on,sp}$ vs V_{br} trade-off: MC-HEMT allows to decrease the on resistance for the same voltage; iPSJ-HEMT offers a better breakdown for a given $R_{on,sp}$; combining the two one gets an MC-iPSJ-HEMT that approaches the most the ideal desired behavior of a power device, potentially breaking the GaN HEMT limit

timization of the field and resistance simultaneously, potentially breaking what is considered GaN HEMT limit by employing a MC-iPSJ-HEMT (see Fig. 1.12).

1.6 Thesis outline

In the second chapter, I present design principles of multi-channel heterostructures. Using an analytical model developed during this thesis, we define the main working principles of a MC-HEM heterostucture and highlight the strategies to achieve high-conductivity channels stacks with specific properties (even carrier distribution, charge balance).

In the third chapter, intrinsic polarization super junction devices based on charged balanced SC- and MC-HEM stacks are discussed. Those structures present optimal field management strategies leading to devices with fully decoupled off- and on-states. Such devices break the fundamental trade-off between the on-resistance and breakdown voltage.

The fourth chapter is dedicated to electronic transport in single- and multi-channel nanowires. Experimental values of sheet resistance, carrier concentration, and mobility in single- and multi-channel nanowires are presented. The results obtained contribute to the optimization of the design of MC-HEMTs. A model explaining the low-temperature behavior of carrier concentration in nanowires is proposed and validated.

The fifth chapter shows an alternative gating technique for MC-HEMTs - in-plane-gate and a device based on it - in-plane-gate field-effect transistor (IPGFET). IPGFET offers an interesting alternative to conventional gating techniques, offering a reduced gate capacitance, important

for high-frequency applications.

2 Multi-channel heterostructures

In this chapter, we will consider design principles of high-electron-mobility (HEM) III-N heterostructures with a given carrier concentration. First, I present a general overview of the stacks described in the literature. Working principles of a HEM heterostructure are reviewed in detail to avoid any further misunderstanding, especially as to the origin of electrons in 2-dimensional electron gases in single- and multi-channel heterostructures. Then, I present a simple physics-based analytical model providing carrier concentrations in each channel of a multi-channel HEM stack, along with its numerical and experimental validation. Finally, the properties of the multi-channel HEM structures along with design principles of the channel stack are derived from the model.

This model, developed during my thesis, constitutes an important analytical tool to analyze the behavior of multi-channel HEM wafers. The carrier concentration profile in a given stack geometry can be found quickly and efficiently using modern simulation tools. However, the inverse problem of designing a multi-channel stack with a given carrier distribution requires tedious and time-consuming multi-parameter optimization if solved purely numerically. Thus, a simple enough analytical tool shedding the light on the main trends allows to greatly restrict the optimization space. For the vast majority of III-N materials and geometries that are feasible nowadays, our model offers 10 to 25% error if no free parameters are used and 2% error when one material-only dependent fit parameter with a clear physical and mathematical meaning is employed.

2.1 State-of-the-art

Currently, several III-N multi-channel heterostuctures have been described in the literature. Materials employed are AlGaN/GaN, InAlN/GaN, and AlN/GaN with or without doping in the barrier/channel. Sheet resistances down to 37 Ω/□ have been demonstrated [15].

AlN/GaN structure offers the best ratio of the channel stack thickness to sheet resistance. However, high-mobility AlN/GaN multi-channel structures are very challenging to grow on

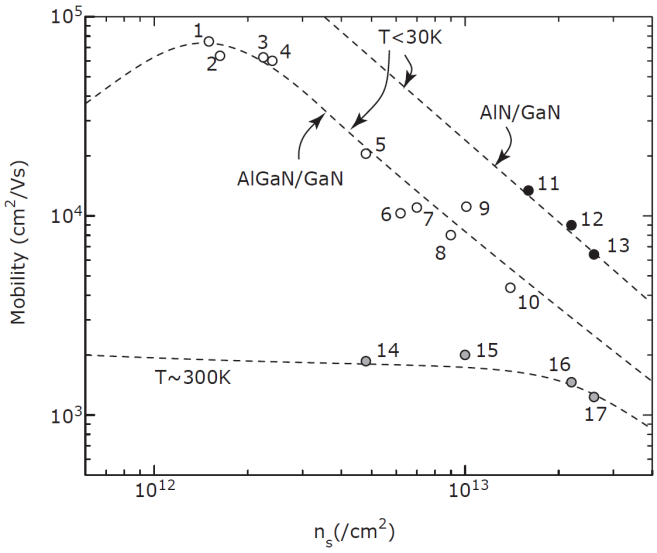

Figure 2.1 – Mobility (μ) vs carrier concentration (N_s) for various single-channel structures. Both at room and at low temperature mobility drops significantly for $N_s > 2 \cdot 10^{13}$ cm^{-2} [13].

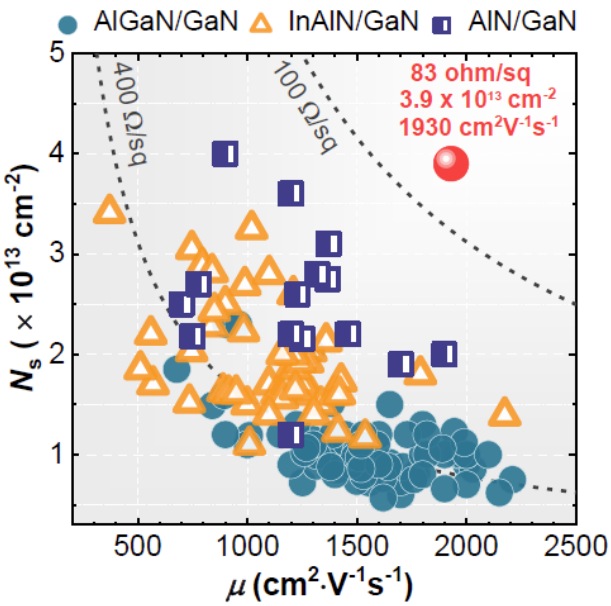

Figure 2.2 – Typical 5-channel AlGaN/GaN wafer [14] compared to different single-channel structures available in literature. Hugh-carrier concentration is obtained without mobility loss.

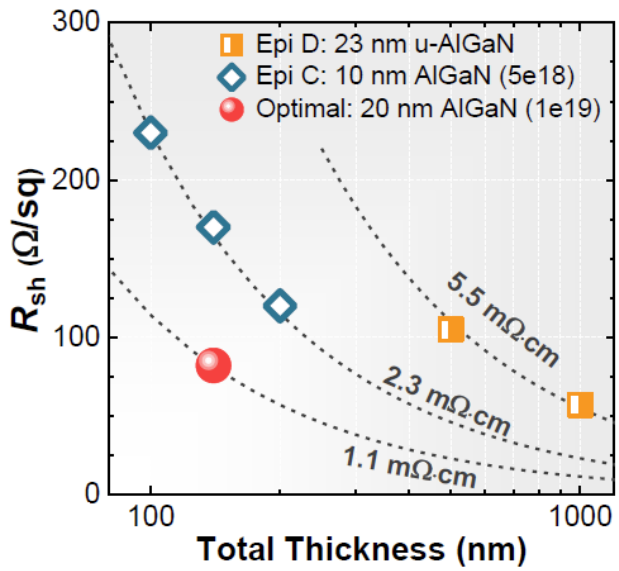

Figure 2.3 – Different doped (blue and red) and undoped (yellow) AlGaN/GaN multi-channel structures [14]. Doping is indicated in parenthesis. Doping allows to significantly reduce the total epi thickness for a given sheet resistance.

large cost-effective substrates. And if mobility is not preserved the resulting gain in R_{sh} is significantly decreased.

The main advantage of a multi-channel structure over a highly populated single-channel one is that the former preserves almost the same mobility (as carriers are distributed in multiple "usual" channels). Increasing the carrier density in a single-channel device typically leads to a decrease in mobility (Fig. 2.1). Moreover, in power devices for the same R_{sh} one would always prefer a heterostructure with higher mobility to the one with higher carrier density. Very high ($> 2 \cdot 10^{13}$ cm^{-2}) carrier concentrations in the same channel are difficult to control and usually lead to a premature breakdown. One can clearly see in Fig. 2.2 the advantage of multi-channel wafers over their single-channel counterparts.

When employing AlGaN/GaN without doping, one has to use a relatively large period to populate middle channels, leading to a thicker stack. Up to our knowledge, the best multi-channel heterostructures in undoped AlGaN/GaN reached R_{sh} of 57 Ω/□ [16] but with 1 μm thick period. Too thick stack makes the device processing difficult or even impossible. As mentioned in the introduction, to effectively control all the channels by the gate, one has to etch nanowires under the gate which are usually from tens to hundreds of nanometers wide. If the stack is too thick (>1 μm) the aspect ratio becomes very high and nanowire width is almost impossible to control (due to a slant of the sidewall present during etching). Moreover, such nanoribbons can be extremely fragile. On top of that, a thick stack would crack due to the strain present in AlGaN barrier. However, the last point can be alleviated by employing a

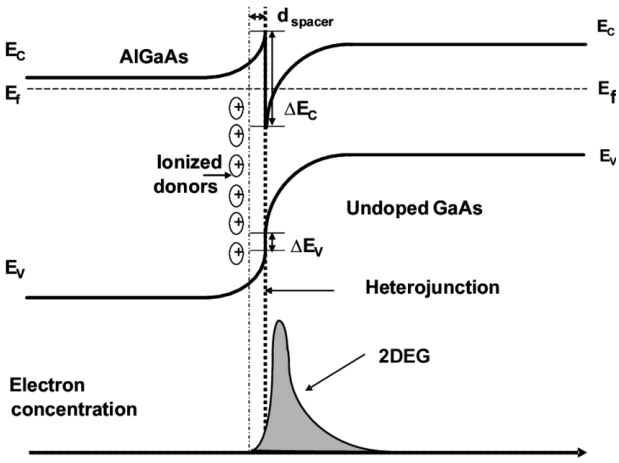

Figure 2.4 – A typical III-V HEMT [29]

nearly lattice-matched InAlN. Typical sheet resistance and thicknesses for doped and undoped AlGaN/GaN stacks can be seen in Fig. 2.3

Currently, the main approach to get a relatively thin, highly conductive multi-channel heterostructure on a large cost-effective substrate is to use doping in the barrier (AlGaN or InGaN) or sometimes in the channel. When doping is present the period thickness can be reduced down to 30 nm for AlGaN/GaN [14] and even down to 14 nm for channel-doped InAlN/GaN HEMT [17] for R_{sh} below 70 Ω/□ as reported in the literature [14].

On the other hand, charge-balanced super-junction-like devices are practically possible only in undoped structures. Thus, both doped and undoped stacks are of interest for modern technologies.

Although multiple experimental heterostructures and devices based on them have been reported in the literature [12], [14], [18]–[28], there is almost no information on the general design rules of the stack: minimal period thickness for a given material, optimal material choice, carrier distribution among the multiple channels of the stack, quantitative role of barrier/channel/cap thicknesses, etc. To fill the gap between available experimental data and a lack of any analytical models for carrier concentrations in each of multiple channels, we have elaborated a simple, still quite precise, analytical model. By employing this model, we could establish a set of design rules for an optimal channel stack with desired properties. The model was verified against simulation and experiment.

2.2 III-N HEMT

2.2.1 What is a usual HEMT?

Before high-quality III-N materials were developed, a typical HEMT used to be a III-V heterostructure (GaAs/AlGaAs, AlInAs/InAs, etc).

The working principle of a classical HEMT is the following. One pseudomorphically (preserving the crystalline structure and having a common lattice constant) grows a wider bandgap (barrier) on top of a lower bandgap (channel) material. Being in contact, both materials have to establish a common Fermi level (chemical potential). However, due to different affinities, a priori Fermi levels in those two materials are not aligned. Thus, a transfer of carriers occurs through the junction and the bands bend, compensating for the initial difference in Fermi levels.

The difference of Fermi levels acts as a quasi-electric field that promotes carrier redistribution. The last continues till the carrier's field compensates the quasi-electric one. As a result, a depletion zone forms in the region that electrons (holes) desert, and an accumulation layer appears on the opposite side. This is a local interface effect, while the whole system stays neutral.

However, if both materials are intrinsic, very few carriers are available in both conduction and valence bands. Accumulation is negligible, Fermi level in the channel at the interface stays well below the conduction band edge, and almost no effect on the conductivity along the interface is observed.

On the other hand, suppose that the barrier is heavily n-doped (see Fig. 2.4), meaning its Fermi level is significantly higher than the channel one. The initial difference between Fermi levels (and thus the quasi-electric field that motivates the electrons to go to the other side) is enhanced. Moreover, a large quantity of mobile carriers is available for transfer. In this situation electrons can form a dense accumulation layer in the channel, leaving a positively charged depletion zone (ionized dopants) in the barrier. This layer is called 2-dimensional electron gas (2DEG). Sheet carrier concentration in the 2DEG in III-V materials is of the order of 10^{12} cm^2. Electrons in this layer are spatially separated from their dopants and are located in the intrinsic channel. This significantly increases electron mobility. One can even leave a small (~1 nm) part of the barrier to be intrinsic (spacer) to further separate mobile electrons from ionized dopants and enhance their mobility. Out of plane, the carriers are confined in a quantum well with discrete energy levels. The layer is so thin that carriers are 2D, meaning they have a constant, energy-independent density of states for a given quantum level, that modifies scattering mechanisms with respect to the 3D case.

To create the 2DEG in a usual HEMT, one has to dope the barrier. Dopants provide electrons for the 2DEG and become positively charged (ionized). The overall structure stays neutral. If metal is added on top of the barrier to form a Schottky gate, the Schottky depletion zone

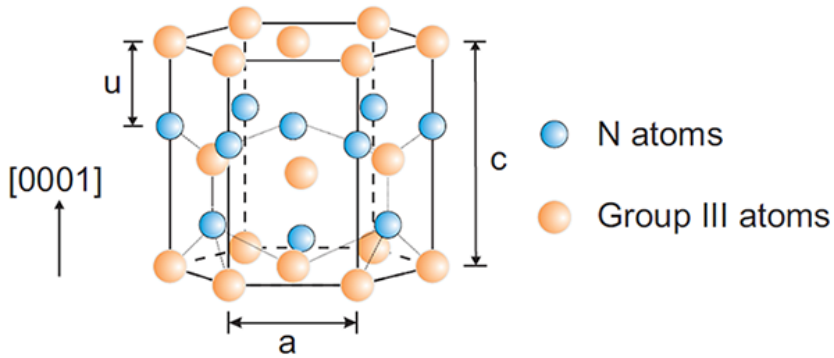

Figure 2.5 – III-N crystal structure [30]

forms in the top part of the barrier (metal gets the corresponding negative charge). In any case the overall structure still stays neutral. In a well-designed barrier, both depletion zones should merge so that no mobile carriers are left in the barrier and the gate can directly control the 2DEG density.

III-N HEMT has a very similar working principle with a 2D sheet of highly mobile electrons confined in a triangular quantum well at the barrier/channel interface. However, it can function without doping in the barrier thanks to polarization present in III-N materials (see further). Nonetheless, it is very important to highlight that, though, no doping is required in a III-N HEMT, the device should always stay overall neutral. Thus, if the 2DEG is formed at the interface, there should be somewhere an equal amount of positive charge. As we will see further in a III-N HEMT there are several possible sources of the 2DEG electrons and several possible origins of the corresponding positive charges. Knowledge of the provenance of the electrons in the 2DEG is crucial to understand the off-state and time-dependent on-state behavior of a III-N HEMT.

2.2.2 III-N crystalline structure and Polarization

III-N crystals usually have a wurtzite structure (see Fig. 2.5) that lacks inversion symmetry along the c-axis leading to two possible non-equivalent orientations: Ga-polar and N-polar. All the heterostructures considered in this thesis are wurtzite, grown along the c-axis and Ga-polar.

Another important property of III-N crystals is that along c-axis the barycenters of all positive charges and all negative charges in a unit cell do not coincide, leading to a microscopic dipole formed in each unit cell. Macroscopically, all those small dipoles add up to form a spontaneous polarization that can be seen as planes of fixed surface charge of opposite sign that form at opposite crystal termination surfaces (see Fig. 2.6). In Ga-face III-N material, negative polarization charge is at the top surface and the corresponding positive one is at the bottom of the crystal.

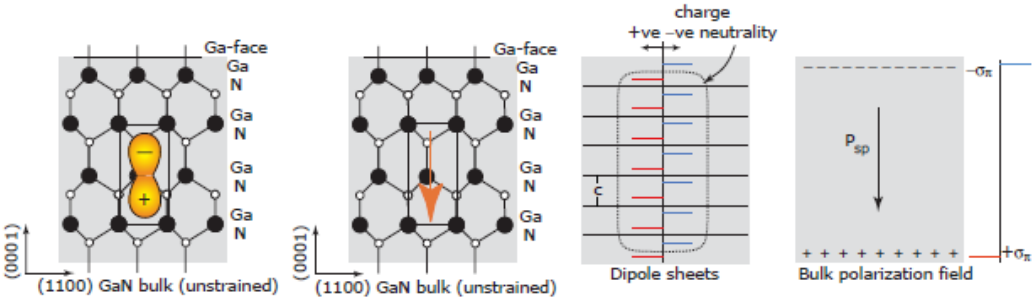

Figure 2.6 – Spontaneous polarization in GaN: from microscopic dipole to macroscopic sheet surface charge [13]

Moreover, if a biaxial in-plane strain is applied additional polarization charge can form along the c-axis. This is a piezo-electric polarization charge that superposes with the spontaneous one. When AlN or AlGaN is grown on GaN, the barrier is under tensile strain (due to lattice constant mismatch). Their piezo component adds up with spontaneous one and enhances the total polarization in the barrier (see Fig. 2.7). For typical Al concentrations (20-30%) in AlGaN barriers, piezo-electric component accounts for about 40% of total polarization charge (see Fig. 2.8). InAlN is usually grown nearly lattice-matched, however, a small mismatch can be introduced to create some strain and enhance the polarization as well.

Thus, an ideal piece of c-axis Ga-face III-N material will have a plane of fixed surface negative polarization charge ($-\sigma_{pol}$) on top and of positive polarization charge (σ_{pol}) on the bottom. $\sigma_{pol} > 0$ denotes the amount of charge per unit surface in cm^{-2}.

2.2.3 Polarization induced 2DEG and 2DHG

What are the consequences of the presence of polarization charges? Let us consider an ideal piece of GaN of thickness d (see Fig. 2.9). It is undoped, no charges are present in the bulk. Two planes of equal, but opposite in sign, surface polarization charges are present at terminating surfaces. This configuration is a usual capacitor with a constant field ($E_\sigma = \frac{\sigma_{pol}}{\epsilon_{GaN}}$) inside and linear potential profile, thus, linear band profile. Potential drop (ΔV) and band-bending (ΔE) through such a piece are related as $\Delta V = -\frac{\Delta E}{q} = E \cdot d$, where $q > 0$ denotes the absolute value of electron charge, and both grow linearly with thickness.

However, GaN is not a dielectric but a semiconductor and it can't accommodate an arbitrary band-bending. When ΔE reaches bandgap (E_g), after certain critical thickness $d_{cr} = \frac{E_g}{qE_\sigma} = \frac{E_g \epsilon_{GaN}}{q\sigma_{pol}}$, Fermi level on each side crosses conduction and valence bands and mobile carriers appear. The field from mobile carriers screens the field created by fixed polarization charges. Total surface charge density at each surface is reduced as mobile carriers have the opposite sign from that of fixed polarization charges at each surface. The neutralizing dipole is formed. This phenomenon is called 'closing of the gap'. One should notice that overall neutrality is conserved: polarization charges always compensate each other by their dipole nature and,

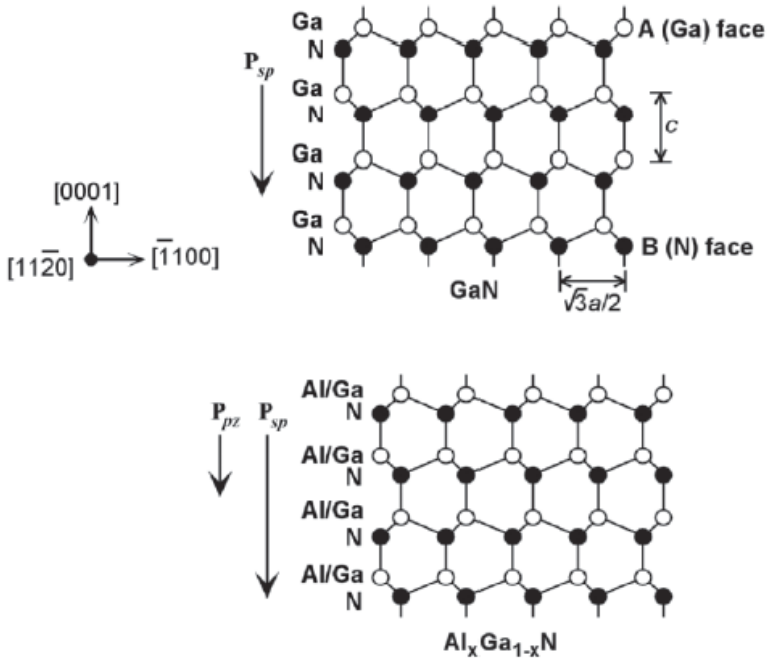

Figure 2.7 – Schematic of crystal structure, spontaneous and piezo polarizations for GaN and AlGaN assumed to be coherently strained to (0001) GaN substrate [13]

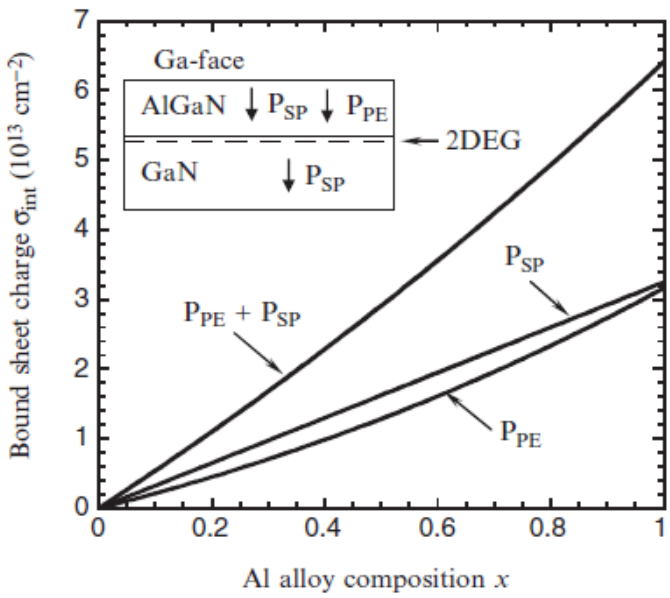

Figure 2.8 – Spontaneous, piezo and total polarization charges as a function of Al composition in AlGaN [13]

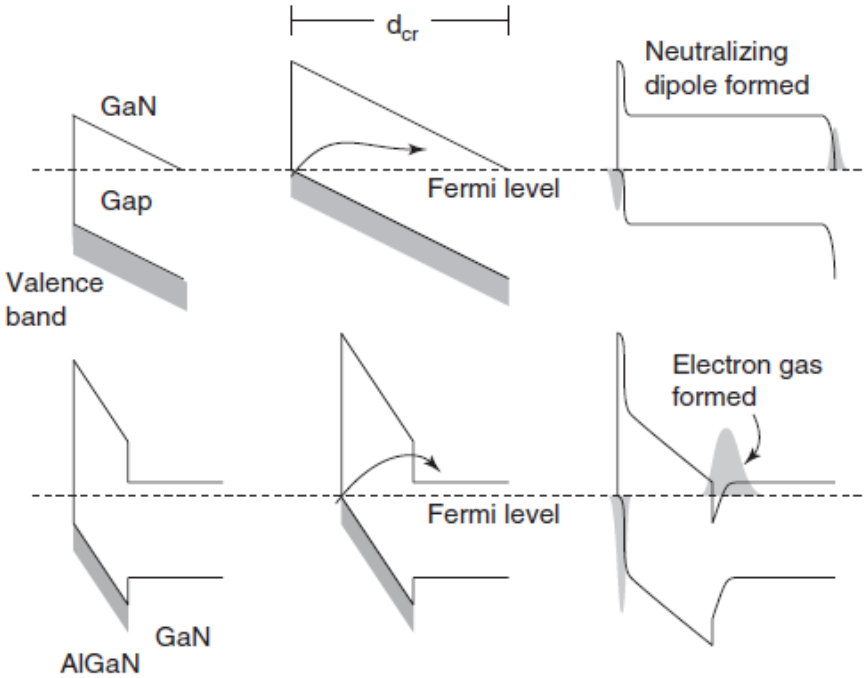

Figure 2.9 – Closing of the gap due to polarization assisted band-bending [13]

thus, induced mobile charges also have equal sheet concentrations, compensating each other.

Formation of the 2DEG in an AlGaN/GaN junction could be qualitatively explained in the same way: once the barrier reaches critical thickness, a neutralizing dipole is formed and we observe a 2DEG at AlGaN/GaN interface and a layer of holes at the top surface of AlGaN. The electrons come into 2DEG from the valence band on the other side of the barrier, leaving exactly the same amount of holes behind. Those holes are also mobile in principle.

It is worth noticing that, contrary to a usual III-V HEMT, such a structure requires no doping to have a 2DEG and to be conductive in the epi plane. In a usual III-V HEMT, such a mechanism is impossible as almost no polarization field is present. Moreover, III-N HEMT can create a high-density 2DEG ($N_s \sim 10^{13}$ cm^{-2}), almost an order of magnitude higher than a typical III-V 2DEG, which keeps the III-N HEMT very conductive even though its room temperature 2DEG mobility is 3-5 times lower than the III-V one.

Yet, we highlight again that even if the 2DEG requires no doping (thus, leaves no positive ionized dopants behind), an equal amount of positive charge has to be formed somewhere to preserve overall charge neutrality. In no case, the role of those positive charges can be taken by fixed polarization charges. Polarization charges always appear paired (if not a pyro-electric material would not be overall neutral) and they never contribute to the total charge balance as they always compensate each other.

In an ideal situation and in some specific heterostructures (considered further), the electrons

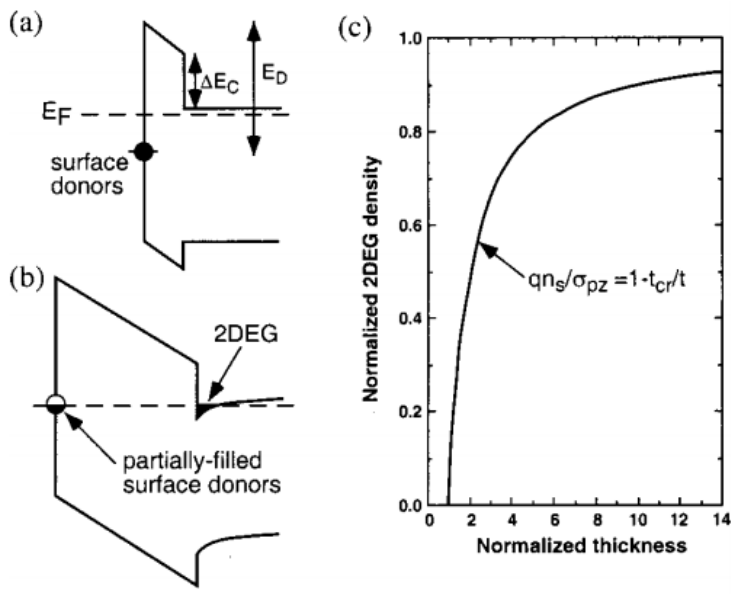

Figure 2.10 – Schematics of the formation of the 2DEG from the surface donor states [34]

come to the 2DEG from the valence band on the other side of the barrier, leaving a two-dimensional hole gas (2DHG) behind. This 2DHG is mobile (even though, $\mu_{2DHG} \sim \frac{1}{20}\mu_{2DEG}$) and has the same sheet carrier concentration (P_s) as the 2DEG: $P_s = N_s$. In that case, similarly to the 2DEG, no p-doping is required to form this 2DHG. Such 2DHGs have been demonstrated experimentally [31]–[33]. p-doped cap, present in experimental structures, only helps to contact the 2DHG and does not participate in the formation of the 2DHG.

However, for the majority of usual single-channel HEMTs with no GaN cap on top of the barrier or just a very thin one, no 2DHG is formed and the origin of the electrons in the 2DEG is different. Ibbetson et al. [34] have experimentally demonstrated that 2DEG appears in AlGaN/GaN heterostructures for thicknesses well below the critical thickness of $d_{cr} = \frac{E_g^{AlGaN}}{qE_\sigma}$. The simplest explanation for this phenomenon is the presence of surface donor states at the top surface of the barrier that lay in the bandgap at the energy $E_D = 1.65$ eV (see Fig. 2.10). A value of 1.65 eV for E_D was suggested in [34]. Then the critical thickness is smaller $d_{cr} = \frac{E_F - E_D}{qE_\sigma} < \frac{E_g^{AlGaN}}{qE_\sigma}$ in accordance with experimental data (Fig. 2.10). In that situation, positive charges left after the formation of the 2DEG are ionized surface donor states. Those charges are fixed, contrary to the mobile 2DHG.

This link between surface state occupation and 2DEG density was exploited in AlGaN/GaN-based sensors for polar molecules. When the surface charge is modified by the adsorbed molecule, 2DEG is modified in the same way. Thus, by measuring 2DEG conductivity, it is possible to sense the surface state [13].

Moreover, the theory of surface donor states at the origin of the 2DEG was later validated by

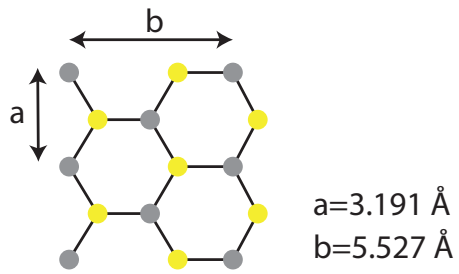

Figure 2.11 – Lattice constats of GaN c-plane [35]

scanning probe microscopy techniques (Kelvin probe microscopy). The energy and surface density values obtained were in accordance with those presented by Ibbetson et al. [13], [34].

The exact nature of those states is a complicated topic. However, one should remember that presence of surface states is intrinsic to the fact of terminating a crystal with a surface. When a crystal is terminated, dangling bonds are left at the surface due to the broken bonds of the atoms. Potentially, there are as many surface states as there are broken bonds (1 per dimer in the case of GaN). A rough estimation for the c-plane GaN gives (see Fig. 2.11) :

$$N_s^{\text{surface states}} = \frac{2 \text{ dimers}}{a \cdot b} = \frac{2}{3.191 \cdot 5.527} \cdot 10^{16} \text{ cm}^{-2} \approx 10^{15} \text{ cm}^{-2}$$

This is clearly enough to create the 2DEG. Intrinsically, just due to finite crystal size, there should be a large amount of surface states present. Of course, on a real surface, much more complicated processes happen: adsorption of other molecules during fabrication, oxidation, presence of dislocations, etc. However, nothing is surprising in the fact that a huge amount of surface states is present at the top of the barrier and their density is large enough to provide all the electrons to the 2DEG.

To summarize, there are two possible sources of electrons in the 2DEG for an undoped III-N HEM heterostructure: valence band on the other side of the barrier or surface states. In the former case, the corresponding positive charges are mobile holes, forming a 2DHG. In the latter case, 2DEG comes from surface states (which is the case for all usual single-channel HEMTs), the positive charges that ensure the charge neutrality are ionized surface donor states that are fixed. Further, in the chapter dedicated to field management using the polarization super junction effect, an intermediate situation will be presented when part of the electrons in the 2DEG comes from surface states and another part from the valence band. If the barrier is doped, the electrons come from the dopants as in a usual HEMT.

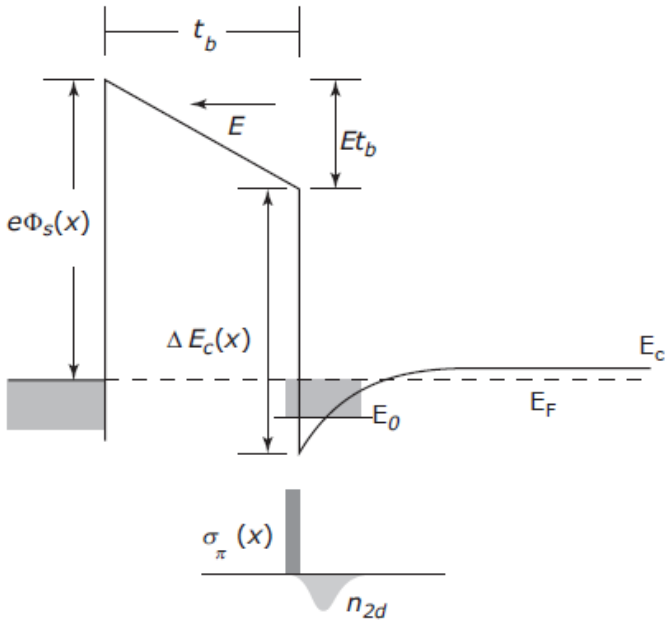

Figure 2.12 – Charge control model for evaluating 2DEG density at the AlGaN/GaN interface [13]

2.2.4 Calculation of N_s

In the most general case, to calculate $n(z)$ and $p(z)$ profiles of the mobile charge distribution in a HEMT one has to self-consistently solve Poisson, Schrödinger and carrier statistics equations.

Typically, a guess for the potential is made first and it is plugged into Schrödinger equation, $n(z)$ and $p(z)$ are calculated using the integral of the carrier statistics weighted by the density of states, plugged back into Poisson, and so on till convergence.

This procedure can be performed using various simulation tools available commercially or provided in open access by some researchers: NextNano, BandEng (UCSB), Greg Sinder's Code (University of Notre Dame), NTU code (Yu Renn Wu), Silvaco Atlas, Sentaurus. However, one has to be cautious as to the interpretation of the results, especially, if a fully coupled solution with Fermi statistics is chosen (often the Schrödinger equation is just solved once after the Poisson one, Maxwell-Boltzmann statistics is set by default). Thus, simplified analytical and semi-analytical tools are necessary to have quick estimations, reduce the optimization time, if one looks for a structure with particular properties, and understand the relative roles of different parameters.

Charge control model offers a nice semi-analytical solution for a single-channel III-N HEMT. From Fig. 2.12 one can easily derive the following relation [13]:

$$e\Phi_s - E \times t_b - \Delta E_c + E_0 + (E_F - E_0) = 0,$$

where $E = e(\sigma_\pi(x) - n_{2d})//\epsilon(x)$. $\sigma_\pi(x)$, $\epsilon(x)$ are total polarization charge (piezo and spontaneous) and absolute electric permittivity of the $Al_xGa_{1-x}N$ barrier. The zero level of the energy is at the bottom of the quantum well at the interface. A single level in the quantum well is supposed to be occupied (E_0). Then ($E_F - E_0$) is obtained using 2D density of states:

$$E_F - E_0 = \frac{\pi\hbar^2}{m^*} n_{2d}$$

And finally E_0 comes from the infinite triangular well approximation:

$$E_0 \approx \left(\frac{9\pi\hbar e^2 n_{2d}}{8\epsilon(x)\sqrt{8m^*}} \right)^{2/3}$$

Because of the 2/3 power in the E_0 this equation is still implicit and has to be solved partially numerically.

However, one can still express n_{2d} analytically and try to "ignore" (neglect E_F, suppose constant E_F) the complicated part which is E_F dependence on n_{2d}:

$$n_{2d} = \sigma_\pi - \frac{\epsilon(x)}{t_b} \frac{e\Phi_s - \Delta E_c + E_F}{e^2}$$

And this is the very expression that is used in practice for many theoretical analyses.

The last expression already contains quite a lot of information. First, n_{2d} is linearly dependent on σ_π, thus, to have a higher 2DEG concentration one would like to have a material with larger polarization discontinuity. From the condition $n_{2d} = 0$ one can estimate the critical barrier thickness needed to have the 2DEG. We see that n_{2d} is always smaller than σ_π and asymptotically approaches it when a larger barrier is used. We see the role of the Schottky barrier and band discontinuity. Thus, although the analytical solution is not fully accurate, it gives all the insights necessary to restrict the search space to a few structures that can be simulated numerically for a more precise estimation of n_{2d} if needed.

We developed our analytical model for carrier concentrations in multi-channel heterostructures with the same idea behind: keep it as simple as possible, still justifying the assumptions to our best, so that one can have a good general vision of the role of each parameter, restrict the space of acceptable structures and then perform numerical simulations for just a few ones to get more precision.

Single-channel structure essentially has only 3-4 parameters to explore: material choice (giving

σ_π, ΔE_C and ϵ), Schottky barrier, barrier, and cap (if used) thicknesses. For a multi-channel, one should also consider channel thickness, eventual doping in the barrier, and the interplay between different channels. Thus, we believe that the analytical model we propose for carrier concentrations in every channel of a multi-channel heterostructure could provide precious insights into the device functioning principles as well as save time and simplify the task of designing a multi-channel stack with desired properties for a given application.

2.3 Model for carrier concentrations in multi-channel HEMTs

This section is based on the paper "Simple analytical model for multi-channel high-electron-mobility III-N heterostructures" by Catherine Erine, Luca Nela, Amirmohammad Miranzadeh, and Elison Matioli , submitted, reference [36] and on the paper "Intrinsic Polarization Super Junctions: application to single and multi-channel structures" by Luca Nela, Catherine Erine, Amirmohammad Miranzadeh and Elison Matioli, submitted [37].

In both papers, Catherine Erine has proposed the idea, developed the theoretical model (in collaboration with Luca Nela), performed numerical simulations to validate the model (in collaboration with Amirmohammad Miranzadeh), designed the experiment, performed measurements, and has written the paper. Sample fabrication was performed by Luca Nela, Amirmohammad Miranzadeh, and Catherine Erine. Jun Ma suggested the optimal heterostructure and performed the growth.

All the subsections with references in the title are entirely taken from the corresponding paper.

2.3.1 Motivation

Multi-channel (superlattice) high-electron mobility (MC-HEM) heterostructures have recently attracted a lot of attention in the domain of power and RF electronics [12], [14], [18]–[26], [38]–[41]. MC-HEM heterostructure is formed by stacking multiple parallel HEM channels on top of each other (Fig. 2.13). As a result, total carrier concentration increases but no mobility degradation is observed as carriers are distributed in multiple normally populated ($N_s \sim 0.5 - 1.5 \cdot 10^{13}$ cm^{-2}) channels. This yields an important reduction of the on-resistance (Fig. 2.13).

MC-HEM diodes and transistors offer a much lower on-resistance without sacrificing the device voltage blocking [12], [14], [18], [19] and switching performances [21]–[25].

However, to fully exploit this technology, one needs to have a good understanding of the carrier distribution in each of the multiple-channels.

Namely, a structure with uneven distribution of carriers among channels would be difficult to control, might present multiple transconductance peaks and it will be difficult to design proper 3D slanted field plates for it to manage the field in the-off state [12], [42]. As we show

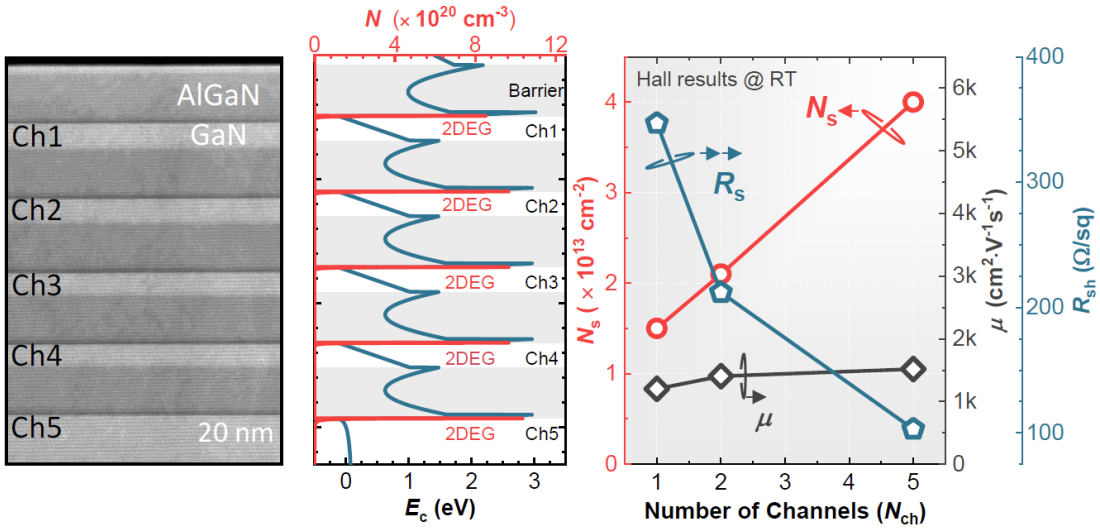

Figure 2.13 – TEM picture (left) and band structure and carrier distribution of a 5-channel HEM heterostructure with 20 nm Si-doped $Al_{0.25}Ga_{0.75}N$ barrier and 10 nm GaN channel (middle). R_{sh}, μ, N_s vs number of channels (right). [14]

from our model, an even distribution of carriers among channels is not at all guaranteed by the simple use of a periodic structure and special precautions should be taken.

Furthermore, novel field management strategies present in super-junction-like devices [26], [38]–[41] require a precise charge balance, restricting even more acceptable carrier concentration distributions.

All those properties (even distribution of carriers, charge balance) can not be insured unless one has a solid understanding of the functioning principles of MC-HEM heterostructures.

Despite a significant number of reports on growth [20], [27], [28] and device fabrication [12], [14], [18]–[26] for particular MC-HEM structures, no information is available as to the general design principles of the channel stack of a multi-channel structure with free carriers (2DEG and 2DHG).

Here we propose a simple physics-based analytical model that sheds light on the carrier distribution in MC-HEMTs and can be used for the ultimate optimization of a MC-HEM channel stack. We perform numerical and experimental validation of the expressions obtained.

2.3.2 General considerations, assumptions and definitions [36]

Consider a heterostructure (Fig. 2.15) consisting of the following layers (from top to bottom) :

- Gate contact, imposing a Schottky barrier of height $q\Phi_b$;

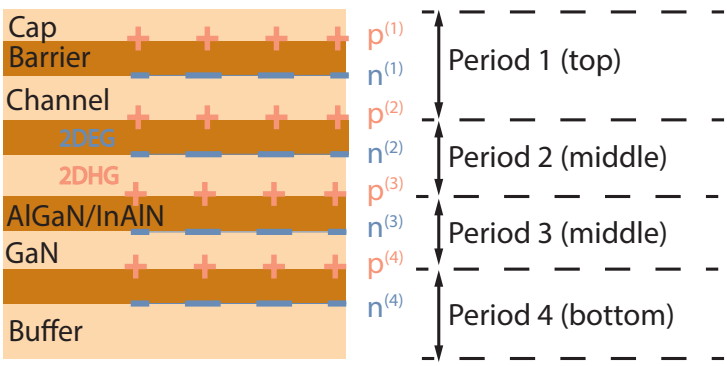

Figure 2.14 – Schematics of a 4-channel high electron mobility heterostructre with 2DHGs and 2DEGs present

- Top period including cap layer, first barrier and first channel;
- $(N-2)$ middle periods (barrier + channel);
- Last period formed by last barrier and buffer.

All the barriers are of thickness d_b, with absolute dielectric permittivity ϵ_b and total polarization charge density σ_b. All the channels are of thickness d_{ch}, with absolute dielectric permittivity ϵ_{ch}, total polarization charge density σ_{ch} and bandgap E_g^{ch}. Channels and barriers can be doped with densities $N_{D,A}^{b,ch}$ correspondingly. Cap (buffer) layers are of thickness d_{cap} (d_{buff}) and are made from the same material as channels.

We consider III-polar crystals as they represent the overwhelming majority of the structures used in practical applications, however, one can use the same approach to derive expressions for N-polar stacks taking care of the charge sign reversal. We define $\Delta\sigma = \sigma_b - \sigma_{ch} > 0$ where σ_b and σ_{ch} include both spontaneous and piezoelectric components if present. We neglect any details about the surface states between the gate and the top of the structure considering that they are already included in the effective Schottky barrier height $q\Phi_b$. Moreover, we consider the buffer to be thick enough so that the electric field vanishes at some point. In case of any doping, all the dopants are considered to be fully ionized.

Free carriers in those structures can be present in the form of 2DEG at the bottom of the barrier ($n^{(i)}$) and possibly 2DHG at the top ($p^{(i)}$). Those free carriers are treated as sheet charges. This assumption does not induce a significant error as typically 2DEG/2DHG extend spatially over few nanometers [43] while channel thickness of the structures considered are well above 10 nm.

We define the quantities $\Delta E_{f,c}^{(i)} = E_c^{(i)} - E_f$ and $\Delta E_{f,v}^{(i)} = E_f^{(i)} - E_v$ which give the penetration of the conduction (valence) band below (above) Fermi level for electrons (holes) at corresponding interfaces (see Fig.2.15). $E_c^{(i)}$ and $E_v^{(i)}$ denote positions of conduction and valence bands at corresponding interfaces. Those quantities are defined positive if 2DEG (2DHG) is present

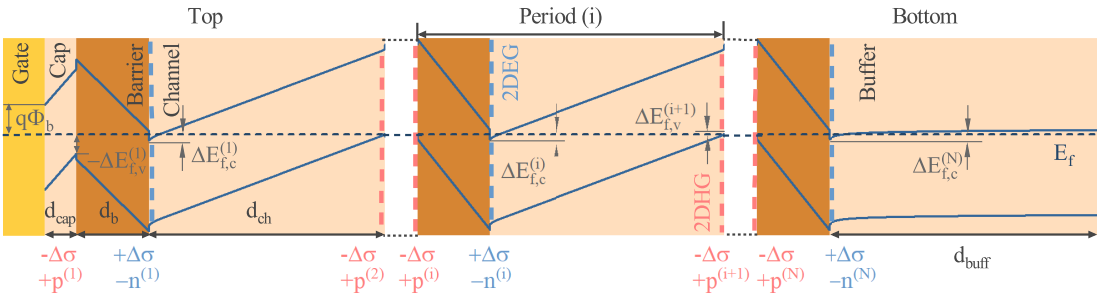

Figure 2.15 – Generic stack of a multi-channel III-N Ga-polar HEMT heterostructure with a simulated band profile of a typical undoped wafer. All the variables used in the model are indicated.

TABLE I. Summary of the main variables employed.

Variable	Definition	Meaning	Units
N		Number of channels	-
d_{cap}		Cap thickness	nm
$d_{b\,(ch)}$		Barrier (channel) thickness	nm
$\varepsilon_{ch\,(b)}$		Absolute dielectric permittivity of the channel (barrier)	F/m
q	$+1.602 \cdot 10^{-19}$	Elementary charge	C
$q\Phi_b$		Schottky barrier height	eV
E_g^{ch}	E_g^{GaN}	Channel bandgap	eV
$\Delta\sigma > 0$	$\sigma_b - \sigma_{ch}$	Polarization discontinuity at barrier/channel interfacee	cm^{-2}
$n^{(i)}$ $(p^{(i)})$		Sheet electron (hole) concentration in the period i	cm^{-2}
$\Delta E_{f,c}^{(i)}$	$E_f - E_c^{(i)}$	Penetration of the Fermi level above the conduction band edge at the 2DEG interface in the period i	eV
$\Delta E_{f,v}^{(i)}$	$E_v^{(i)} - E_f$	Penetration of the Fermi level below the valence band edge at the 2DHG interface in the period i	eV
$\Delta_{c,l}^{v,k}$	$\Delta E_{f,c}^{(l)} + \Delta E_{f,v}^{(k)}$	Sum of $\Delta E_{f,c}^{(l)}$ from period l and $\Delta E_{f,v}^{(k)}$ from period k	eV
Δ	$\Delta_{c,i-1}^{v,i} = \Delta_{c,i}^{v,i} = \Delta_{c,i}^{v,i+1}\ \forall\, i$	Effective parameter used in the analytical expressions	eV

Figure 2.16

at the interface, and thus, conduction (valence) band lies below (above) the Fermi level, and negative elsewise.

To facilitate the understanding of the notation employed, we provide a summary table (Table 2.16) with the names, definitions, and meanings of the most important variables introduced in the text. Schematics with all the notation are given in Fig. 2.14 and Fig. 2.15.

To derive all the formulas one uses displacement vector continuity at each interface and Fermi level continuity through the structure along with Poisson equation in each region (see Supplementary for detailed derivations).

All the simulations were performed using commercially available NextNano software. See supplementary material for simulation details.

2.3.3 Main results [36]

From the simulation results, confirmed by analytical expressions, we deduce that all the carrier concentrations in a multi-channel heterostructure can be divided into three groups of

channels (Fig. 2.15):

- top ($p^{(1)}, n^{(1)}$)
- middle ($p^{(i)}, n^{(i)},\ i = \overline{2, N-1}$)
- bottom ($p^{(N)}, n^{(N)}$)

Middle channels behave as a supperlattice with periodic boundaries. In an undoped structure, they are either populated by both a 2DEG and a 2DHG of equal carrier density or empty. If the barrier is n-doped, the middle channels can either contain only a 2DEG of a density corresponding to the total amount of dopants in the period or contain both a 2DEG and a 2DHG depending on the interplay between doping, channel, and barrier thicknesses. In the latter case, the difference between sheet electron and hole concentrations again equals the total amount of dopants. Carrier concentrations are fully defined by channel and barrier thicknesses and doping, if present.

Bottom channel 2DEG in an undoped case behaves exactly as in an uncapped single-channel HEM heterostructure with a Schottky barrier of E_g^{ch} and its concentration depends only on barrier thickness[13]. The corresponding 2DHG equals 2DHG of the middle channels. For the n-doped barrier, an unexpected dependence on the channel thickness appears if 2DHG is absent in the stack.

Top channel behaves the same as a single-channel structure with a finite buffer thickness (given by the channel thickness). If 2DHG is present, the corresponding 2DEG equals the one from the middle periods. If not, it will depend on the cap thickness and Schottky barrier height. The 2DHG has a similar dependence when present.

When one adds an extra layer to the epi stack, top, bottom, and middle concentrations do not change and the total carrier concentration is just enhanced by one more middle channel. Thus, the dependence of total carrier concentration on the number of channels is linear. This fact was observed experimentally in our previous work on undoped multi-channel heterostructures [20].

It should be highlighted that, in general, neither doped nor undoped structure guarantees an even distribution of carriers in all channels and/or charge balance. To equalize the desired concentrations, layer thicknesses have to be adjusted following the expressions presented below.

In the following sections, we present detailed formulas for each channel and each type of behavior along with their validation by simulation for the two most common barrier materials: $Al_{0.3}GaN$ and near lattice-matched $In_{0.17}AlN$. Those materials present two extremes: low polarization discontinuity (AlGaN) requiring thick structures and high polarization discontinuity (InAlN), leading to thinner stack for a given target carrier concentration. Other material compositions would lay in between these two and can be described by the model as well.

Moreover, the chosen materials are currently present in the overwhelming majority of barriers used in practical device applications. For doped structures, only uniform n doping in the barrier is considered in the main text (formulae for other cases are provided in supplementary information) as this is the main doping profile employed in recent literature[12], [14], [18], [19], [21]–[25]. All the technical details and formula derivations are presented in Supplementary Material.

2.3.4 Model for undoped structures [36]

In case no doping is present, the solution for carrier densities in each channel is given by (see Supplementary Material for derivation):

$$\begin{aligned}
&p^{(i)} = \Delta\sigma - \frac{1}{q^2}\left[\frac{\epsilon_{ch}}{d^*_{ch}}\left(E^{ch}_g + \Delta^{v,i}_{c,i-1}\right) + \frac{\epsilon_b}{d_b}\left(E^{ch}_g + \Delta^{v,i}_{c,i}\right)\right] \\
&n^{(i)} = \Delta\sigma - \frac{1}{q^2}\left[\frac{\epsilon_{ch}}{d_{ch}}\left(E^{ch}_g + \Delta^{v,i+1}_{c,i}\right) + \frac{\epsilon_b}{d_b}\left(E^{ch}_g + \Delta^{v,i}_{c,i}\right)\right] \\
&\qquad\qquad\qquad\qquad\qquad\qquad\qquad\qquad i = \overline{1,N} \\
&\Delta^{v,k}_{c,l} = \Delta E^{(k)}_{f,v} + \Delta E^{(l)}_{f,c} \\
&\Delta E^{(0)}_{f,c} = -q(\Phi_b - V_G) \\
&\Delta E^{(N+1)}_{f,v} = -E^{ch}_g - \Delta E^{(N)}_{f,c} \\
&d^*_{ch} = d_{cap} \;\; if \; i = 1, \;\; d_{ch} \;\; else
\end{aligned} \tag{2.1}$$

In case any of the concentrations $p^{(i)}$ and $n^{(i)}$ predicted by Equation (2.1) is negative, zero should be taken instead.

The only unknown quantities in those equations are $\Delta^{v,k}_{c,l}$ giving the sum of the conduction (valence) band penetrations above (below) the Fermi level at corresponding interfaces. To evaluate them exactly, one must use proper carrier statistics and solve Poisson-Schrodinger equations self-consistently. In general, $\Delta^{v,k}_{c,l}$ depends on the corresponding carrier concentrations, making the system of Equations (2.1) implicit, coupled, and hard to resolve analytically. Fortunately, it turns out that for almost all practically important cases, one can either exclude $\Delta^{v,k}_{c,l}$ from the equations, or neglect it, or replace it with a single constant Δ that is valid for any geometry for a given barrier material. In the following, we demonstrate the validity of such assumption and provide all the information necessary for the correct choice of Δ in a given problem.

Middle channels

Equation (2.1) shows that middle-channel 2DEG (n^{mid}) and 2DHG (p^{mid}) sheet carrier concentrations are all the same except for the term depending on $\Delta^{v,k}_{c,l}$. Simulation results reveal

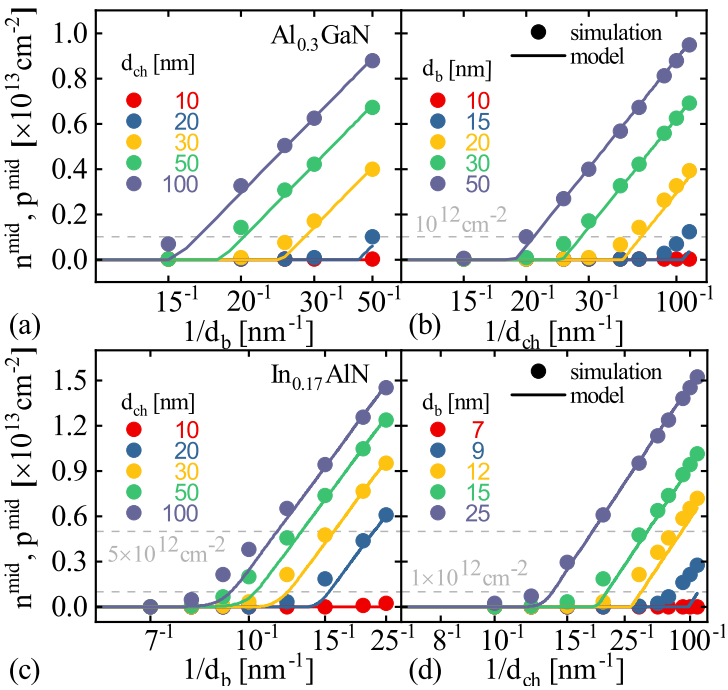

Figure 2.17 – Simulated (dots) and modelled (lines) 2DEG/2DHG sheet carrier concentrations in the middle channels (n^{mid}, p^{mid}) as a function of the inverse barrier (a,c) and the inverse channel (b,d) thicknesses for $Al_{0.3}GaN$ (a,b) and $In_{0.17}AlN$ (c,d). The linear dependence predicted by the model is observed for all practically meaningful n^{mid}, p^{mid} in both materials, validating the choice of a constant Δ. Here Δ was fixed at 266 meV ($Al_{0.3}GaN$) and 432 meV ($In_{0.17}AlN$), minimizing the relative error for all the concentrations above 5×10^{12} cm^{-2} (See Fig. 2.18).

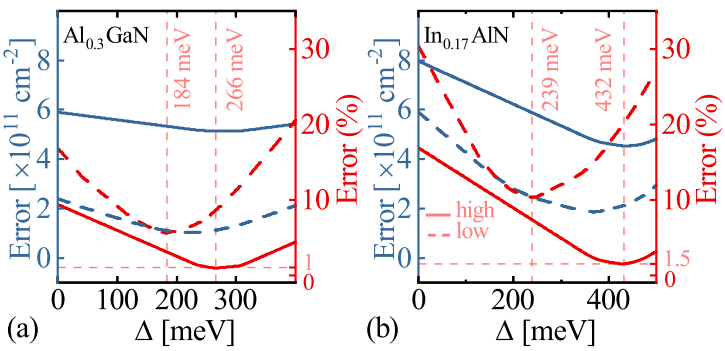

Figure 2.18 – Absolute (blue, left) and relative (red, right) mean errors of the model as a function of Δ for two regions of optimization: $n^{mid} > 5 \times 10^{12}$ cm^{-2} (solid) and $n^{mid} > 1 \times 10^{12}$ cm^{-2} (dashed) with optimal Δ indicated for each case for (a) $Al_{0.3}GaN$ and (b) $In_{0.17}AlN$. If only $n^{mid} > 5 \times 10^{12}$ cm^{-2} are considered, completely neglecting Δ introduces not more than 15% error. The absolute error is below 1×10^{12} cm^{-2} in any situation. For optimal values of Δ the relative error is as low as 2%.

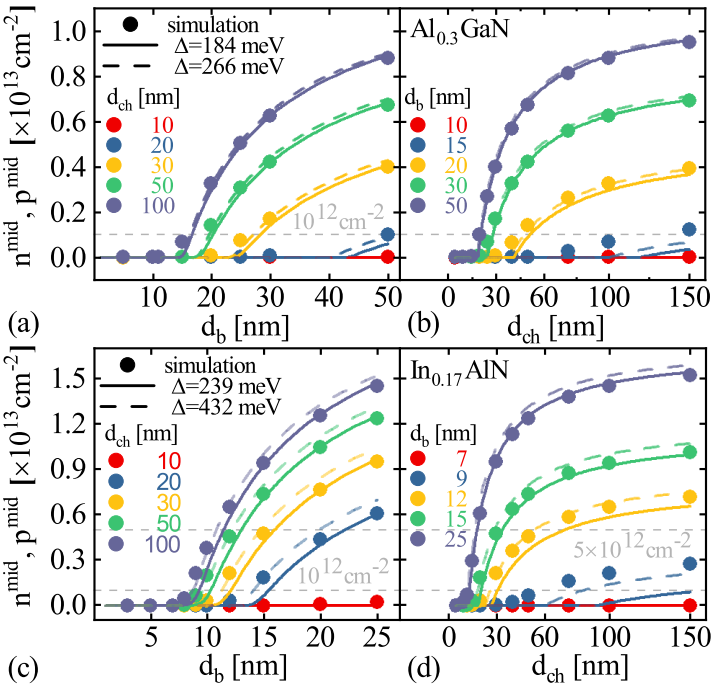

Figure 2.19 – Simulated (dots) and modelled (lines) 2DEG/2DHG sheet carrier concentrations in the middle channels (n^{mid}, p^{mid}) as a function of barrier (a,c) and channel (b,d) thicknesses for $Al_{0.3}GaN$ (a,b) and $In_{0.17}AlN$ (c,d). Modelled values are indicated for both regions of optimization. The low concentration region can be well described by the model at the expense of a small loss of precision for the higher concentration area. $Al_{0.3}GaN$ is way less sensitive to the choice of Δ because of higher barrier and channel thicknesses and lower n^{mid}, p^{mid} (leading to lower Δ).

that, if filled, all the middle channels are the same with $n^{mid} = p^{mid}$, meaning that all the $\Delta_{c,l}^{v,k}$ can be considered equal. However, still remains a question if one can replace $\Delta_{c,l}^{v,k}$ with a single constant Δ or even neglect it. If this was the case, the carrier expressions in the middle channels would follow a very simple formula:

$$n^{mid} = p^{mid} = \Delta\sigma - \frac{E_g^{ch} + \Delta}{q^2}\left[\frac{\epsilon_{ch}}{d_{ch}} + \frac{\epsilon_b}{d_b}\right] \tag{2.2}$$

This expression is true as long as carrier concentrations are linear with inverse barrier and channel thicknesses. Fig. 2.17 shows a perfect linear behavior for both materials for all carrier concentrations above 1×10^{12} cm^{-2} for $Al_{0.3}GaN$ and 5×10^{12} cm^{-2} for $In_{0.17}AlN$, fully justifying the choice of constant material-dependent Δ.

We have restricted the maximum channel thickness to 150 nm for both materials in order to keep a reasonable period thickness. The maximum barrier thickness for $Al_{0.3}GaN$ was set to 50 nm, largely beyond the usual 20-30 nm employed. There is no use in considering very thick barriers as strain from the lattice mismatch of $Al_{0.3}GaN$ causes cracking of the stack for barriers above critical thickness[44]. $In_{0.17}AlN$ barriers are considered up to 25 nm (versus usual 10 nm) as thicker barriers lead to very high carrier concentrations ($> 2 \times 10^{13}$ cm^{-2}) that present little importance for practical applications due to low breakdown and mobility degradation[45]. Moreover, in practical applications carrier concentrations well below 5×10^{12} cm^{-2} are also of limited interest as mobility degradation occurs in low populated channels as well[45].

Unfortunately, the linear dependence was not present for AlN-based barriers due to very high carrier concentrations and very thin (few nm) periods. Thus, our model can not be applied to this material which is however rarely employed in multi-channels due to extreme lattice mismatch, requiring very costly molecular beam epitaxy (MBE) growth on native substrates instead of usual lower-cost metal-organic chemical vapor deposition (MOCVD) on a silicon substrate.

In order to properly choose the numeric value of Δ we estimated the absolute and relative average errors of the model versus simulation as a function of Δ (Fig. 2.18). Two regions of optimization were assessed: all the structures with $n^{mid} > 5 \times 10^{12}$ cm^{-2} (high-density, solid lines) and a wider one - all the structures with $n^{mid} > 1 \times 10^{12}$ cm^{-2} (low-density, dashed lines). The average absolute error is defined as the mean value of the absolute difference between the simulated value and the value predicted by the model. The mean value was taken over all the geometries excluding the ones having n^{mid} outside of corresponding optimization regions. The average relative error is defined as the average under the same restrictions of relative errors. The metrics proposed show how well on average the model describes the chosen carrier concentration region. See supplementary for the mathematical definition.

For any value of Δ and any optimization region, the absolute error never exceeded 1×10^{12} cm^{-2}. Meaning that even if one completely neglects Δ (sets $\Delta = 0$), the average ab-

solute error would always be small compared to practically interesting carrier concentrations ($> 5 \times 10^{12}$ cm^{-2}). This would lead to not more than 10% / 15% error in the high concentration case. However, if better quantitative precision is needed, an optimal Δ of 266 meV (184 meV) for $Al_{0.3}GaN$ and 432 meV (239 meV) for $In_{0.17}AlN$ for high (low) concentration optimization regions can be employed reducing the relative error to only 2%.

As one can see from Fig.2.18, the model proposed is very robust as to the choice of Δ. Absolute error is always below 1×10^{12} cm^{-2} even if Δ is set to zero or to a non-optimal value. However, the relative error can become quite important for low-density structures ($n^{mid} < 5 \times 10^{12}$ cm^{-2}). Thus, one should be particularly careful as to the choice of Δ when dealing with such stacks. The influence of different choices of Δ on the final result is further shown in Fig. 2.19.

Moreover, to support the physical interpretation of Δ being a sum of conduction/valence band penetrations below/above the Fermi level at corresponding interfaces, we have extracted it from the simulations. The values of 270 meV ($Al_{0.3}GaN$) and 391 meV ($In_{0.17}AlN$) were very close to the ones obtained by fitting optimization confirming the correct interpretation of the origin of the parameter Δ.

In order to better see the difference in model predictions versus simulated values, we have plotted carrier concentration versus d_b and d_{ch} for these two different values of Δ (Fig. 2.19). When choosing the optimal Δ for low concentrations one gets a better overall match at the expense of a slight loss of precision for higher concentrations. The Δ optimal for high concentration gives a perfect match for the practically important region at the expense of precision loss for low populated cases. For $Al_{0.3}GaN$ the difference between the two is negligible because of lower carrier densities (and thus lower Δ) and thicker period.

Bottom channel

If carriers are present in the middle channels, the bottom channel can be described by (see Equation (2.1)):

$$n^{bot} = \Delta\sigma - \frac{E_g^{ch} + \Delta}{q^2} \frac{\epsilon_b}{d_b} \tag{2.3}$$

This expression is exactly the same as the one in single-channel uncapped structure if E_g^{ch} is set as Schottky barrier height[13].

From Fig. 2.20 (a), (c) we can see a perfect linear dependence on $1/d_b$ and no dependence on d_{ch} for both materials, as predicted by the model. All the points that do not match the model correspond to the case of empty middle channels which is not interesting for applications and not described by our model. A perfect quantitative match is seen on a direct scale (Fig. 2.20 (b), (d)). The Δ employed is the same one as for middle channels. 2DHG in the bottom period is the same as in the middle ones.

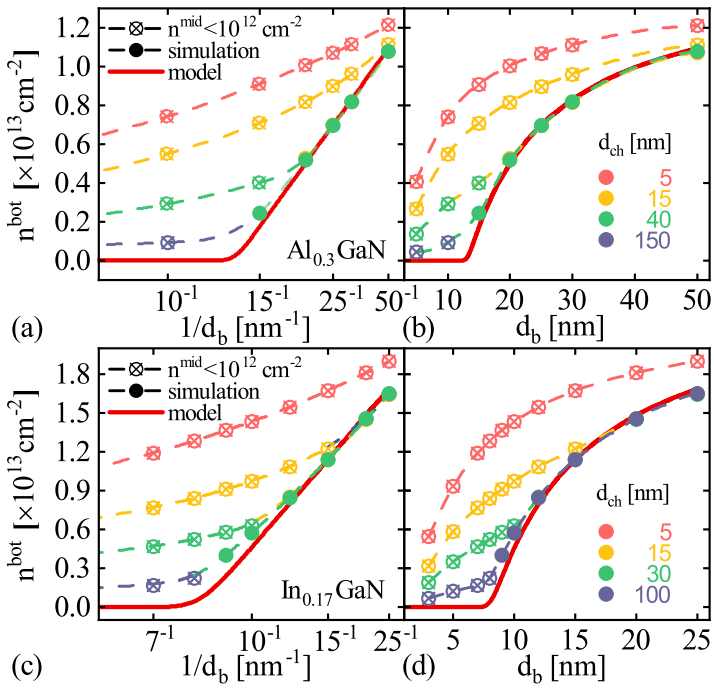

Figure 2.20 – Simulated (dots) and modelled (solid lines) 2DEG sheet carrier concentrations in the bottom channel (n^{bot}) as a function of the inverse barrier (a, c) and barrier (b, d) thicknesses for $Al_{0.3}GaN$ (a, b) and $In_{0.17}AlN$ (c, d). Crossed circles indicate points corresponding to empty ($< 1 \times 10^{12}$ cm^{-2}) middle channels – practically uninteresting case not considered by this model. All the points corresponding to filled middle channels show a perfect linear dependence on $1/d_b$ and no dependence on d_{ch} in agreement with the model. An excellent quantitative match is observed for both materials on a direct scale (b,d).

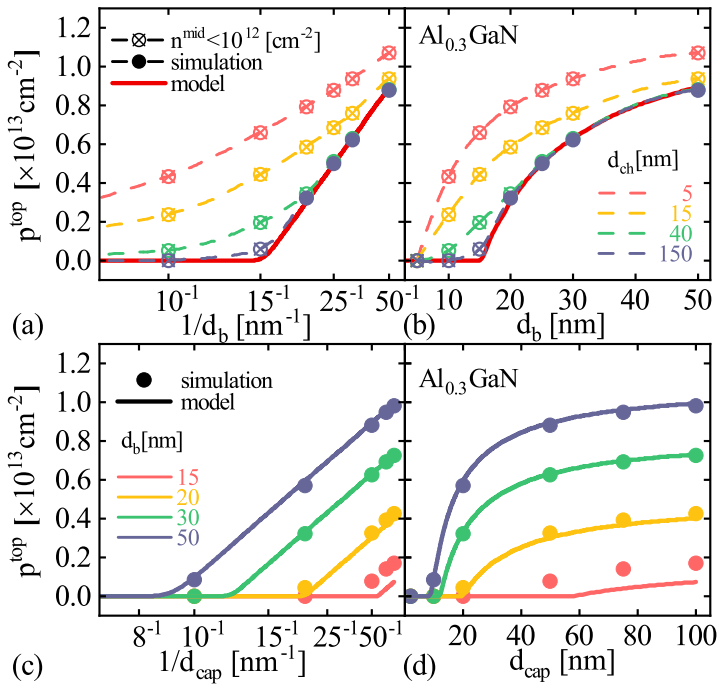

Figure 2.21 – Simulated (dots) and modelled (solid lines) 2DHG sheet carrier concentration in the top channel (p^{top}) as a function of the inverse barrier (a), barrier (b) thicknesses for d_{cap}=50 nm and the inverse cap (c), cap (d) thicknesses, $q\Phi_b$=1.65 eV[34]. Crossed circles indicated points corresponding to empty($< 1 \times 10^{12}$ cm^{-2}) middle channels – practically uninteresting case not considered by this model. All the points corresponding to filled middle channels show a perfect linear dependence on $1/d_b$ and $1/d_{cap}$, there is no dependence on d_{ch} in agreement with the model. No 2DHG is present in the thin cap case. An excellent quantitative match is observed on a direct scale (b,d).

Top channel

When discussing the top channel, one should distinguish two cases: $p^{top} \neq 0$ (occurs for thick enough cap) and $p^{top} = 0$ (thin cap situation).

In the former, top 2DEG is the same as in the middle channels ($n^{top} = n^{mid}$) and p^{top} is given by the following expression (derivation in Supplementary information):

$$p^{top} = \Delta\sigma - \frac{E_g^{ch} + \Delta}{q^2}\left[\frac{\epsilon_{ch}}{d_{cap}} + \frac{\epsilon_b}{d_b}\right] + \frac{(q\Phi_b + \Delta)}{q^2}\frac{\epsilon_{ch}}{d_{cap}} \tag{2.4}$$

where we assumed $\Delta E_{f,c}^{(1)} \approx \Delta_{v,1}^{c,1} = \Delta$. This assumption is justified by the fact that if both 2DEG and 2DHG are present in a period i, $\Delta E_{f,c}^{(i)}$ is of the order of 100-500 meV while $\Delta E_{f,v}^{(i)}$ never exceeds few tens of meV for any material at any geometry.

From Fig. 2.21 one can observe a perfect linear dependence of p^{top} on $1/d_b$ and $1/d_{cap}$

when middle channels are filled (Fig. 2.21 (a), (c)) in accordance with model predictions. An excellent quantitative match is observed on a direct scale (Fig. 2.21 (b), (d)). There is no dependence on channel thickness. For $In_{0.17}AlN$ the behaviour is similar.

In the latter, thin cap case ($p^{top} = 0$), $\Delta E^{(1)}_{f,v}$ can not be simply replaced by Δ or neglected anymore as it becomes negative and could have a large absolute value. In this case one has to express $\Delta E^{(1)}_{f,v}$ from the condition $p^{(1)} = 0$ and plug in the formula for $n^{(1)}$ from Equation (2.1) (see Supplementary Material for details). The resulting formula is the same as the single-channel case with cap, but with a non-vanishing buffer electric field:

$$n^{(1)} = \frac{1}{q}\frac{q\Delta\sigma - \frac{1}{q}\frac{\epsilon_b}{d_b}\left(q(\Phi_b - V_G) + \Delta E^{(1)}_{f,c}\right)}{1 + \frac{\epsilon_b}{\epsilon_{cap}}\frac{d_{cap}}{d_b}} - \\ - \frac{1}{q^2}\frac{\epsilon_{ch}}{d_{ch}}\left(E^{ch}_g + \Delta^{c,1}_{v,2}\right) \tag{2.5}$$

The first term is exactly the capped single-channel solution [46] and the second accounts for the finite field in the channel (in the single-channel case it is absent due to the vanishing field in the buffer). $\Delta E^{(1)}_{f,c} \approx \Delta^{c,1}_{v,2} = \Delta$ as $\Delta E^{(2)}_{f,v}$ is small due to 2DHG being present in the second period (if not middle channels are empty). We do not provide validation for this case as this formula is already present in literature [46]–[48].

One can easily express d^*_{cap} that delimits thin and thick cap cases by setting $p^{top} = 0$ in Equation (2.4) and get:

$$d^*_{cap} = \epsilon_{ch}\frac{\frac{E^{ch}_g - q\Phi_b}{q^2}}{\Delta\sigma - \frac{E^{ch}_g + \Delta}{q^2}\frac{\epsilon_b}{d_b}} \tag{2.6}$$

2.3.5 AlN interlayer [36]

Most of the modern III-N heterostructures employ a thin (< 1 nm) AlN interlayer at the interface between the barrier and the channel to enhance mobility and carrier concentration [49]. One can show (see supplementary information) that the main effect of the interlayer on the carrier concentrations is to increase the polarization discontinuity according to the following relation:

$$\Delta\sigma^{int} = \Delta\sigma^{no\,int} + \frac{\sigma_{int} - \sigma_b}{1 + \frac{\epsilon_{int}}{\epsilon_b}\frac{d_b}{d_{int}}} \tag{2.7}$$

where $\sigma^{int} > 0$ accounts for the total polarization charge density of the interlayer. Thus, the

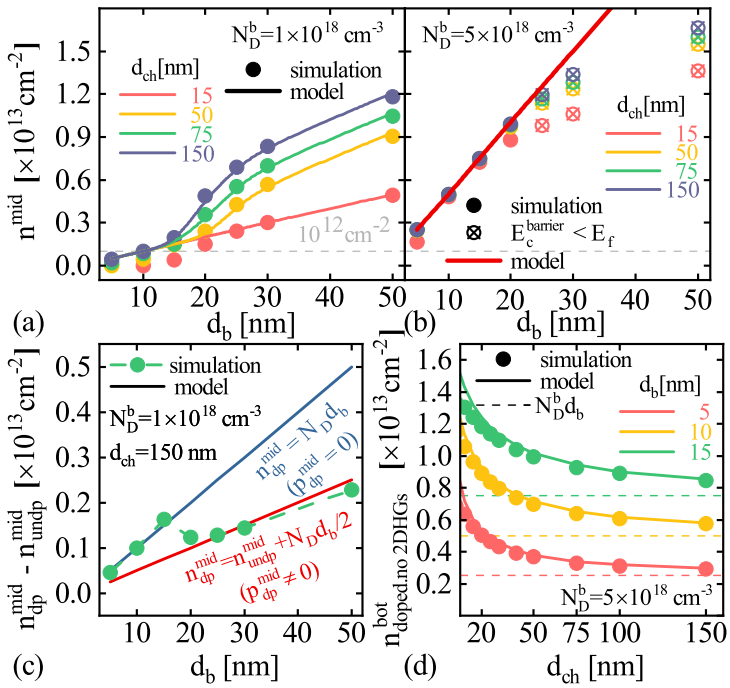

Figure 2.22 – Simulated (dots) and modelled (solid lines) 2DEG sheet carrier concentration in the middle channel (n^{mid}) as a function of barrier thickness for light doping and the stack is thick enough, $N_D^b = 1 \times 10^{18}$ cm^{-2} (a) and heavy doping, $N_D^b = 5 \times 10^{18}$ cm^{-2} (b). An excellent match between simulation and model is observed. Crossed circles indicate points corresponding to the case of the parasitic parallel channel in the barrier, not described by this model. (c) $n_{dp}^{mid} - n_{undp}^{mid}$ vs barrier thickness graph showing two regimes: no 2DHGs in the doped structure (blue) and 2DHGs present due to light doping (red). (d) Simulated (dots) and modelled (solid lines) 2DEG sheet carrier concentration in the bottom channel ($n_{doped,\,no2DHGs}^{bot}$) of a doped structure with no 2DHGs present as a function of channel thickness. Dashed lines indicate $n_{doped}^{mid} = N_D^b d_b$. An excellent match between model and simulation is observed.

interlayer can be integrated into the proposed model by simply adjusting $\Delta\sigma$.

2.3.6 Model for doped barrier structures [36]

In order to populate middle channels in an undoped structure with electrons a relatively large period thickness is needed[20], [26]. Another way to achieve high carrier concentrations is to introduce n doping in the barrier[12], [18], [19], [22]–[25]. One can easily extend the undoped model to that case.

In case the 2DHGs are still present in each period ($N_D^b d_b/2 < p_{undoped}^{(i)}$ $\forall\, i$, thick cap), the

expressions for carrier concentrations are very simple:

$$\begin{aligned} n^{(i)}_{doped,2DHGs} &= n^{(i)}_{undoped} + \frac{N^b_D d_b}{2} \quad \forall\, i \\ p^{(i)}_{doped,2DHGs} &= p^{(i)}_{undoped} - \frac{N^b_D d_b}{2} \quad \forall\, i \end{aligned} \tag{2.8}$$

So if the doping is light, half of it goes to diminish hole concentration and only half to enhance electrons. A very good match is observed between the model and the simulation (Fig. 2.22 (a)), using the same Δ as in the undoped case.

The thin cap case, when all the 2DHGs except the first one are present, can be treated similarly to the undoped thin cap (see supplementary information for the expression and its derivation).

In case of heavy enough doping and/or thin stack ($N^b_D d_b/2 < p^{(i)}_{undoped}\ \forall\, i$) $p^{(i)}$ vanishes and only 2DEGs are present in the structure.

In this situation, middle channels behave as one would expect with n^{mid} equivalent to the total amount of dopants in the period (Fig. 2.22 (b)) :

$$n^{mid}_{doped,no\,2DHGs} = N^b_D d_b \tag{2.9}$$

No dependence on channel thickness is observed for middle channels, allowing to shrink the period by shrinking the channel.

However, one should pay attention to the fact that in case of too heavy doping (or too large doped barrier) the quadratic band profile in the barrier can cross the Fermi level. Then part of the dopants does not fall in the quantum well at the interface but stays in the conduction band of the barrier. A parallel low-mobile channel is formed with as much as 15% of the mobile carriers located in the barrier even for relatively moderate doping of 5×10^{18}cm^{-3} and 25 nm barrier. That regime comes into play very early and does not require any unreasonable dopings or geometries. The effect of AlN interlayer is beneficial but does not fully solve the issue. The proposed model does not describe this highly undesirable situation as mobile carriers are not limited to the 2DEG anymore and cannot be treated as sheet charges at the interface. All the points in Fig. 2.22 (b) that do not match the model originate from that situation.

All the data in Fig. 2.22 is provided for $Al_{0.3}GaN$ with Δ taken from the undoped structure.

By plotting the difference between doped (n^{mid}_{dp}) and undoped (n^{mid}_{undp}) sheet electron concentrations in the middle channel as a function of d_b at a relatively low N^b_D of 1×10^{18} cm^{-3} (Fig. 2.22 (c)), one can clearly see the two regimes for middle channels. First, the barrier is thin, corresponding to an empty undoped stack ($n^{mid}_{undp} = 0$), and n^{mid}_{dp} just equals the total amount of dopants in the barrier, following the blue curve (Equation (2.9)). Once the barrier is thick enough to allow $n^{mid}_{undp} > 0$, the 2DHG appears and n^{mid}_{dp} switches to the red curve, described

by Equation (2.7). If the doping was heavier this switch would occur at higher d_b or even never happen.

Until now, a doped structure without 2DHGs looks like the simplest one to design: one only needs to carefully check for the parallel channel in the barrier, and the desired 2DEG would be just the total amount of dopants in the period. Unfortunately, this is not true for the bottom and top periods. An unexpected dependence on channel thickness appears in the expression of $n^{bot}_{doped,no\,2DHG}$ (derivation in supplementary information):

$$n^{bot}_{doped,\,no\,2DHG} = N^b_D d_b + \frac{\Delta\sigma - \frac{N^b_d d_b}{2}}{1 + \frac{\epsilon_b}{\epsilon_{ch}} \frac{d_{ch}}{d_b}} \tag{2.10}$$

This dependence is not in favor of thin structures as the mismatch between middle and bottom channels increases when d_{ch} is reduced. Moreover, for typical dopings and barriers, the last channel would be more populated than the middle ones, making the gate control more difficult and limiting the breakdown voltage. Fig. 2.22 (d) shows the modelled and simulated $n^{bot}_{doped,no\,2DHG}$ as a function of d_{ch} for different d_b. The mismatch created at low d_{ch} is significant: $3-5\times10^{12}\ cm^{-2}$ for commonly employed d_{ch} of 20 nm. The only way to balance the channels is to use $d_b = 2 * \Delta\sigma / N^b_D$. But then for $Al_{0.3}GaN$ doped with $N^b_D = 5\times10^{18}\text{cm}^{-3}$ one would need a 60 nm barrier - impossible to use as the parallel channel in the barrier will appear at way lower d_b.

The top channel dependence is more sophisticated (see supplementary information), but in the limit of the very thick cap ($d_{cap} \to \infty$) one gets an expression very similar to Equation (2.11):

$$n^{top,\,d_{cap}\to\infty}_{doped,\,no\,2DHG} = N^b_D d_b - \frac{\Delta\sigma - \frac{N^b_d d_b}{2}}{1 + \frac{\epsilon_b}{\epsilon_{ch}} \frac{d_{ch}}{d_b}} \tag{2.11}$$

The only difference is the sign of mismatch, meaning that usually, the top channel will be less populated. This mismatch is less problematic as $n^{top}_{doped} < n^{mid}_{doped}$ does not limit the breakdown.

2.4 Experimental validation of the model [37]

Direct measurement of carrier concentrations in each channel is quite challenging. However, quite a lot of information is available from the dependence of total carrier concentration on the number of channels for a given period and cap geometry in a given material. Let us shortly

	n_s	p_s
Middle	$\Delta\sigma - \frac{E_g^{ch}+\Delta}{q^2}\left(\frac{\varepsilon_{ch}}{d_{ch}}+\frac{\varepsilon_b}{d_b}\right)+\frac{N_D d_b}{2}$	$\Delta\sigma - \frac{E_g^{ch}+\Delta}{q^2}\left(\frac{\varepsilon_{ch}}{d_{ch}}+\frac{\varepsilon_b}{d_b}\right)-\frac{N_D d_b}{2}$
	$N_D d_b$	0
Bottom	$\Delta\sigma - \frac{E_g^{ch}+\Delta}{q^2}\frac{\varepsilon_b}{d_b}+\frac{N_D d_b}{2}$	$\Delta\sigma - \frac{E_g^{ch}+\Delta}{q^2}\left(\frac{\varepsilon_{ch}}{d_{ch}}+\frac{\varepsilon_b}{d_b}\right)-\frac{N_D d_b}{2}$
	$N_D d_b + \frac{\Delta\sigma - \frac{N_D d_b}{2}^{(*)}}{1+\frac{\varepsilon_b}{\varepsilon_{ch}}\frac{d_{ch}}{d_b}}$	0
Top	$\Delta\sigma - \frac{E_g^{ch}+\Delta}{q^2}\left(\frac{\varepsilon_{ch}}{d_{ch}}+\frac{\varepsilon_b}{d_b}\right)+\frac{N_D d_b}{2}$	$\Delta\sigma - \frac{E_g^{ch}+\Delta}{q^2}\left(\frac{\varepsilon_{ch}}{d_{cap}}+\frac{\varepsilon_b}{d_b}\right)+\frac{q\Phi_b+\Delta}{q^2}\frac{\varepsilon_b}{d_{cap}}-\frac{N_D d_b}{2}$
	$N_D d_b + \frac{\Delta\sigma - \frac{N_D d_b}{2} - \frac{q\Phi_b+\Delta}{q^2}\frac{\varepsilon_{ch}}{d_{ch}}}{1+\frac{\varepsilon_b}{\varepsilon_{ch}}\frac{d_{cap}}{d_b}} - \frac{E_g^{ch}+\Delta}{q^2}\frac{\varepsilon_{ch}}{d_{ch}}$	0 $(p_s^{middle} \neq 0)$
	$N_D d_b + \frac{\Delta\sigma - \frac{N_D d_b}{2} - \frac{q\Phi_b+\Delta}{q^2}\frac{\varepsilon_{ch}}{d_{ch}}}{1+\frac{\varepsilon_b}{\varepsilon_{ch}}\frac{d_{cap}}{d_b}} - \frac{\Delta\sigma - \frac{N_D d_b}{2}^{(*)}}{1+\frac{\varepsilon_b}{\varepsilon_{ch}}\frac{d_{ch}}{d_b}}$	0 $(p_s^{middle} = 0)$
$^{(*)}$ Not valid for undoped structures (N_D=0)		

Figure 2.23 – Summary of the expression for carrier concentrations in undoped and n-doped in the barrier multi-channel heterostructures

summarize the expressions for carrier concentrations (see Table 2.23).

What dependence of n_s on the number of channels should we expect? Middle channels are always the same with 2DEG carrier concentration n_s^{mid}, top channel (n_s^{top}) and bottom channels (n_s^{bot}) are different from the middle ones in general case. In a series of heterostructures with the same epi geometry but different number of channels (N), all the middle channels would be the same for any heterostructure $N \geq 3$. Top and bottom channels will also be the same starting from the 2 channel case. Moreover, in the single channel case $n_s = n_s^{top} + n_s^{bot}$. Thus, the dependence of total sheet carrier concentration n_s^{Σ} on number of channels can be expressed as:

$$n_s^{\Sigma} = n_s^{top} + n_s^{bot} + (N-2)\cdot n_s^{mid},$$

where $N \geq 1$ is the number of channels.

Thus, if we grow a series of wafers with a different number of channels we should see a linear dependence of the total sheet carrier on the number of channels with the slope corresponding to the middle channel n_s^{mid}.

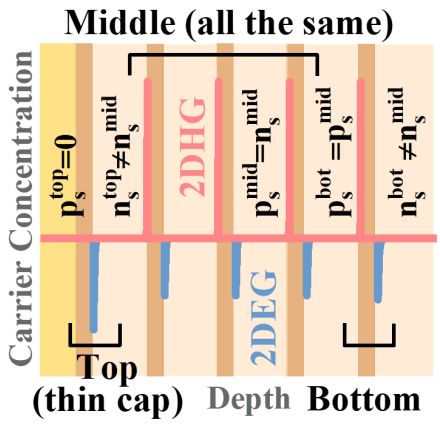

Figure 2.24 – Schematics of an undoped multi-channel structure: middle channels are always the same for any number of channels bigger than 3, top and bottom also stay the same starting from the two-channel case. For the doped structure, the situation is similar except that usually it is designed so that 2DHGs are absent and middle channel carrier concentration is equal to the total doping in the barrier.

To check this conclusion and validate the model, we have grown two series of wafers.

Undoped series with 1,3, 5 and 10 periods of 2 nm i-GaN cap / [23 nm i-$Al_{0.308}Ga_{0.692}N$/ 1 nm i-AlN/ 75 nm i-GaN] x N / 3 μm i-GaN / 300 nm AlN on sapphire substrate (see Fig. 2.25).

Doped series with 5, 7, and 10 periods of 4 nm i-GaN cap / [1 nm i-$Al_{0.25}Ga_{0.75}N$/ 8 nm $Al_{0.25}Ga_{0.75}N$ $N_D = 5 \cdot 10^{18}$ cm^{-3}/ 1 nm i-$Al_{0.25}Ga_{0.75}N$/ 1 nm i-AlN/ 10 nm i-GaN] x N / 150 nm i-GaN channel / 4.3 μm GaN buffer on Si substrate (see Fig. 2.26). Moreover, 1- and 2-channel structures were produced by etching out top channels of the 5-channel wafer.

After growth, wafers were cut into chips and processed to pattern Hall squares. For the doped series, a blank etch of the 5-channel chip to obtain 1 and 2 channel ones was performed. The resulting etch depth was controlled by AFM on special test patterns present next to the corresponding Hall squares to confirm the number of channels left and the etching uniformity. Then for all chips, mesa was defined by optical lithography and etched. All the etchings were performed in Cl_2-based inductively coupled plasma (ICP) to isolate Hall squares from each other. Then ohmic contact was formed using one optical lithography followed by metal deposition, lift-off, and annealing. A metal stack consisting of Ti (200 Å)/ Al (1200 Å)/ Ti (400 Å) / Ni (600 Å) / Au (500 Å) was deposited by electron-beam evaporation and annealed at 860 °C. Hall measurements were performed in 4-lead Hall square geometry following the procedure from Lake Shore 7500/9500 Series Hall System User's Manual, using Keithley 6221 current source, 2182A nano-voltmeter, 2612B source-measurement unit as picoammeter, 3765 Hall Effect card as a switch and permanent 0.345 T magnet (field measured by gaussmeter on the chuck). Current, field reversal and homogeneity checks were performed to minimize errors. In each case, measurements were performed over at least 4 Hall squares in different parts of the chip except the doped 10 channel wafer where cracking occurred and only 2 squares were

2 nm GaN cap	X 1,3,5,10
23 nm AlGaN barrer (x=30.8%)	
1 nm AlN	
75 nm GaN	
3-um GaN buffer	
300 nm AlN	
Sapphire	

Figure 2.25 – Schematics of the undoped heterostructure used for the experimental model verification

4 nm GaN cap	X 5,7,10
1 nm i-$Al_{0.25}GaN$	
8 nm $Al_{0.25}GaN$ N_D=5e18 cm^{-3}	
1 nm i-$Al_{0.25}GaN$	
0.7 nm AlN	
10 nm GaN	
150 nm i-GaN channel	
4.3 um GaN buffer	
Si	

Figure 2.26 – Schematics of the doped heterostructure used for the experimental model verification

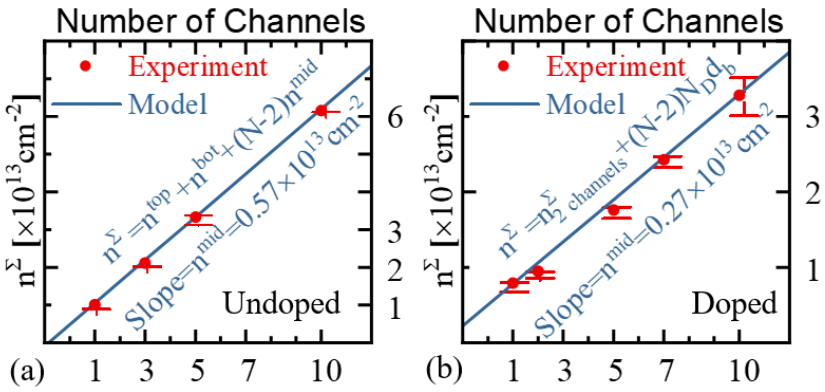

Figure 2.27 – Experimental data (red circles) and linear fit (blue line) of n_s^{Σ} vs number of channels dependence for (a) the undoped series of 1,3,5 and 10 channel wafers; (b) for the barrier doped series of 1, 2, 7, and 10 channel wafers. The trend is linear as predicted by the model.

appropriate for measurements.

Experimental results obtained for both doped and undoped structures are in perfect accordance with the model (see Fig.2.27 (a), Fig.2.27 (b)).

The undoped series of 1,3,5, and 10 channel heterostructures (see Fig 2.27 (a)) presented a linear dependence of carrier concentration on number of channels with a slope of $0.57 \cdot 10^{13}$ cm^{-2} giving the n_s^{mid}. For the nominal structure parameters the model predicts $n_s^{mid} = 0.63 \cdot 10^{13}$ cm^{-2}, yielding a perfect agreement with experiment within the measurement error and possible deviations from nominal growth parameters.

The doped doped series of 1, 2, 5, 7, and 10 channels also presented linear behavior with a slope of $0.27 \cdot 10^{13}$ cm^{-2} giving the n_s^{mid}. However, model and simulation predict $n_s^{mid} = 0.4 \cdot 10^{13}$ cm^{-2} - total sheet carrier concentration of dopants in the doped 8 nm of the barrier. The discrepancy can be explained by only partial dopant activation and incorporation during growth. 68 % of incorporated Si dopants giving electrons to the conduction band in $Al_{0.25}Ga_{0.75}N$ is an acceptable value [50]. However, precise reasons behind this should be further explored by first doing SIMS (secondary ion mass spectroscopy) measurement to exactly determine the amount of incorporated Si atoms and then investigating some calibration samples to precisely know the activation ratio.

Experimental results are in full accordance with the model and simulation, supporting the validity of the proposed model. The quantitative discrepancy between model (simulation) and experiment for doped structures can probably be explained by only partial dopant activation of Si dopants - a typical phenomenon for AlGaN [50].

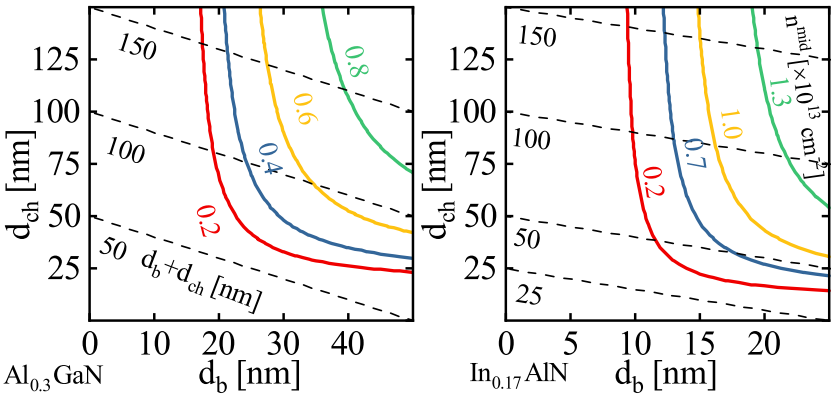

Figure 2.28 – Level lines of carrier concentration as a function of barrier and channel thicknesses for AlGaN (left) and InAlN (right).

2.5 Consequences of the model for the channel stack design [37]

2.5.1 Minimum period required to get a given n_s^{mid}

Some fundamental restrictions on carrier concentrations achievable within a given material with a reasonable period thickness can be deduced from the model proposed. By plotting the contour lines corresponding to different middle channel concentrations on the d_{ch} vs d_b plot (see Fig. 2.28) together with straight lines giving all the structures with a given period one can see that in an undoped structure for any given material there is a minimal period thickness (p^*) required to achieve desired n_s^{mid}.

It is possible to derive p^* by solving the minimization problem: minimize $p^* = d_b + d_{ch}$ under the restriction of n_s^{mid} given by the expression from the Table 2.23. For an undoped structure p^* required to obtain a given n_s in middle channels is described by the following expression:

$$p^* = \frac{\epsilon_b + \epsilon_{ch} + 2\sqrt{\epsilon_b \epsilon_{ch}}}{\Delta\sigma - n_s} \frac{E_g^{ch} + \Delta}{q}$$

By plotting this p^* vs n_s for different materials (see Fig. 2.29) one can quantitatively see the advantage of using materials with higher polarization discontinuity and of employing an AlN interlayer (that mainly enhances $\Delta\sigma$). To achieve a typical n_s of $0.8 \cdot 10^{13}$ cm^{-2} in the middle channel one would need at least 117 nm on $Al_{0.3}GaN/GaN$ (reduced to 83 nm if 1 nm AlN interlayer employed) and only 49 nm of nearly-lattice-matched $In_{0.17}AlN$ (reduced to 42 nm with 1 nm AlN interlayer).

Similarly, if one decides to use a different material or different composition, it is possible to have an idea of the period required by plotting p^* vs $\Delta\sigma$ for a given n_s (see Fig. 2.29). Of course, this is a rough estimation as bandgap and permittivity would also change if a different material is employed. However, those changes are quite minor for the most common materials

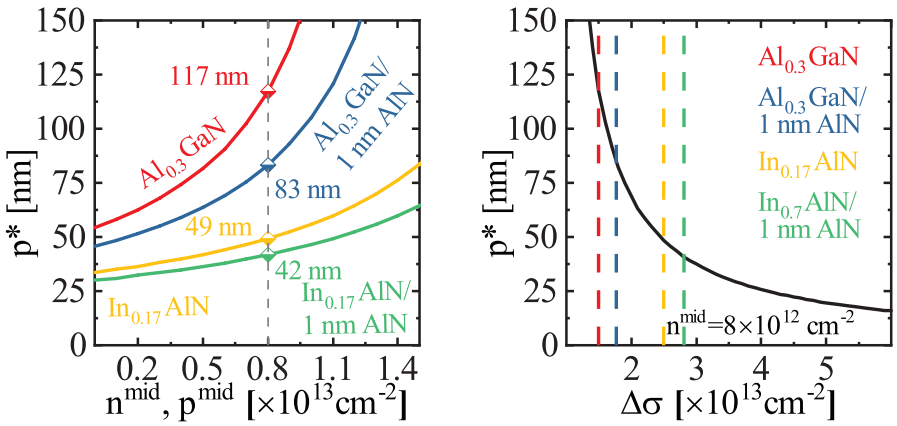

Figure 2.29 – Left: minimum period thickness required to achieve a given n_s^{mid} in different materials; Right: minimum period thickness required to achieve $n_s^{mid} = 0.8 \cdot 10^{13}$ cm^{-2} as a function of polarization discontinuity. Most common stacks are indicated by vertical lines.

(AlGaN, InAlN). Vertical lines indicate the most common epi configurations for the reference.

However, when considering the doped structure, it is possible to show that within the model boundaries, no minimal channel thickness exists and to obtain a given n_s^{mid} it is sufficient to use N_D and d_b such that $N_D d_b = n_s^{mid}$. Yet, one has to be extremely careful when working with doped structures. To keep a reasonable barrier thickness ($d_b < 30$ nm) and achieve some useful carrier density $n_s \geq 0.6 \cdot 10^{13}$ cm^{-2} one would need an N_D of at least $2 \cdot 10^{18}$ cm^{-3}. However, very quickly the doping in the barrier may become too heavy dipping the Fermi level in the barrier under the conduction band edge and transferring a non-negligible part of the 2DEG inside the barrier (see Fig. 2.30). As shown in the Fig. 2.30 for a relatively low doping of $5 \cdot 10^{18}$ cm^{-3} and typical $d_b = 20$ nm and $d_{ch} = 30$ nm as much as 15% of the total 2DEG is located in the barrier. This is highly undesirable. Being next to the dopants in the barrier, this part of 2DEG loses its high mobility. If an interlayer is used the situation is a little better, but a parallel channel in the barrier can still appear quite easily.

The situation of too low doping is not very probably for thin channels, thus, this is not the most common precaution to be taken.

Moreover, the parasitic conductance in the barrier is not the only potential problem of trying to shrink the channel as much as possible to minimize the period in a doped structure. As shown in section 2.4.5 when a thin channel is used in a doped stack the bottom-most channel starts to be overpopulated, making the control more difficult, carrier distribution uneven, potentially leading to punch-through and breakdown problems.

2.5.2 Even distribution of carriers among channels

As discussed above, in both doped and undoped structures even distribution of carriers is not guaranteed by using a periodic structure. Middle channels would always be the same but not

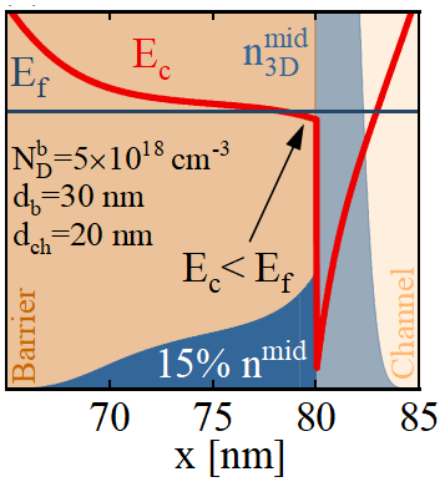

Figure 2.30 – Band structure and electron concentration profile in the middle channel of a n-doped ($N_D = 5 \cdot 10^{18}$ cm^{-3}) $Al_{0.3}GaN/GaN$ heterostructure with $d_b = 20$ nm and $d_{ch} = 30$ nm. Due to heavy doping and large barrier the 2DEG is partially delocalized in the barrier.

the top and bottom ones.

In an undoped structure, the easiest way to obtain $n_s^{top} = n_s^{mid}$ is to use a cap thick enough so that the top 2DHG also appears, automatically matching the first 2DEG to the middle ones. In the absence of a thick cap, top 2DEG density would depend on Schottky barrier height or surface state for free surfaces - which is highly undesirable as difficult to control.

As for the bottom channel, it will always be more populated unless some back barrier is designed. However, the mismatch between the last channel and others satisfies:

$$n_s^{bot} - n_s^{mid} = \frac{E_g^{ch} + \Delta}{q^2} \frac{\epsilon_{ch}}{d_{ch}}$$

For larger channels this mismatch becomes smaller. For example, if d_{ch} of 100 nm is employed in $Al_{0.3}GaN$ the mismatch will only be $0.2 \cdot 10^{13}$ cm^{-2}.

Another way to deal with this mismatch is to adjust the last barrier thickness. This approach was followed in the heterostructures present in the literature [12], [14]. In that situation the thickness of the last barrier (d_b^*) should be:

$$d_b^* = \frac{\epsilon_b}{\frac{\epsilon_b}{d_b} + \frac{\epsilon_{ch}}{d_{ch}}}$$

Which, for example, gives around 17 nm for the main $Al_{0.3}GaN$ barrier of 23 nm and 75 nm channel.

For the doped structure, the only realistic way to try to diminish the mismatch is to use both a thicker cap and a thicker channel. One should notice that it is mathematically possible to choose doping such that the last channel equals the middle ones. $N_D = \frac{\Delta\sigma}{d_b}$ would do the job. However, even for the low-polarization $Al_{0.3}GaN$ and a typical 20 nm barrier it would require doping of $N_D = 1.5 \cdot 10^{19}$ cm^{-3} - very difficult to achieve in practice in AlGaN.

2.5.3 Balancing electrons and holes

Another important question is the balance between the total amount of holes and the total amount of electrons in the heterostructure. Charge balanced multi-channel HEM heterostructures recently attracted quite a lot of attention as they could potentially be used in super-junction-like devices [26], [38]–[41], [51]. Of course, we consider only undoped structures as doped ones will always have ionized dopants left in the off-state, perturbing the balance (see the corresponding chapter for the details about super-junction-like GaN HEMT devices and charge requirements for it).

Here again, all the middle channels have $n_s^{mid} = p_s^{mid}$ by charge conservation and are all equal between each other. However, the top 2DHG is different and the bottom 2DEG. It is possible to express a particular d_{cap} to match the first 2DHG to the middle 2DHG. However, Schottky barrier height will enter in the expression and, thus, the charge balance would depend on the difficultly controllable surface state. Moreover, the last 2DEG will still be different from his 2DHG (which equals the middle ones).

A less evident but more robust solution is to notice that the mismatched charge in an undoped heterostructure equals the difference between the top 2DHG and the bottom 2DEG:

$$p_s^{top} - n_s^{bot} = \frac{E_g^{ch} - q\Phi_b}{q^2} \frac{\epsilon_{ch}}{d_{cap}}$$

and this quantity is inversely proportional to the cap thickness. Thus, by choosing a thick enough cap, one can achieve charge neutrality. For a typical $Al_{0.3}GaN$ stack 150 nm cap would be enough to make the mismatch below $1 \cdot 10^{12}$ cm^{-2} - a value comparable to the sheet carrier concentration of residual doping in a typical HEMT stack.

2.6 Future work

The proposed model can be completed by studying the detailed properties of the parameter Δ and maybe by providing some considerations to calculate it analytically for a given material.

Moreover, for doped structures, one should consider doing a more detailed analysis of the amount of active doping effectively present in the barrier in order to explain the mismatch between expected and measured carrier concentrations in the middle channels.

Experimental measurement of n_s in each channel separately is challenging but possible in principle.

First, a C-V measurement can be considered in the top capacitance configuration for thin enough structures. If the stack is too thick the anode of the capacitor would probably break way before the last channel is depleted. The same problem occurs for too populated structures where the top gate does not deplete at all [14], all the drop falls between the anode and the first channel, and the capacitor breaks. This method is not very precise as when integrating the capacitance to obtain charge one chooses the integration limits rather arbitrarily (it is difficult to see the exact onset of each channel), introducing an error in the derived charge concentrations.

Another way to perform such a measurement would be to do Hall measurement with the magnetic field sweep and apply methods of quantitative mobility spectrum analysis (QMSA) [52]. This powerful tool could be a promising way to study each channel of the MC-HEMT heterostructure separately.

A more extensive study of undoped multi-channel structures with higher polarization discontinuities, namely InAlN/GaN, would be beneficial to demonstrate thin undoped stacks and compare doped and undoped devices with similar channel stack thicknesses.

All the proposed directions would contribute to a better understanding and experimental description of charge distribution in MC-HEMT structures.

2.7 Conclusion [36]

In this chapter, we have proposed a simple physics-based analytical model for carrier concentrations in doped and undoped multi-channel high-electron-mobility heterostructures. All practically important materials and geometries are considered and a perfect quantitative match between model and simulation is observed. All model parameters have a simple physical explanation and the main trends were derived using only well-known material properties. Model validation against simulation gives less that 2% relative error, showing that provided analytical expressions can fully replace simulations when designing a given stack. Numerical and experimental validation of the model is performed. The main consequences of the model for the channel stack design for a given application are presented.

The model presented provides a set of analytical tools for the ultimate optimization of multi-channel heterostructures and corresponding devices, allowing to fine-tune the carrier concentration profile for a given application and opening new perspectives for better MC-HEMT devices.

3 Intrinsic Polarization Super Junctions

3.1 Motivation

Super Junction (SJ) devices have revolutionized the field of Si power electronics by breaking the one-dimensional unipolar material limit [53], [54]. As discussed in the introduction, for any given on-resistance , the device breakdown voltage has a fundamental, material-only dependent limit. The main reason for this limit is that the maximum field in the off-state is proportional to the number of ionized dopants, which in turn equals the number of electrons conducting in the on-state, strongly linking conduction to the maximum field. If only the drift region could be neutral during the off-state while still having some conductivity in the on-state, the trade-off would be resolved. However, in 1D geometry, using only one type of carriers, such a device is impossible. By employing a 2D doping profile with interchanging p and n pillars it is possible to achieve charge neutrality. Moreover, each junction between two pillars has its own lateral depletion facilitating the depletion of the whole drift region at low voltages and making the field profile more homogeneous. Such a structure that uses interchanging p and n pillars to achieve an almost uniform field profile in the off-state while still preserving bipolar conductivity in the on-state is called super junction and is commercially used in Si-based power electronics [55].

Applied to wide band-gap (WBG) materials, such as GaN, super-junction technology could give a major breakthrough in the field. However, precise p-doping, common in Si, is not yet achievable in GaN. Thus, it is currently almost impossible to make a usual super junction with GaN. However, high mobility heterostructures with similar properties exist.

The unique property of the lateral platform is that the drift region seems to be intrinsically neutral in the off-state as no intentional doping is used in a III-N HEMT. Mobile carriers move out of the properly designed drift region in the off-state. If not, one could use a shorter region reducing the on-resistance as the undepleted part accommodates almost no voltage drop in the off-state but increases the drift region length and, thus, its resistance. Fixed polarization charges always compensate each other. This idea lies behind the concept of Polarization Super Junction [56]–[58].

Yet, as discussed in the previous chapter, one should not forget about ionized surface donor states that also represent fixed charges and do contribute to the field increase in the off-state. In the current research, those charges are either neglected [56]–[58] or their influence is minimized by using doping.

In this chapter, we present a detailed analysis of the working principles of an intrinsic polarization super junction compared to a usual HEMT. We propose a novel robust platform to achieve super junction-like behavior in a GaN HEMT without any doping. We also provide details that were missing in previous works, hindering the full potential of III-N HEMT based super junctions.

This chapter is based on the paper "Intrinsic Polarization Super Junctions: application to single and multi-channel structures" by Luca Nela, Catherine Erine, Amirmohammad Miran Zadeh, and Elison Matioli, submitted [51] and on paper "Figures-of-Merit of Lateral GaN Power Devices: modeling and comparison of HEMTs and PSJs" by Luca Nela, Catherine Erine, Maria Vittoria Oropallo, and Elison Matioli, submitted. Catherine Erine has proposed, analyzed, and simulated the heterostructure, has proposed the model for the off-state depletion of a mismatched HEMT, and has written the code for off-state simulations. Luca Nela together with Amirmohammad Miran Zadeh, Maria Vittoria Oropallo, and Catherine Erine have performed the simulations. Luca Nela has analyzed the depletion behavior and has written the paper.

3.2 State-of-the art

Most GaN-based super junction devices present in literature either employ p-doping in the cap [59]–[61] or consist of alternating n barriers and p channels [38], [39]. In practice, the use of p-doping is very difficult due to the inefficient Mg activation and to its thermal back diffusion [62]. Moreover, the amount of ionized dopants strongly depends on temperature, making the charge balance difficult to maintain, due to the device heating up during operation. Finally, when the p-cap is used, it has to be terminated before the drain to prevent the heavily doped p-GaN from holding the same voltage as the drift region. In that situation, the field peak is just moved to the cap edge (similar to field plates) and is not eliminated [61].

Some previous works have also claimed the demonstration of polarization super junctions without doping by employing usual AlGaN/GaN HEMT heterostructure [56], [57]. However, the epi stack and performance of those devices are the same as usual HEMTs [63], including usual HEMTs presented earlier by the same group [64]. The high breakdown voltage of those devices, attributed to the super junction effect by the authors, was probably just due to the very long gate-drain distance as the average field at the breakdown in the drift region is the same as in usual HEMTs. Although the idea behind the undoped polarization super junction was correct, the authors have neglected the surface states, claiming that 2DHG forms at the top interface of any AlGaN barrier. As shown in the previous chapter, in HEMTs with thin or no cap, ionized surface donors play the role of positive charge instead of the 2DHG. Multi-channel devices proposed by the same authors could behave as super junctions in the middle

channels. Yet, mismatched top and bottom channels were limiting the breakdown to the same value as a usual HEMT. However, those devices do have reduced on-resistance due to their multi-channel nature.

Another very interesting approach to the realization of charge-balanced super-junction consists of employing 3D polarization doping achieved by grading Al composition in the epi stack [65], [66]. This approach (when the p-like pillar is on top and is sufficiently thick) alleviates the problem of top surface states, similarly to the thick GaN cap. Graded polarization doped structures are continuous equivalents of GaN/(AlGaN/GaN)xN/GaN structures analyzed in this thesis and share similar physical principles. However, the realization of such epi-structures is probably less direct within current industrial growth techniques than single-channel structures with thick cap and even multi-channel stacks.

To fully explore the potential of polarization super junctions, we have performed extensive theoretical and numerical work. As a result, we proposed a simple and robust platform for such devices - intrinsic polarization super junction (iPSJ). The proposed structure can be fabricated using current commercial fabrication methods, it does not need any precise doping control, and is independent of the top surface state. Moreover, we show how to apply the same concept to multi-channel heterostructures to create a device with optimal breakdown voltage (due to super junction effect) and low on-resistance (multiple channels) - multi-channel intrinsic polarization super junction HEMT (MC-iPSJ HEMT). MC-iPSJ HEMT fully resolves the trade-off between the on-resistance and breakdown voltage by decoupling the off-state field from the carrier concentration in the on-state.

3.3 Heterostructure design

By applying the model presented in the previous chapter to the single channel case one can obtain the following expressions for 2DEG and 2DHG sheet carrier concentrations in presence of 2DHG:

$$n_s = \Delta\sigma - \frac{E_g^{ch} + \Delta}{q^2}\frac{\epsilon_b}{d_b}$$

$$p_s = \Delta\sigma - \frac{E_g^{ch} + \Delta}{q^2}\frac{\epsilon_b}{d_b} - \frac{(E_g^{ch} - q\Phi_b)}{q^2}\frac{\epsilon_{ch}}{d_{cap}}$$

Those two quantities are different with a mismatch Δ_{mm} of:

$$\Delta_{mm} = n_s - p_s = \frac{E_g^{ch} - q\Phi_b}{q^2}\frac{\epsilon_{ch}}{d_{cap}}$$

The mismatch between 2DEG and 2DHG depends on Schottky barrier height. However, if a thick enough cap is chosen the mismatch can be minimized whatever is the Schottky barrier.

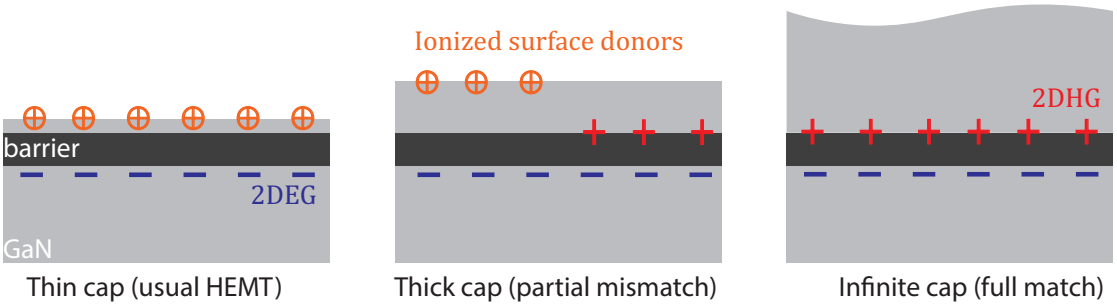

Figure 3.1 – Left: Usual HEMT all the electrons in the 2DEG come from surface donor states; Center: Thick enough cap, some electrons come from the surface others from the valence band on the other side, leaving a 2DHG behind. The mismatch $\Delta_{mm} = n_s - p_s$ equals the number of ionized surface states Right: Infinite cap that leads to an ideal match as all the electrons come from the valence band on the other side.

This fact is very interesting as it means that one can match mobile charges independently of the state of the metal/cap interface.

Moreover, as the whole structure has to be neutral and all the polarization charges are compensated by their nature the Δ_{mm} has to be compensated by the charge on the metal. By choosing a thick enough cap, one minimizes the amount of mobile charge on the metal electrode (fixed polarization at the GaN top surface is always there) as all the electrons rather come from the valence band on top of the barrier, leaving a 2DHG behind.

Let us now consider a free surface without a metal electrode. As discussed in the previous chapter, a large density of surface donor states at energy E_D below the conduction band is present at the cap (or barrier, if no cap) surface. As the density is high, it is reasonable to think of those states as a metal creating a Schottky barrier of height E_D.

If the cap is below the critical thickness d^*_{cap} (see previous chapter for derivations):

$$d^*_{cap} = \epsilon_{ch} \frac{\dfrac{E_g^{ch} - E_D}{q^2}}{\Delta\sigma - \dfrac{E_g^{ch} + \Delta}{q^2} \dfrac{\epsilon_b}{d_b}},$$

no 2DHG is formed and all the electrons in the 2DEG come from surface states (see Fig. 3.1, left), leaving an equivalent amount of fixed positive charge in the form of ionized surface donor states. n_s is given by the following expression:

$$n_s = \frac{1}{q} \frac{q\Delta\sigma - \dfrac{1}{q}\dfrac{\epsilon_b}{d_b}(E_D + \Delta)}{1 + \dfrac{\epsilon_b}{\epsilon_{ch}} \dfrac{d_{cap}}{d_b}}$$

and it depends on the E_D ($q\Phi_b$). Mobile charges are fully mismatched: $\Delta_{mm} = n_s$. In the off-state, the drift region will have a total charge of $\Delta_{mm} = n_s$ as mobile electrons will be depleted to the drain (cathode) electrode and fixed positive ionized surface dopants would stay. This is the case of usual HEMT.

Now, when one increases the cap thickness above d^*_{cap}, 2DHG appears and 2DEG loses its dependence on E_D:

$$n_s = \Delta\sigma - \frac{E_g^{ch} + \Delta}{q^2}\frac{\epsilon_b}{d_b}$$

However, the newly appeared 2DHG now interacts with the surface:

$$p_s = \Delta\sigma - \frac{E_g^{ch} + \Delta}{q^2}\frac{\epsilon_b}{d_b} - \frac{(E_g^{ch} - E_D)}{q^2}\frac{\epsilon_{ch}}{d_{cap}} = n_s - \Delta_{mm}$$

Here one can see that 2DHG gives all the electrons to the 2DEG except those that create the mismatch - the ones still coming from the surface. This hypothesis is confirmed by simulations using Silvaco Atlas: Δ_{mm} always equals the number of ionized dopants. Thus, in such an intermediate case, part of electrons come from the valence band and part from the surface donor states. One can also consider the same thing with a different interpretation: 2DHG of equal density to the 2DEG one forms, but then it is partially compensated by electrons coming from surface donors (see Fig. 3.1, center). Partial mismatch $\Delta_{mm} = n_s - p_s < n_s$ is present in the heterostructure. During the off-state mobile 2DEG will be depleted to the drain (cathode) and mobile 2DHG to the gate (anode) and the drift region will be left with a net charge of Δ_{mm}, equal to the number of ionized dopants left.

We do not consider possible modification of dopant ionization by the gate /anode (virtual gate effect). Although this effect is beneficial for reducing the charge of the drift region in the off-state, this degrades the on-performance due to trapped charges. Thus, a well-designed HEMT should not rely on this effect.

As Δ_{mm} is inversely proportional to the d_{cap}, it is easy to imagine the other limit of cap thickness - an infinite cap. In this case, no mismatch would be present, all the electrons come from the valence band and surface states are not ionized. This would be an ideally matched device and the drift region in the on-state would be neutral. Such a device would present an ideal super junction behavior: it easily conducts through the 2DEG in the on-state (2DHG is usually negligible due to low mobility and high contact resistance) and the drift region is neutral in the off-state. The drift region, being neutral, presents the best possible field profile - a flat uniform field. Carrier concentration in the on-state is fully decoupled from the maximum field in the off-state.

Even if the ideal infinite cap situation can not be reached, one can always reduce Δ_{mm} as much

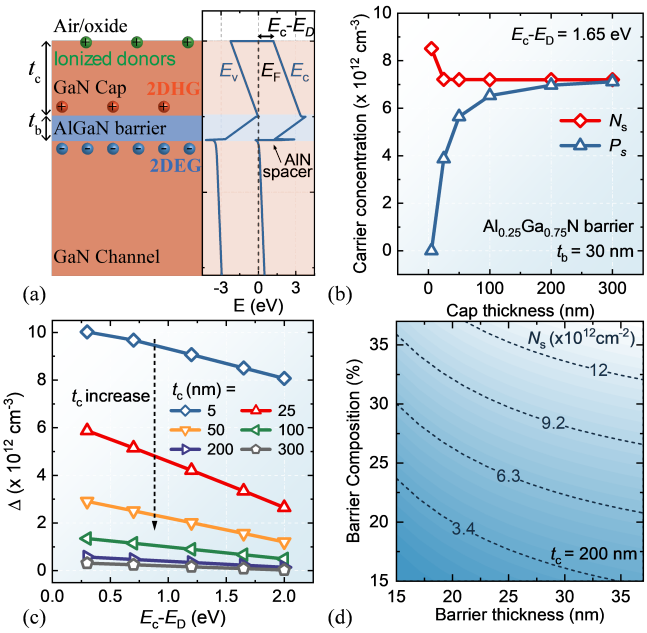

Figure 3.2 – (a) Schematics and band structure of a thick cap HEMT. (b) n_s and p_s dependence on cap thickness, Δ_{mm} is reducing with the cap thickness. (c) Mismatch vs donor state energy for different cap thicknesses. For thick enough cap the mismatch is independent of the surface state (d) n_s for different barrier thicknesses and compositions when a 200 nm cap is used. High n_s is achievable within commonly used thicknesses and compositions. [51]

as needed by employing a thick enough cap. By reducing Δ_{mm} one reduces the maximum field in the off-state and increases the maximum voltage that the drift region can hold. Thus, by varying d_{cap} the device continuously passes from a usual HEMT with a full mismatch to the ideal case of a fully-matched super junction. Even if the ideal case is never reached any reduction of Δ_{mm} is beneficial.

We performed an extensive numerical study of thick-cap $Al_{0.25}GaN/GaN$ structures in order to demonstrate the feasibility of the proposed structures.

Fig. 3.2 (a) shows the schematics of the structure under consideration.

In Fig. 3.2 (b) we show n_s and p_s as a function of cap thickness for a typical E_D of 1.65 eV [13], [34] in a commonly used $Al_{0.25}GaN/GaN$ heterostructure employing 1 nm AlN interlayer and 30 nm barrier. One can clearly see the mismatch reducing when cap increases. Moreover, for the cap thickness of only 200 nm the mismatch is already reduced to less than $0.5 \cdot 10^{12}$ cm^{-2}, compared to $1 \cdot 10^{13}$ cm^{-2} of a fully mismatched usual thin cap HEMT. Further reducing Δ_{mm} presents no interest in practice as residual unintentional doping of a typical HEMT stack would be of the order of $0.1 - 1 \cdot 10^{12}$ cm^{-2} and it contributes to the charge mismatch in the same way.

In Fig. 3.2 (c) we sweep E_D for different cap thicknesses to show that for a thick enough cap

the mismatch is not only small but also independent of E_D and, thus, the state of the surface. It is extremely important to achieve this property as the exact configuration of the top surface is almost impossible to control during growth, different fabrication steps, and exposure to the environment.

Furthermore, thick cap is known to reduce n_s. In Fig. 3.2 (d) we show that with typical barrier thicknesses of 20-40 nm and typical compositions of 25-35% it is possible to achieve high carrier concentrations $n_s > 0.8 \cdot 10^{13}$ cm^{-2} even when a 200 nm cap is employed.

Finally, some concerns exist as to the experimental demonstration of the presence of high-density 2DHG in such structures. Although it is tough to provide a contact exclusively to the 2DHG without contacting 2DEG as well, some groups have experimentally measured and studied 2DHGs in III-N HEMTs [67]–[69]. For that, a p-GaN cap was employed to provide contact to the 2DHG. Though the cap was not later removed, the presence of 2DHG was clearly identified by temperature-dependent Hall measurements and densities as high as $0.8 \cdot 10^{13}$ cm^{-2} for usual AlGaN/GaN were reported [67].

To summarize, we have demonstrated that by employing a thick cap one obtains an undoped heterostructure with zero total fixed charge and compensated mobile charges, independent of the state of the top surface. We also showed that such a structure is easily achievable in practice, using commonly employed barrier thicknesses and compositions. In the following, we numerically analyze a diode based on such heterostructure and demonstrate its super junction behavior.

3.4 Fully matched intrinsic polarization superjunction diode

Once the design of the appropriate heterostructure is performed, we consider a diode based on a fully matched super junction stack.

It is worth noticing that transistors and diodes are very similar when it comes to on-resistance vs breakdown voltage analysis. In the off-state, gate-drain region behaves exactly the same as a Schottky diode. As the barrier thickness is way smaller than gate-to-drain distance (L_{gd}), one can neglect all the 2D effects as they are important only at low voltage when the depletion region is very small. The on-resistance of the power transistor is also mainly defined by L_{gd} as this is the longest part of the channel.

Fig. 3.3 (a) shows the schematics of the device under consideration.

The heterostructure used for the analysis comprises a 30 nm thick $Al_{0.25}GaN$ barrier and a 200 nm thick UID-cap, leading to n_s of $0.8 \cdot 10^{13}$ cm^{-2}. The anode to cathode distance (L_{AC}) is 10 μm. The cathode forms ohmic contact to the 2DEG and Schottky to holes and the anode vice versa. The ohmic contact to the holes is realized through the top p++ ($N_A = 2 \cdot 10^{18}$ cm^{-3}) GaN layer and a metal electrode, which is connected to the anode. In practice this can be realized by including the p++ cap in the heterostructure with further self-aligned etching of the parts

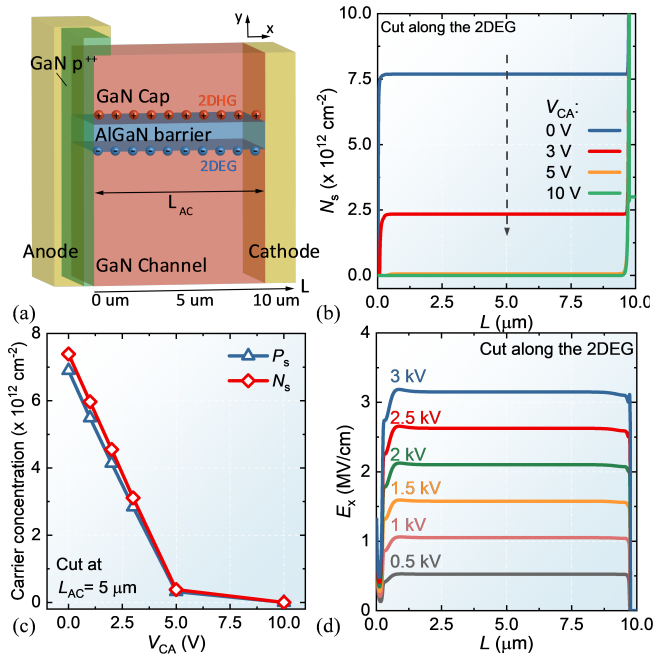

Figure 3.3 – (a) Schematics of the device under consideration (b) n_s profile in the drift region for different anode voltages. 2DEG is uniformly depleted over the whole drift region. (c) n_s, p_s vs V_{AC}: full depletion occurs around 5 volts. [51]

not covered by electrodes.

First, we study the depletion behavior under reversed bias of the proposed device.

In a unipolar Schottky diode or, as we show in the next section, in a usual HEMT when a reverse bias is applied a depletion zone appears next to the anode. When the anode voltage is increased (in magnitude), the depletion zone slowly grows. Thus, in a usual device, the voltage drop always occurs in a region shorter than L_{AC}.

In the super junction device, we propose, the situation is different. We observe a uniform depletion of the 2DEG in the whole drift region (see Fig. 3.3 (b)), full depletion occurs at only 5V. Thus, the voltage drop is always accommodated by the whole region, minimizing the average field. Such a depletion behavior can be explained by the fact that 2DHG, being connected to the anode, passes the anode voltage on top of the 2DEG, acting as a usual top gate.

Holes and electrons are depleted at a very low voltage of 5 V (see Fig. 3.3 (c)), leaving behind a neutral drift region with a uniform field profile (see Fig. 3.3 (d)).

Thus, an ideal intrinsic polarization diode gets depleted with just few first volts of the reverse bias and further presents an ideal uniform field profile in the drift region.

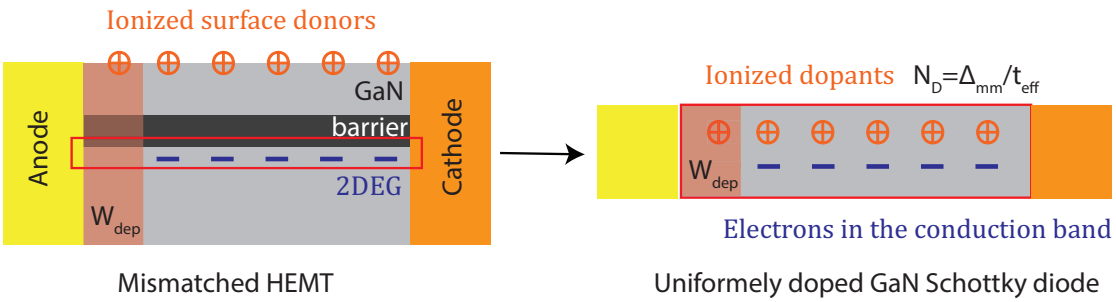

Figure 3.4 – Equivalence between an effective uniformly doped device and a mismatched HEMT

3.5 Partially mismatched intrinsic polarization super junction diode

Achieving an ideally matched heterostructure is impossible in practice. However, one can significantly reduce the mismatch by employing a thick enough cap. For that, one has to analyze the depletion behavior of partially- and fully-mismatched HEMTs.

It is instructive to first remind the depletion behavior of a usual uniformly n-doped Schottky capacitor. When a reverse voltage is applied, a depletion zone forms next to the anode and propagates towards the cathode with increasing voltage. The charge density in the depletion is equivalent to the doping N_D (we suppose full ionization) and the field profile is linear, given by:

$$E_x = \frac{qN_D}{\epsilon}(x - W_{dep})$$

The depletion is given by:

$$W_{dep} = \sqrt{\frac{2\epsilon V_{AC}}{qN_D}}$$

and it grows as a square root of the applied reverse bias. We neglect the Schottky barrier for simplicity as it affects only very low voltage behavior.

From the simulations of the off-state behavior of the Schottky HEMT, we have found out that Schottky HEMT under reverse bias can also be considered in a first approximation as a uniformly n-doped Schottky diode with the doping equivalent to $\frac{\Delta_{mm}}{t_{eff}}$, where t_{eff} has the dimension of length (see Fig. 3.4).

In Fig. 3.5 we present extracted from simulations the depletion and field profiles of a usual HEMT (full mismatch) and an ideal iPSJ HEMT (no mismatch). One can see that a usual HEMT presents a typical square root depletion while the iPSJ one very quickly fully depletes the whole drift region as explained above. A smaller depletion in a usual HEMT leads to a non-uniform, peaked field profile.

In the model we propose, we replace the peaked field profile, which is difficult to treat analyti-

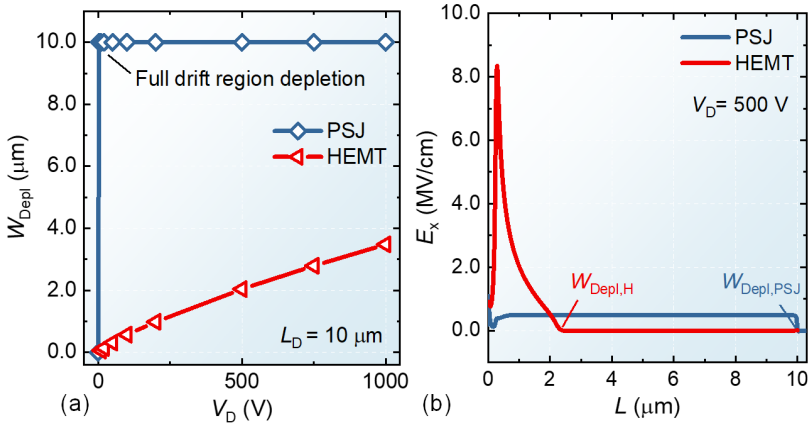

Figure 3.5 – (a) W_{dep} vs voltage for a usual HEMT and for a PSJ HEMT (b) Field profiles in a usual HEMT and in PSJ HEMT [70]

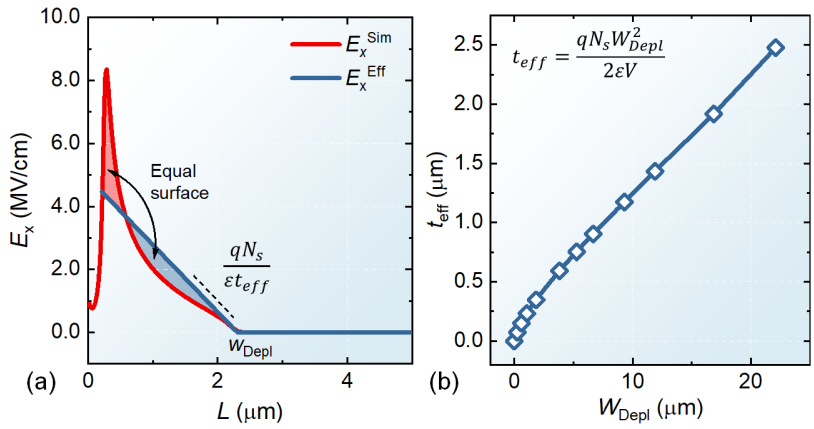

Figure 3.6 – (a) Simulated off-state electric field along L_D in the 2DEG region for a HEMT device and corresponding approximated linear field profile assumed in the model (b) t_{eff} as a function of the depletion width extracted from the device simulation. [70]

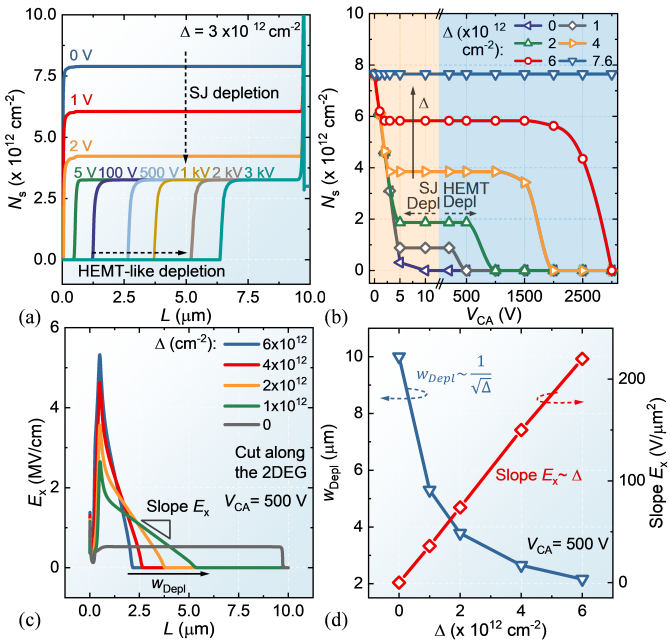

Figure 3.7 – (a) Depletion of a partially matched diode. (b) Sheet carrier concentration in the center of the drift region vs anode voltage (c) Field profiles for partially matched diodes with different Δ_{mm} [51]

cally, by an effective linear field with the same voltage drop (see Fig. 3.6 (a)). This assumption is advantageous to usual HEMTs as a linear profile is more uniform than the peaked one present in the real device. The geometrical parameter t_{eff} accounts for the 2D distribution of the electric field between the gate electrode and the gate edge of the undepleted 2DEG. For this reason, it only depends on the device geometrical parameters, such as the gate metal thickness and the dielectric constant of the passivation layer, and the depletion width, while it is independent on N_s. In particular, t_{eff} increases as W_{dep} grows to account for the more 2D shape of the electric field (Fig. 3.6 (b)). While a mathematical expression for t_{eff} is challenging to obtain, its value can be extracted from simulation using the expression:

$$t_{eff} = \frac{q\Delta_{mm}W_{dep}^2}{2\epsilon V_{AC}}$$

When a partial mismatch exists, the devices present hybrid behavior: first, a uniform depletion of 2DEG and 2DHG occurs till the 2DHG disappears, then the device behaves as fully mismatch HEMT with a mismatch of Δ_{mm}, with a depletion zone slowly propagating from anode to cathode and the field with an average slope proportional to Δ_{mm}. Fig. 3.7 (a) illustrates this behavior. Fig. 3.7 (b) shows a cut of the carrier concentration profile at the middle of drift region vs voltage for different mismatches. A fully mismatched device is not even half depleted even at V_{AC} of 2000 V, while devices with smaller mismatches get depleted way easier. Field profiles for different mismatches are provided in Fig. 3.7 (c), the slope of the field

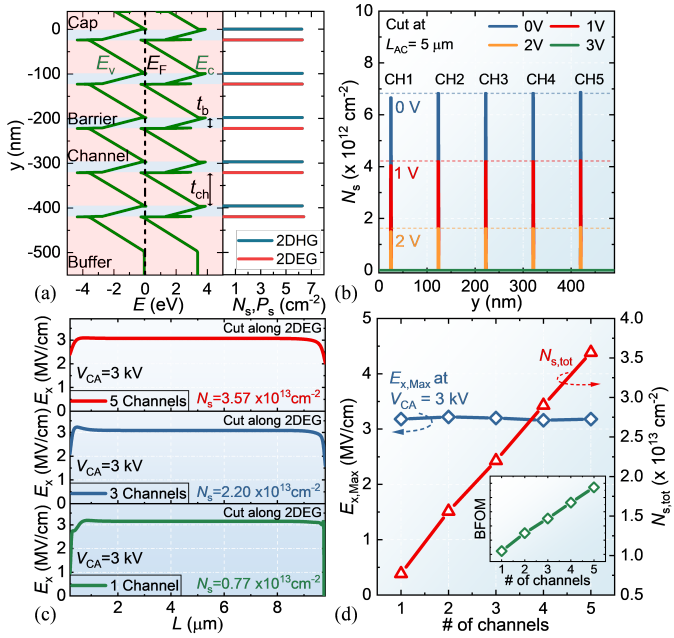

Figure 3.8 – (a) Schematics and band structure of the multi-channel device under consideration (b) Simultaneous depletion of all the channels with only few volts of reverse bias (c) Field profiles in top, middle and bottom channels (d) Maximum field and carrier concentration vs number of channels *Inset(Scaling of Baliga's figure of merit. [51]

is proportional to the mismatch, leading to more peaked profiles for devices with a higher mismatch. Finally, Fig. 3.7 (c) shows the dependence of W_{dep} and slope of the field profile on Δ_{mm}, showing the results in accordance with the model proposed.

In summary, even if a fully matched device can not be reached, reducing Δ_{mm} significantly reduces the maximum field and facilitates the depletion. Thus, a thick-cap heterostructure with low mismatch allows to reduce the maximum field and increase the breakdown voltage with respect to a usual fully mismatched HEMT.

3.6 Multi-channel intrinsic polarization super junction diode

The same concept of iPSJ can be applied to the multi-channel structure. Each period of a matched multi-channel structure would act similarly to a single-channel iPSJ but the whole structure will have a reduced sheet resistance. Fig. 3.8 (a) shows a schematics of an undoped 5-channel structure simulated. In Fig. 3.8 (b) one can see that all the 5 channels are depleted simultaneously. Fig. 3.8 (c) shows a uniform field profile in each of the channels. Fig. 3.8 (c) shows that the maximum field in the structure is independent of the number of channels, while N_s scales linearly with the number of channels. Thus, one fully decouples the off-state from the on-state and can now scale the BFoM (Fig. 3.8 (d) inset) in a similar way.

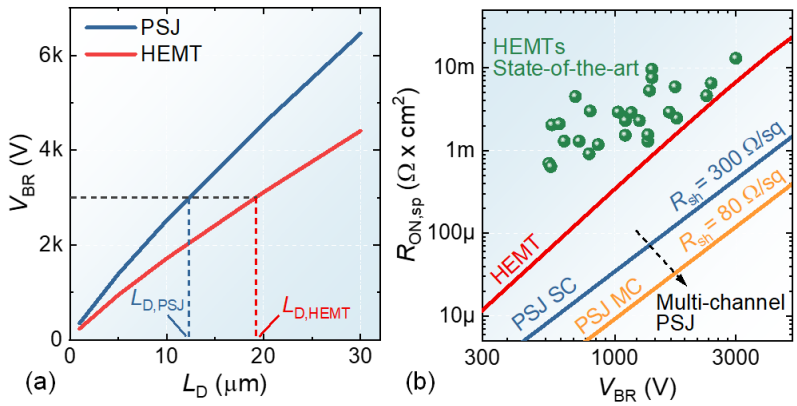

Figure 3.9 – (a) Breakdown voltage as a function of the drift region length for a HEMT and a PSJ device. Complete L_D depletion is assumed for HEMTs. (b) $R_{ON,SP}$ vs V_{BR} benchmark for HEMTs and PSJs with single and multiple channel heterostructures (SC and MC respectively). Electron mobility of 2000 cm2/Vs was used. The performance of state-of-the-art devices in literature is reported in green.[70]

3.7 Baliga's figures of merit of usual and PSJ HEMTs [70]

Based on the electric field profiles for HEMTs (described in Section 3.5) and PSJs (uniform) , we can compare the DC performance of the devices. The breakdown voltage (V_{BR}) is typically obtained by considering the onset of avalanche breakdown by impact ionization, with the ionization integral being simplified by using Fulop's power law [71], [72]. Solving the resulting ionization integral and considering a complete L_D depletion, as in the case of a well-designed power device, one obtains an important relation between V_{BR} and the drift region length:

$$V_{BR,PSJ}[V] = 0.95 \cdot 10^6 L_{D,PSJ}^{6/7}[cm]$$

$$V_{BR,HEMT}[V] = 0.64 \cdot 10^6 L_{D,HEMT}^{6/7}[cm]$$

These expressions, which depend only on the E_x profile and not on the carrier concentration, set an important relation between the drift region length of PSJs and HEMTs. In particular, for a given V_{BR}, $L_{D,PSJ} = L_{D,HEMT}$, which means that PSJ devices can have a shorter drift region to hold the same voltage thanks to the improved off-state electric field profile (Fig. 3.9 (a)). Besides, one obtains also a relation between V_{BR} and N_s for HEMTs:

$$V_{BR,HEMT}[V] = 2.51 \cdot 10^{15} \left(N_{s,HEMT}[cm^{-2}] t_{eff}[cm]\right)^{-3/4}$$

while, thanks to the very small value of voltage at which 2DEG is fully depleted for any realistic carrier concentration, in a first approximation V_{BR} does not depend on N_s in PSJs.

For a lateral device, the specific on-resistance ($R_{ON,SP}$) is given by:

$$R_{ON,SP} = \frac{L_D^2}{q\mu N_s}$$

with μ the electron mobility. From above expressions, one can extract the expression of the device $R_{ON,SP}$ as a function of V_{BR}, which represents the main figure-of-merit to assess power devices DC performance:

$$R_{ON,sp,HEMT}[\Omega \cdot cm^2] = \frac{5.2 \cdot 10^{-16}}{\mu[\frac{cm^2}{V \cdot s}]t_{eff}[cm]} V_{BR}[V]^{11/3}$$

$$R_{ON,sp,PSJ}[\Omega \cdot cm^2] = 1.15 \cdot R_{sh}[\Omega/sq]V_{BR}[V]^{2.3}$$

where R_{sh} is the heterostructure sheet resistance and t_{eff} can be obtained from Fig. 3.6 (b). A significant improvement in the $R_{ON,sp,PSJ}$ vs V_{BR} limit can be achieved by PSJs using conventional AlGaN/GaN single-channel heterostructures (R_{sh} 300 Ω/sq), with a reduction up to 10 times in the specific on-resistance for a given breakdown voltage (Fig. 3.9 (b)). It should be noted that often the electric field profile of HEMT devices is approximated to be flat in the whole L_D, which however erroneously results in the same $R_{ON,sp}$ vs V_{BR} limit as for PSJ devices. The commonly used in literature "GaN HEMT limit", taken from Baliga's paper [71] is derived under this uniform field profile. Nevertheless, as previously explained, such an assumption is not physically accurate and leads to an overestimation of the potential of HEMT devices. This explains why real HEMTs present performance very far from this limit, which are instead properly described by the proposed model (Fig. 3.6).

In addition, we observe that for HEMTs V_{BR} depends on N_s and thus the carrier concentration does not appear in the final trade-off. This is the usual situation for conventional semiconductor devices for which there is a trade-off between the carrier concentration and the blocking capabilities. On the contrary, R_{sh} (and thus N_s) is a free parameter for PSJs, which allows increasing the device conductivity without affecting the breakdown voltage. While similar considerations would hold for single-channel heterostructures with low sheet resistance, an effective way to reduce the heterostructure R_{sh} is the use of multiple parallel channels, which enable to increase the carrier concentration without degrading the mobility.

As shown in Fig. 3.9 (b), the reduced sheet resistance of multi-channel PSJ devices would enable a further improvement in the $R_{ON,sp}$ vs V_{BR} trade-off, resulting in a decrease of the device resistance without affecting its off-state behavior.

3.8 Future work

The next steps of this project include the experimental demonstration of single- and multi-channel iPSJ HEMTs. While a SC-iPSJ HEMT can be fabricated quite straightforwardly using existing techniques, MC-iPSJ HEMT still presents some difficulties. The major one is the de-

velopment of a regrown p contact that would be ohmic to holes but still Schottky to electrons.

Dynamic characterization of iPSJ HEMTs is also a very interesting topic as a priory those devices should not need surface passivation to present a good dynamic R_{on} as 2DEG and 2DHG are completely independent of the state of the surface.

SC- and MC-PSJ HEMTs open new perspectives for major advances in the performances of GaN power HEMTs.

3.9 Conclusion

In this work, we propose a simple and robust approach to realize intrinsic PSJs with negligible mismatch by the use of a thick undoped GaN cap layer. Devices based on this structure offer excellent carrier depletion and a flat electric field profile regardless of the N_s value, paving the way to a significant improvement of power devices' performance.

4 Electronic transport in multi-channel nanowires

4.1 Motivation

Multiple 2DEG channels of a MC-HEMT can not be controlled by a conventional top gate (see Fig. 4.1) and a 3D tri-gate geometry is necessary to obtain efficient and simultaneous control of all the multiple channels. Moreover, a typical MC-HEMT (Fig. 4.2) also contains nanowire termination between the edge of the gate and the drain to prevent premature breakdown.

As the average carrier concentration in the nanowire reduces with its width due to the side-wall depletion and possible strain relaxation, one can adjust the threshold voltage of the devices by controlling the width of the nanowire under the gate (Fig. 4.1). Thus, by using a slanted nanowire one continuously changes the threshold voltage through the slant, creating a structure very similar to a slanted field plate on top of usual HEMT (Fig. 4.2).

Moreover, for a multi-channel structure, the usual top field plate only degrades the device performance. As the top gate can not deplete multiple 2DEGs, the top field plate can do that neither. Thus, by leaving gate metal on top of the planar multi-channel region, one creates an extremely high voltage drop between the undepleted 2DEG under high voltage V_D and gate with voltage V_G over a very short distance of just one or two periods of the multi-channel stack (top channels can be partially depleted) plus the oxide. This creates a high field (see Fig. 4.3) that leads to a very early breakdown.

To avoid the detrimental effect of having metal on top of a planar multi-channel stack, one has to terminate the gate at the nanowires (Fig. 4.4), extending the depletion region for a given voltage drop and, thus, reducing the maximum field.

After performing all the analysis presented above on simulated and experimental devices we realized the crucial role of the nanowires and the importance of precise knowledge of their properties (carrier concentration, mobility, sheet resistance) in different parts of the device. Thus, we decided to perform an extensive study of electronic properties of top-down etched single- and multi-channel nanowires.

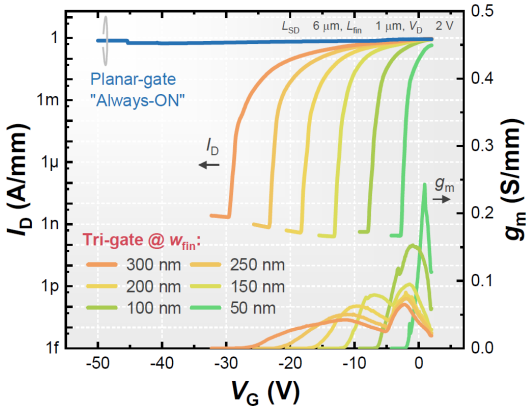

Figure 4.1 – Transfer characteristics of planar and tri-gate MC-HEMTs. A planar transistor with only the top gate is impossible to turn off even at $V_G = -50\ V$ - voltage at which the gate oxide breaks. However, by using tri-gate one can tailor the threshold voltage and merge multiple transconductance peaks in a single one. [12]

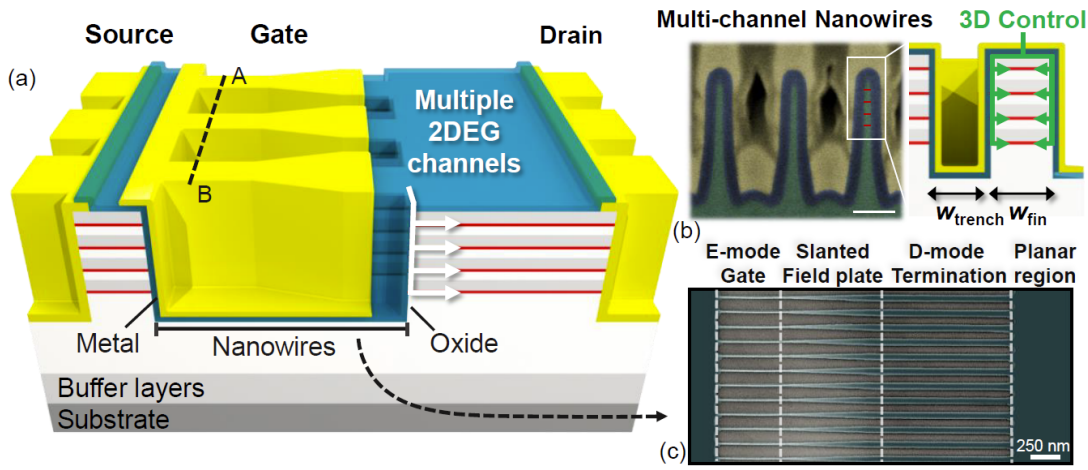

Figure 4.2 – (a) Schematics of an MC-HEMT. Nanowires under the gate are needed to control the threshold voltage by adjusting carrier concentration and increasing gate control through additional sidewall gating. The slanted part acts as a field plate. (b) SEM image and schematics of the cross-section of a MC-HEMT in the gate region. Tri-gate geometry adds sidewall control on top of the usual one and sidewall depletion of the nanowire reduces average carrier concentration, creating efficient and simultaneous 3D control of all the channels (c) Top-view SEM image of the gate and gate-to-drain regions before metal deposition. The thinner part of the nanowire defines the desired threshold voltage while the slanted part acts as a field plate. Nanowire termination after the gate is required to prevent premature breakdown. [14]

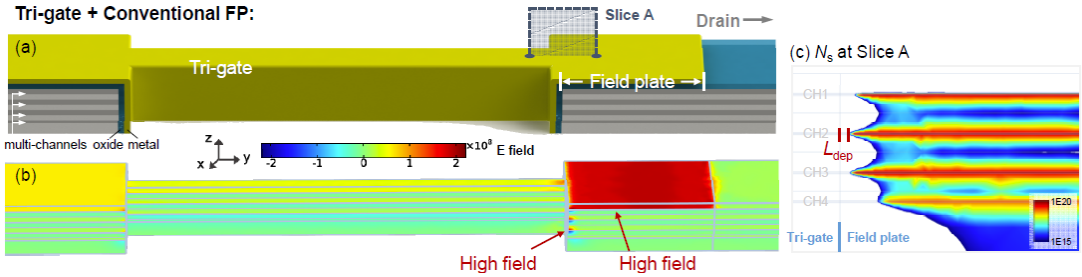

Figure 4.3 – (a) 3D Schematics (b) COMSOL simulation of the field distribution in a tri-gate MC-HEMT with a usual planar field-plate. High-field regions are situated between the planar metal and the undepleted MC stack as well as on the side face. [12]

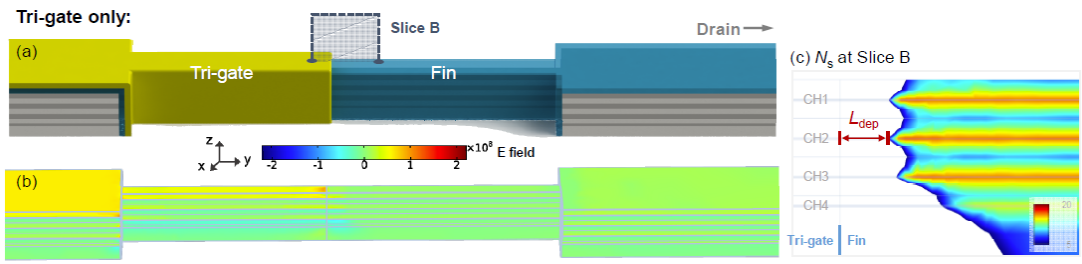

Figure 4.4 – (a) 3D Schematics (b) COMSOL simulation of the field distribution in a tri-gate MC-HEMT with nanowire termination. The maximum field is significantly reduced as depletion is facilitated by lower carrier concentration and absence of co-planar undepleted region accommodating a high voltage drop [12]

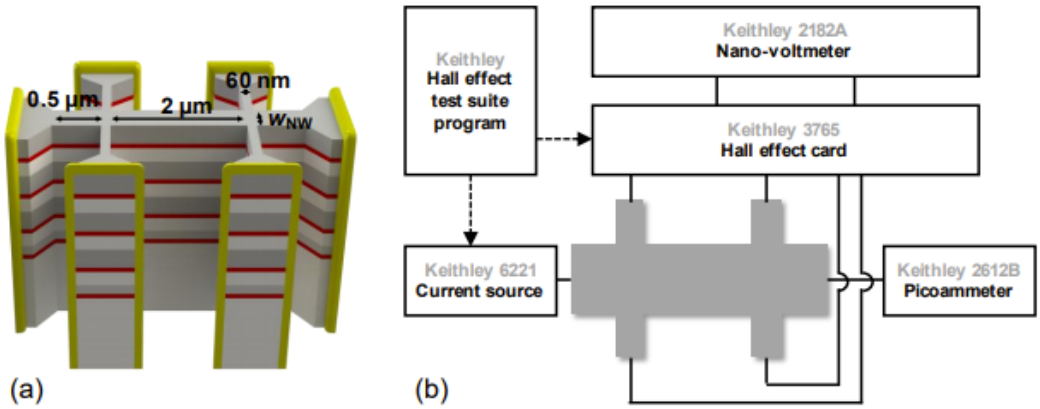

Figure 4.5 – (a) Schematics of a Hall bar used for measurements. (b) Measurement setup employed. A permanent magnet of 0.345 T was used for magnetic field, for field reversal it was mechanically flipped to the other side [14]

During this thesis, I have performed a full Hall characterization of gated and ungated single- and multi-channel nanowires. The results presented below lead to the design of MC-HEMTs that outperformed state-of-the-art devices. In addition, we propose a semi-empirical model for the temperature behavior of carrier concentration in single-channel nanowires. This model opens interesting perspectives for the analysis of the sidewall surface states in tri-gate devices.

4.2 Nanowire Hall bar measurements

To characterize sheet resistance, carrier concentration, and mobility we have designed nanowire Hall bars. Both the bar and leads to measure longitudinal and transverse voltages were formed during the same mesa etch step with an ohmic contact deposited further on the pads. The layout of the nanowire employed as well as measurement schematics are presented in Fig. 4.5.

Hall bar mesa was defined by e-beam lithography and etched. All the etchings were performed in Cl_2-based inductively coupled plasma (ICP). Then ohmic contact was formed using one optical lithography followed by metal deposition, lift-off, and annealing. A metal stack consisting of Ti (200 Å)/ Al (1200 Å)/ Ti (400 Å) / Ni (600 Å) / Au (500 Å) was deposited by electron-beam evaporation and annealed at 860 °C. Hall measurements were performed in 6-lead Hall bar geometry following the procedure from Lake Shore 7500/9500 Series Hall System User's Manual, using Keithley 6221 current source, 2182A nano-voltmeter, 2612B source-measurement unit as picoammeter, 3765 Hall Effect card as a switch and permanent 0.345 T magnet (field measured by gaussmeter on the chuck). Current and field reversal and homogeneity checks were performed to minimize errors. In each case, measurements were performed over at least 4 Hall bars in different parts of the chip.

In order to characterize the error induced by the leads being of the size comparable to the

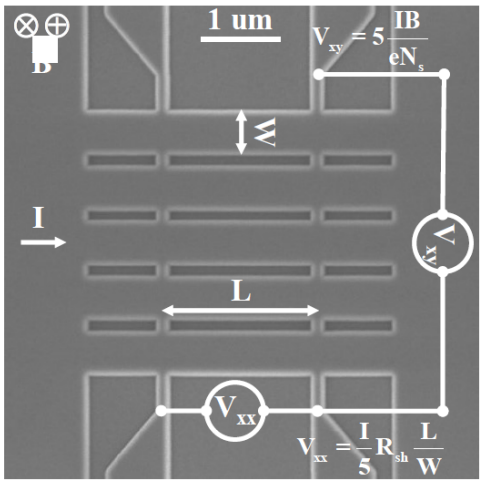

Figure 4.6 – Top-view SEM image of the 5-nanowire Hall bar and measurement schematics

nanowire itself, we performed COMSOL simulations for the same geometry. Geometrical errors were found to be below 5% for all relevant carrier concentrations, sheet resistances, and widths.

To increase the signal from small nanowires in some cases multiple parallel bars were present within the same device (see Fig. 4.6). There was no difference in average values of sheet resistance, carrier concentration, and mobility between single and multi-nanowire devices neither in numerical simulations nor during the experimental checks. However, a single nanowire Hall bar presented a bigger variance among devices due to random defects and impurities present over the chip. Using an N-nanowire Hall bar is equivalent to measuring N single nanowire Hall bars, thus, increasing the number of devices to average and reducing the error bar.

To characterize the nanowires in the gate region, a gate electrode was added on the top of the Hall bars and a usual Hall measurement was performed at each gate voltage.

4.3 Achieving normally-off MC-HEMT

The ability to tailor the threshold voltage (V_{TH}) by employing different nanowire widths opens an important way to achieve normally-off behavior in a MC-HEMT, necessary for the safe operation of any power transistor.

However, to achieve positive V_{TH} in a multi-channel structure one has to employ very small 20 nm nanowires. The nanowire part becomes the most resistive part of the devices and concerns rise as to the possibility to recuperate decent mobility and carrier concentration by applying a positive gate voltage. We performed a detailed study of gated nanowire Hall bars together with

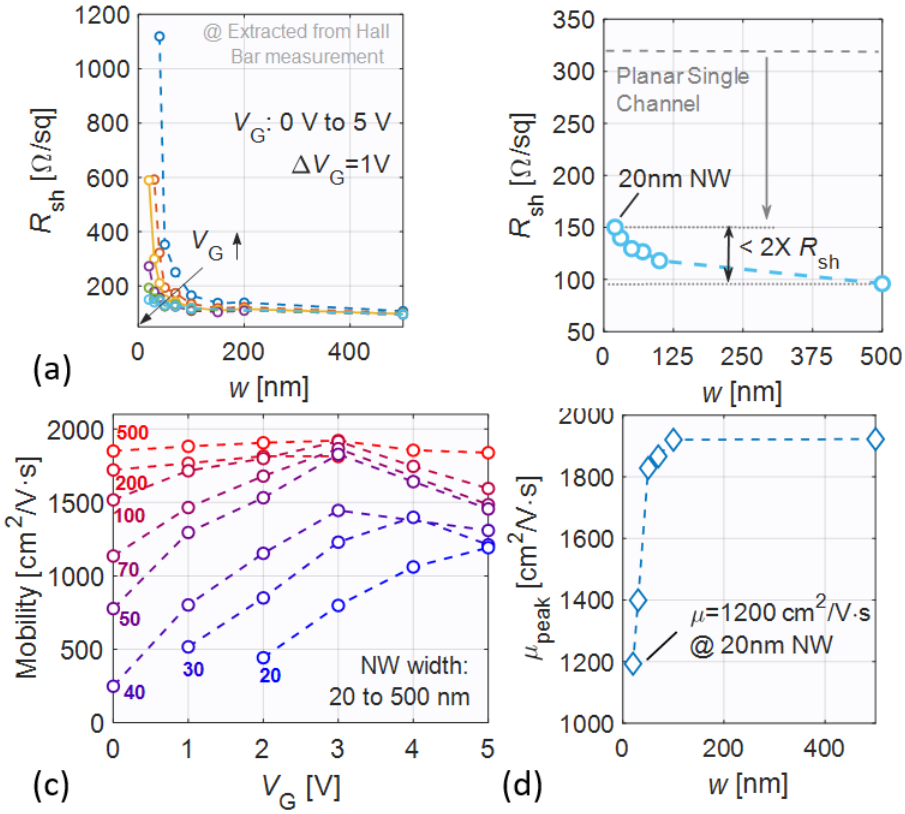

Figure 4.7 – (a) Sheet resistance vs nanowire width for different gate voltages. By applying a positive gate voltage one reduces the sheet resistance of the nanowire and opens the channel. Smaller is the nanowire, bigger is the swing of the resistance. (b) Sheet resistance vs width at $V_G = 5V$. Even a 20 nm nanowire is less than twice as resistive as the planar one, showing that by applying the gate voltage one almost fully recovers the conductivity (c) Mobility vs V_G for different nanowire widths. By applying positive gate voltage one recuperates the mobility. (d) Maximum mobility vs nanowire width. Even a 20 nm nanowire has a high mobility of 1200 cm^2/V·s

a real tri-gate device in order to address those questions.

By measuring sheet resistance (R_{sh}) vs nanowire width (w) at different gate voltages (V_G) we found that by applying a positive gate voltage one effectively recuperates the conductivity (Fig. 4.7 (a)). Moreover, by plotting the maximum conductivity (at $V_G = 5V$, Fig. 4.7 (b)) vs nanowire width we could see that a tiny 20 nm nanowire was less then twice more resistive then a planar wafer ($R_{sh}^{planar} = 80\ \Omega/\square$). Meaning that one can recuperate as much as 150 Ω/□ in a 20 nm multi-channel nanowire by applying $V_G = 5V$. To compare, a typical resistance of a single channel wafer is 300 Ω/□, almost twice as big. Thus, etching the nanowire does degrade the conductivity, but it still remains comparable to the single-channel planar conductivity (even if the filling factor is taken into account). This degradation happens only in a tiny region under the gate, necessary to provide the normally-off behavior, while the major part of the

multi-channel device is more than 3 times more conductive than a planar single-channel one.

Moreover, when we measured mobility (μ) vs gate voltage at different nanowire widths (Fig. 4.7 (c)), we also found an increase in mobility. 20 nm nanowire had maximum mobility of 1200 cm^2/V·s - more than half of the mobility of the planar device (Fig. 4.7 (d)). This indicates that the conduction is probably happening through the restored 2DEG channels rather than through the eventual accumulated MOS channel, which would have a way lower mobility.

Recuperation of carrier concentration (N_s) with applied voltage was observed as well (Fig. 4.8 (a)).

Furthermore, we have extracted sidewall depletion widths (w_{dep}) in single- and multi-channel devices by plotting conductivity per nanowire in a tri-gate device vs nanowire width (Fig. 4.8 (b)). Single-channel value was in accordance with the previous data reported in literature [73]. The multi-channel depletion width was 2.5 times smaller than the single-channel. This date is in accordance with the fact that for single-channel tri-gates normally-off behavior can be achieved in 40-50 nm nanowires, while for multi-channels 15-20 nm width is required. By repeating the same extraction at different gate voltages (Fig. 4.8 (c)) we were able to plot w_{dep} vs gate voltage (Fig. 4.8 (c) inset).

Finally, the extracted data was correlated with threshold voltages of real devices (Fig. 4.8 (d)). The separation between normally-on and normally-off devices occurred exactly at twice the value of the w_{dep} extracted. If a lower work function metal (Ni instead of Pt) was employed, the normally-off behavior would be more difficult to achieve (Fig. 4.8 (c)).

Using all the information gathered from nanowire properties we were able to design E-mode multi-channel devices outperforming the state-of-art devices reported in the literature (Fig. 4.9). Devices with on-resistance as low as 2.8 $Ohm \cdot mm$, positive V_{TH} of +0.75 V(Fig. 4.9 (a)) and breakdown voltage as high as 1200 V (Fig. 4.9 (b)) were demonstrated. Those devices present a major advance compared to the existing ones.

4.4 Temperature-dependent carrier concentration in SC-HEMT nanowires

To further explore the electronic properties of HEMT nanowires we have performed temperature-dependent Hall measurements.

4.4.1 Measurement details

5-nanowire Hall bars with widths of 100 nm, 150 nm, and 500 nm were wire-bonded to a PCB and placed in the LakeShore CPX-VF cryoprobe station with a superconducting magnet. At each temperature, a field sweep with at least five field points between -0.35 T and 0.35 T was performed to extract the Hall coefficient from the slope of the transverse voltage vs magnetic field. At each field value, symmetry and current reversal checks were performed. The error

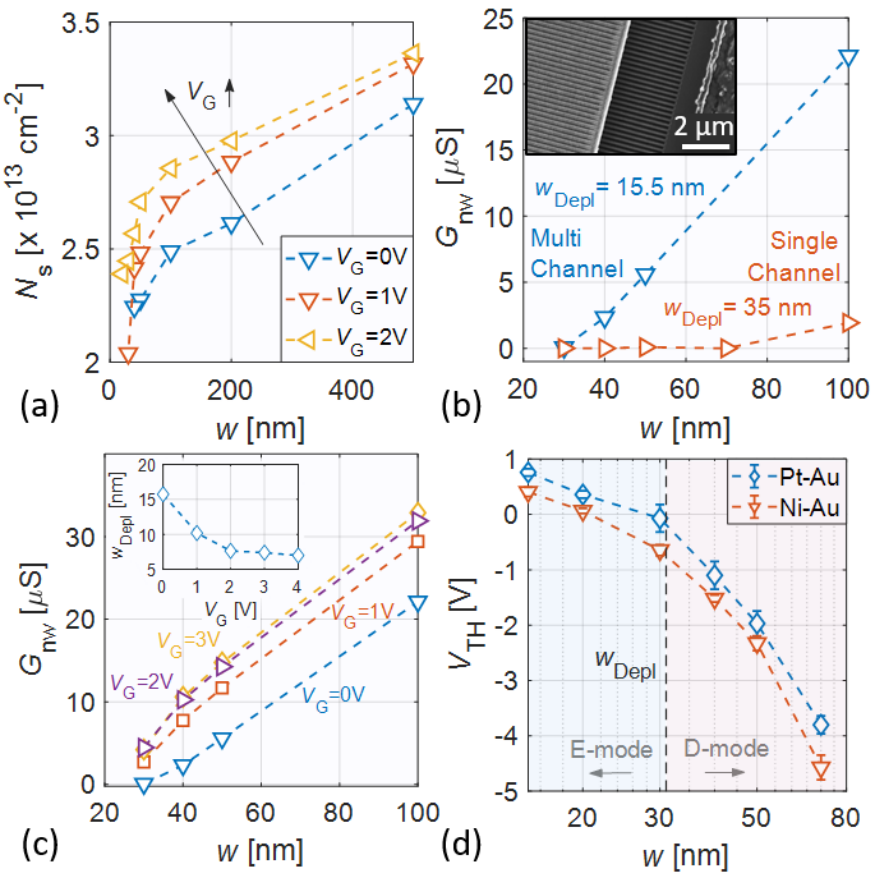

Figure 4.8 – (a) Average carrier concentration vs nanowire width for different gate voltages. (b) Conductivity per nanowire vs nanowire width extracted from a tri-gate device. One can clearly see a difference in depletion width between single- and multi-channel devices (c) Conductivity per nanowire vs width for different gate voltages and depletion width vs gate voltage (inset). (d) Threshold voltage vs nanowire width for different gate metals. The split between normally-on and normally-off devices is in perfect accordance with the measured depletion width.

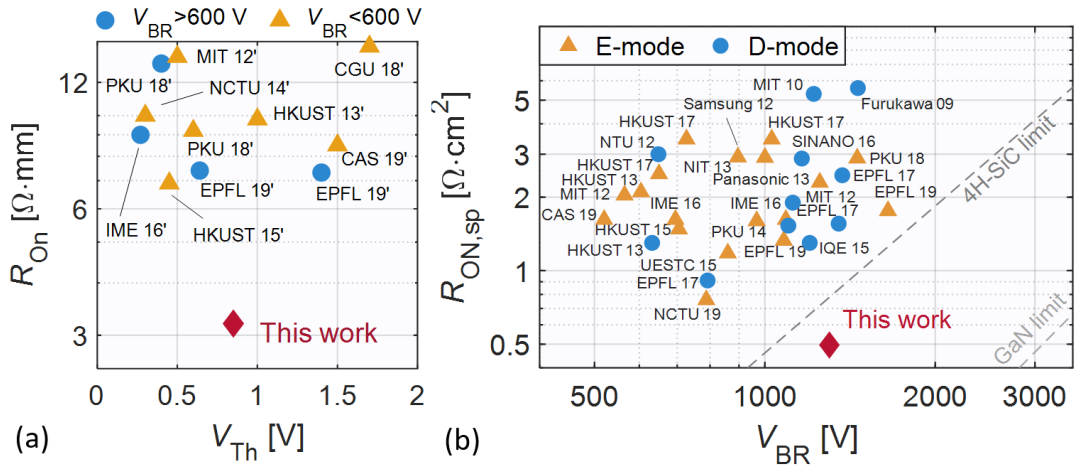

Figure 4.9 – (a) On-resistance vs threshold voltage benchmark of the device designed (b) On-resistance vs breakdown voltage benchmark of the device designed

indicated comes from the difference of values measured during the symmetry checks. Sheet resistance was extracted from longitudinal voltage. Mobility was derived from R_{sh} and N_s. The sweep was always performed from high temperature (300 K) to low (4.2 K) with preliminary degassing of the devices for at least 1h at 400K in the chamber under vacuum. The typical vacuum level at 300K was few 10^{-4} mbar. At each temperature point, the device was left for at least 15 min to settle after temperature stabilization. The temperature was stabilized within 0.1 K. Ambient light did not affect the measurement significantly, probably due to very small device area (2 um x 2.5 um for the largest 5-nanowire Hall bar measured) and the sidewalls being vertical and receiving almost no light inside the cryo chamber. However, to prevent error induced the measurement was performed in the dark. Measurements were found to be perfectly repeatable between different days. The wafer employed was a standard single-channel HEMT with 2.5 nm GaN cap, 19.8 nm $Al_{0.25}GaN$ barrier, 420 nm i-GaN channel, and 4.2 μm buffer on Si.

4.4.2 Measurement results

Sheet resistance and mobility presented a typical HEMT behavior. R_{sh} first rapidly decreased with temperature and then saturated (see Fig. 4.10 left). R_{sh} of wider nanowires was always smaller than the narrower ones. Mobility presented a typical shape in the log-log scale (see Fig. 4.10 right) with a linear phonon limited region at higher temperatures and a plateau at lower ones. The mobility of narrower nanowires was always below the mobility of wider ones. One of the connections to 100 nm nanowire broke during the last point measurement and only N_s value could be extracted with confidence.

Yet, carrier concentration presented an unexpected behavior (see Fig. 4.11). N_s in a typical HEMT with room temperature $N_s^{300\,K}$ of ~ 10^{13} cm^2 does not depend on temperature. The

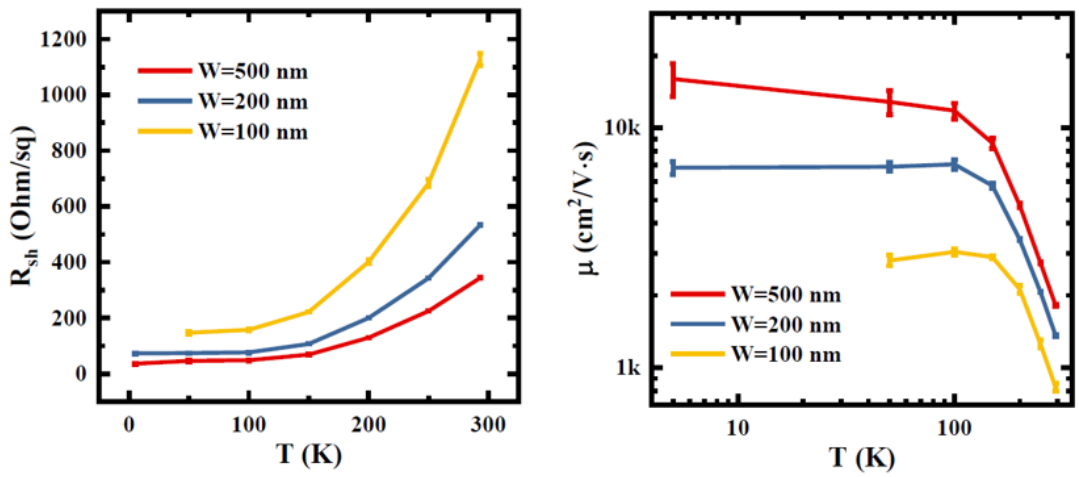

Figure 4.10 – Left: Sheet resistance vs temperature dependence for nanowires with different widths. Right: Mobility vs temperature dependence for nanowires with different widths in log-log scale

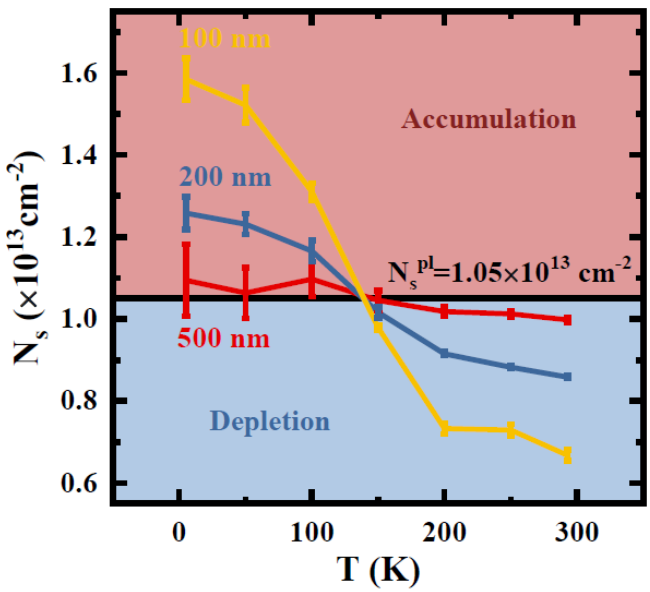

Figure 4.11 – Sheet carrier concentration vs temperature dependence for nanowires with different widths. An unexpected behavior is observed for small nanowires that pass from the depletion to flat band at T=132 K and then continue to accumulation.

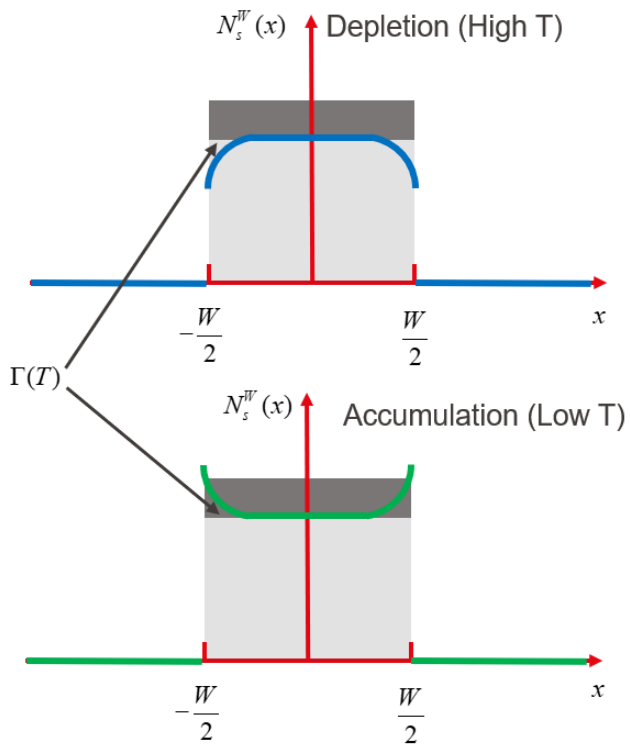

Figure 4.12 – Sheet carrier concentration profile in nanowires with definition of $\Gamma(T)$

wafer employed had $N_s^{300\,K} = 1.05 \cdot 10^{13}$ cm^2 that was verified to be unchanged for the temperatures down to 4.2 K. However, small nanowires presented a clear dependence of N_s on temperature with N_s monotonously increasing when the temperature was decreased. What was even more surprising is that N_s of narrower nanowires exceeded that of the wider ones for temperatures below 132 K. 100 nm and 150 nm behaved as if they were passing from depletion at higher temperatures to accumulation at lower ones. Further, we propose a simple semi-empirical model that could explain such behavior.

4.4.3 Model

To explain the interesting behavior of N_s observed during the temperature-dependent transport measurement we propose the following model.

Consider that at flat band the nanowire has the same N_s as the planar device. We neglect the eventual effects of the strain relaxation for the moment and discuss them separately at the end.

It is known from experiments presented here and in previous literature [74], [75], that at room temperature a sidewall depletion forms at the sidewalls of an AlGaN/GaN nanowire. One can define a quantity $\Gamma(T, W)$ that gives the number of deficient electrons with respect to

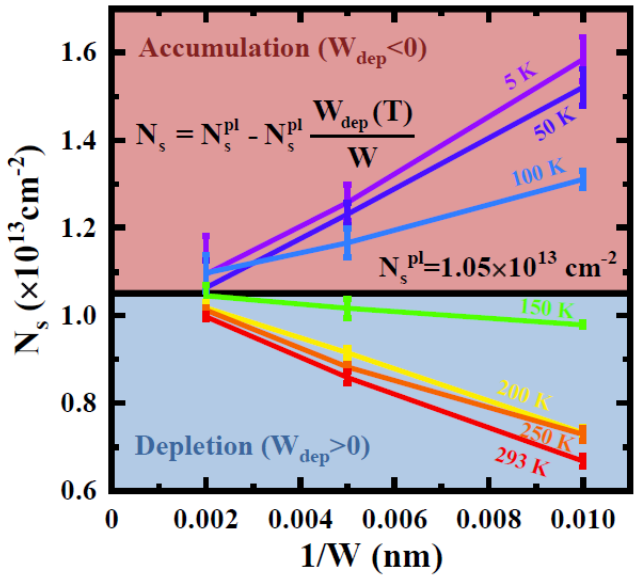

Figure 4.13 – Linear dependence of N_s on $1/W$ at different T for large enough (W»$2W_{dep}$) nanowires. The slope indicates depletion width ($W_{dep}(T)$) and the intercept yields planar carrier concentration (N_s^{pl}).

the planar case per unit length of the nanowire sidewall at a given temperature and a given nanowire width (Fig. 4.12). Similarly, one can define $\Gamma(T,W)$ for nanowire in accumulation. $\Gamma(T,W)$ is negative if nanowire is in depletion and positive if nanowire is in accumulation. Then, the average carrier concentration measured during the Hall measurement (N_s^{meas}) can be expressed as:

$$N_s^{meas} = \frac{1}{W}\int_{-W/2}^{W/2} N_s(x)dx = \frac{1}{W}\left[N_s^{planar}W + \int_{-W/2}^{W/2}\left(N_s(x) - N_s^{planar}\right)dx\right] = N_s^{planar} + \frac{2\Gamma(T,W)}{W}$$

If the nanowire is wide enough (depletion regions from both sides don't merge) then the Fermi level at the center of the nanowire will be the same for all the nanowires and $\Gamma(T,W)$ will depend only on temperature, not on width. So further we write $\Gamma(T,W) = \Gamma(T)$.

If all the assumptions above are true, N_s^{meas} should be linear vs $1/W$ at any given temperature. $\Gamma(T)$ will be given by the slope of N_s^{meas} vs $1/W$. Indeed, as we see in Fig. 4.13 N_s^{meas} does present linear behavior vs $1/W$ for any given temperature.

$\Gamma(T)$ can be easily linked to W_{dep}:

$$W_{dep}(T) = -\frac{\Gamma(T)}{N_s^{planar}}$$

Thus, from Fig. 4.13 one can easily extract the dependence of $\Gamma(T)$ (Fig. 4.15 left) and $W_{dep}(T)$

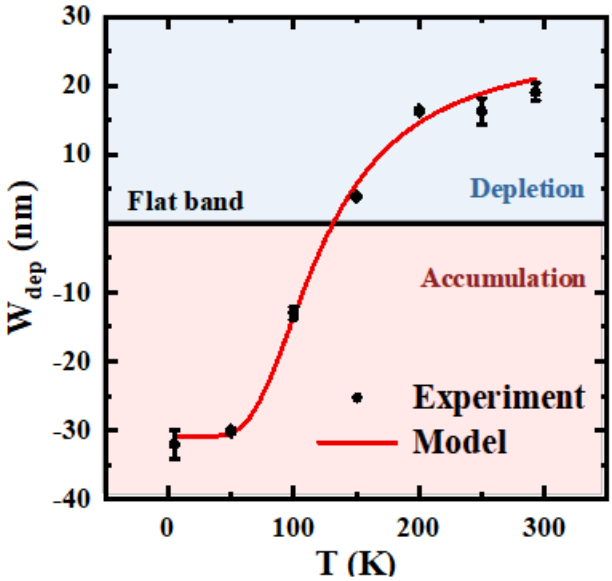

Figure 4.14 – Modelled and experimental values of W_{dep} are in a good agreement.

(Fig. 4.16) on temperature . Negative W_{dep} indicates accumulation.

To explain the temperature dependence of $\Gamma(T)$ one could imagine the following model. We suppose N_{surf}^{max} surface states per unit length of the sidewall at energy ϵ_{surf}. Each of the states can be occupied by one electron or empty. In the bulk we suppose N_{bulk}^{max} states, each having energy ϵ_{bulk} that can be occupied by one electron or empty. The system is supposed at thermal equilibrium and temperate T. Then from grand canonical ensemble formalism, one obtains the Fermi distribution of amount of occupied states on the surface and in the bulk:

$$N^{occupied} = \frac{N^{max}}{e^{\frac{\epsilon-\mu}{kT}}+1}$$

By equalizing the Fermi levels on the surface and in the bulk, the following expression is obtained:

$$\frac{N_{surf}^{occupied}}{N_{surf}^{max}} = \frac{k_1 e^{\frac{k_2}{T}}}{1+k_1 e^{\frac{k_2}{T}}},$$

where

$$k_1 = \frac{\frac{N_{bulk}^{occupied}}{N_{bulk}^{max}}}{1-\frac{N_{bulk}^{occupied}}{N_{bulk}^{max}}}$$

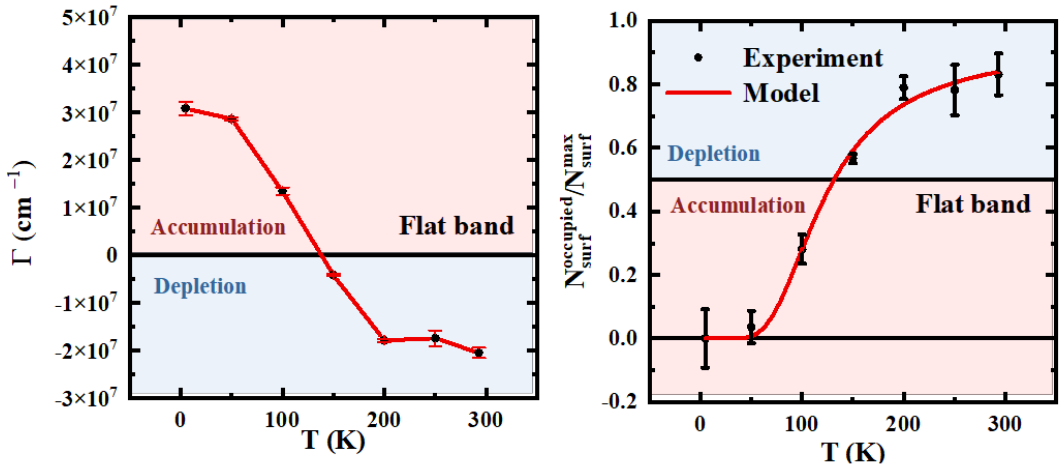

Figure 4.15 – Number of excess/deficient electrons (Γ) and surface state occupation extracted from the experiment and fitted with the model proposed. A good agreement is observed between the model and experimental data

$$k_2 = \frac{\epsilon_{bulk} - \epsilon_{surf}}{k}$$

This is a well-known curve of surface thermodynamics - Langmuir adsorption isotherm which describes thermodynamic equilibrium between surface excesses and the bulk.

It is reasonable to suppose that $\frac{N_{bulk}^{occupied}}{N_{bulk}^{max}}$ and ϵ_{bulk} are independent of T as $\frac{N_{bulk}^{occupied}}{N_{bulk}^{max}}$ is number of electrons in the planar 2DEG (independent of T as discussed before) and ϵ_{bulk} is a function of quantum well energies. In a triangular quantum-well with high-density 2DEG, the levels are separated by approximately 1 eV, thus, it is reasonable to suppose that number of occupied states doesn't change. Then Fermi energy only depends on N_s^{planar}, independent of temperature.

Now let us come back to the origin of those surface states and their occupation. When a crystal is cut, dangling bonds are created.

After GaN is cut along the m plane (our sidewall) Ga and N atoms are left on the surface with unsaturated bonds that have one electron instead of two for the atoms in the bulk in the same position. Thus, one extra state per atom of the surface is created. Those states can act as acceptors (taking the missing electron from the bulk) or as donors (giving the remaining electron to the bulk).

In a flat band condition, the surface state is like the bulk one - it has neither given nor accepted an extra electron from the bulk, thus, the occupation at the flat band is 1/2.

The maximum number of electrons the surface can lose (receive) equals the number of atoms on the surface. Per unit cell of m plane, GaN has 2 atoms which correspond to approximately

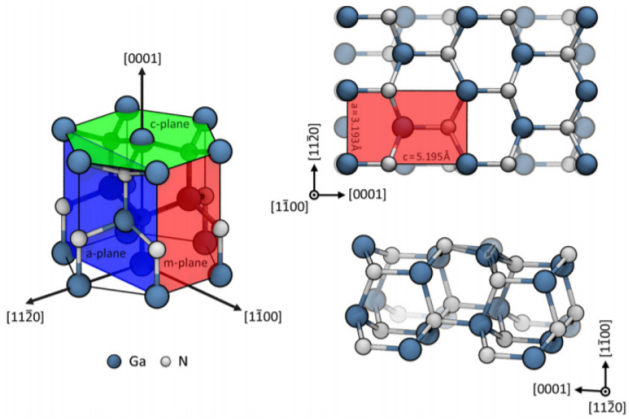

Figure 4.16 – Crystal structure and lattice parameters of GaN m-plane

$3.47 \cdot 10^7$ cm^{-1} states per unit periphery.

$$N_{surf}^{max} = \sqrt{\frac{2\ atoms}{S_{unitcell}^{m\ plane}}} = \sqrt{\frac{2}{3.193 \cdot 5.195 \cdot 10^{-16}}}\ \text{cm}^{-1} = 3.47 \cdot 10^7\ \text{cm}^{-1}$$

We can reasonably suppose that close to 0 K all the surface states have given their electrons to bulk giving rise to an excess of electrons. At higher temperatures, surface traps electrons from bulk creating a deficiency. $\Gamma(5K) = 3.09 \cdot 10^7$ cm^{-1} is in a very good agreement with this assumption and estimation of the number of surface states. And as we see from Fig. 4.15 that the curve is saturating, we would suppose:

$$\Gamma(5\ K) = 3.09 \cdot 10^7\ \text{cm}^{-1} = \Gamma(0\ K) = \Gamma^{max}$$

Now we can transpose the $\Gamma(T)$ curve into the $\frac{N_{surf}^{occupied}(T)}{N_{surf}^{max}}$ described by the Langmuir adsorption isotherm derived above and perform the fit (see Fig. 4.15). The relation between $\Gamma(T)$ and $\frac{N_{surf}^{occupied}(T)}{N_{surf}^{max}}$ is given by:

$$\frac{N_{surf}^{occupied}(T)}{N_{surf}^{max}} = \frac{-\Gamma(T) + \Gamma^{max}}{2\Gamma^{max}}$$

Fig. 4.15 shows a very good agreement between the proposed model and experimental data. The fit parameters obtained are: $k_1 = -394K$ and $k_2 = 20$.

$k_1 = -394K$ corresponds to $\epsilon_{bulk} - \epsilon_{surf} = -34$ meV. This means that the effective energy of the electron at the surface is 34 meV higher than bulk. This is in accordance with the observed

behavior: at low T all the electrons will get out from the surface to the more energetically favorable bulk, creating accumulation; at room temperature (comparable to 34 meV) electrons are excited from bulk to the surface, partially occupy it and get trapped there, creating depletion. However, the exact nature of those states and their position have to be studied separately by different methods.

$k_1 = 20$ corresponds to 95% occupation of bulk states which is not unreasonable, though the exact value for N_{bulk}^{max} is not very obvious. It is important to have less than 100% occupation of the bulk states to make the accumulation possible.

This simple model doesn't take into account the real dependence of the Fermi level in the bulk on temperature, which for a high-density 2DEG in an infinite triangular well should be way weaker than the one supposed here. However, from simulations one can see that the Fermi level in the quantum well of a typical high-density 2DEG is very shallow, making the real situation very different from the infinite triangular well hypothesis and pure 2D statistics for electrons. However, this point has to be investigated more thoroughly and in detail.

To summarize, we have performed a temperature-dependent Hall measurement to extract the dependence of N_s in nanowires on temperature. We observed an unexpected behavior of nanowire passing from depletion at room temperature to flat band around T=132 K and into accumulation when the temperature decreases further. We proposed a semi-empirical model that explains well the behavior observed. Model parameters extracted are the difference between surface and bulk energies of 34 meV and occupation of bulk states of 95%. The values extracted are not unreasonable, however, an independent in-depth study is required to determine the exact microscopic origin of those parameters and explain their values.

4.4.4 Model verification: passivated Hall bar

To further confirm the link between the depletion/accumulation behavior observed and surface states we performed an extra measurement of a 100 nm Hall bar with the surface conformally passivated by SiN [21] (see Fig. 4.17). The observed variation of N_s vs T was significantly reduced in a passivated bar compared to its unpassivated counterpart (see Fig. 4.17). This is in accordance with the fact that passivation should reduce the number of surface states and, thus, restrict the number of electrons that can be lost/accumulated by the bulk. A further study with the precise extraction of the number of surface states in passivated devices could be of interest for future work. Moreover, it could become a powerful tool for the characterization of different sidewall passivation strategies.

4.4.5 Comments about strain effects

In the very beginning, we supposed that N_s^{bulk} is the same for all nanowire widths. By supposing this, any eventual strain relaxation effect is neglected. However, this assumption is not unreasonable.

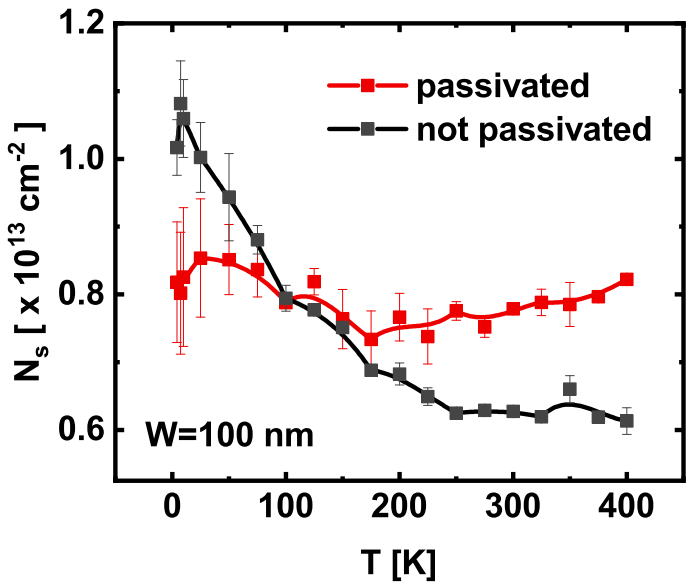

Figure 4.17 – N_s vs T for passivated and unpassivated 100 nm wide nanowire. The passivated device presents way less accumulation/depletion, indicating the surface origin of the observed phenomena in accordance ith the model proposed

First of all, in AlGaN piezo-electric charges represent not more than 30-40% of the total charge. Thus, even in a fully relaxed nanowire N_s would be reduced not more than by 30%.

Moreover, nanowires considered here are relatively large (W>100 nm). Thus, strain relaxation, which might be essential for smaller nanowires does not necessarily play a significant role here. According to our COMSOL simulations, strain should enter into the game for nanowires below 50 nm. As the model taking into account only surface effects already explains rather well the experimental data, it is reasonable to neglect the strain-related effects.

Another concern is the temperature dependence of strain, which could be at the origin of the observed effects rather than surface-related effects. However, if one compares the thermal expansion coefficients (taken from [76]) even between GaN and AlN and translates them in a possible variation of strain with temperature, only a 3% variation of piezoelectric polarization should be observed - nothing compared to more than x2 increase of N_s in a 100 nm nanowire. Spontaneous polarization does not depend on temperature neither [77].

The real concern should rather be that some residual gases/ water vapors are adsorbed on the nanowire sidewall in the chamber. To minimize such effects, we tried to go to the lowest possible vacuum level ($< 10^{-4}$ mbar at low T) and performed at least 1-hour degassing of the sample at 400 K (the highest temperature available in our chamber) prior to the measurement. However, this possibility can not be neglected and should be studied more in detail.

4.5 Future work

The work presented opens a lot of questions as to the role of sidewall surface states in the nanowire-based SC- and MC-HEMTs. Although some interesting preliminary results are presented, a detailed exploration of the origin of those states as well as the behavior of the bulk is necessary. Moreover, a thorough study of passivated devices with the extraction of surface state density would be beneficial and could potentially lead to a new technique to characterize surface sidewall states. Increasing the number of device widths under consideration could also be interesting to improve the quality of the data presented and to reduce errors.

Finally, a study of the potential influence of external factors (residues in the vacuum chamber) is a necessary check to ensure the consistency of the model.

4.6 Conclusion

In this chapter, we presented a study of the electronic properties of single- and multi-channel nanowires. Most of the measurements presented are reported for the first time, to the best of our knowledge. We proposed a semi-empirical model to explain the temperature behavior of single-channel HEMT nanowires, that explains well the measured experimental data.

The reported properties of multi-channel nanowires allowed us to design MC-HEMTs that outperform state-of-the-art devices. And the proposed model opens new perspectives for the analysis of sidewall surface states in tri-gate devices.

5 In-plane gate multi-channel transistors

Multiple 2DEG channels in an MC-HEMT can not be controlled by conventional top gates, thus, alternative gating techniques have to be investigated. While for power transistors the tri-gate configuration satisfies all the needs, for RF domain one might want to have a lower gate capacitance to achieve higher frequencies. In-plane gate transistors (IPGs) [74], [78]–[84] present an interesting geometry that offers an advantage in terms of lower intrinsic gate capacitance compared to planar, double- and tri-gates, and were proposed for high-frequency applications [74], [78]–[81]. A single-channel GaN HEMT IPG for RF applications was analyzed in detail in [74]. Namely, the estimated cut-off frequency, including both intrinsic and extrinsic components, was predicted to be in THz range (up to 0.89 THz) and the influence of channel width and gate-to-channel spacing was studied in detail. The advantages of IPGs for RF applications described previously [74], [78]–[81] could only be directly verified experimentally once a real scaled-up device is fabricated. One of the ways to get closer to it is to maximize the performance of a single device, which was the aim of the study presented further. Moreover, even if RF potential of IPGs can be disputed, other potentially interesting applications remain: sensing, enabled by a larger surface, or high-temperature/harsh environment operation possible due to the absence of Schottky metal. Both of those would benefit from an increased transconductance and conductance of a single device, offered by multi-channel IPGs presented in this chapter. Finally, the possibility of almost simultaneous control of multiple channels by the in-plane gate as well as the study of the field-effect (or not) origin of this control constitute an interesting topic to explore.

All the quantities (current, transconductance) of IPGs presented were normalized in the same way as in previous works in the literature, so that the reader could easily compare the presented device to others and benefit from the analysis of capacitance (and thus cut-off frequency) performed by previous authors [74], [78]–[81]. One should notice that a fair way to normalize would be to divide by the total width of the scaled-up device on the wafer, which would include gate size and gate-to-channel spacing but on the other hand would depend on precise scaled-up technology. Contrary to classical FinFETs, it is not reasonable to include sidewall height in the normalization. First of all, IPGFET is still a HEMT device and conduction occurs

only through 2DEGs, not through the whole height. Moreover, those devices are normally-on and no accumulation layer is present. Thus, as for any HEMT the relevant normalization width is linked to the surface occupied by the device on the wafer face which is proportional to nanowire width plus gap width plus gate size.

In this chapter, we propose and investigate numerically and experimentally multi-channel in-plane-gate field-effect transistors. We show the advantages of using a multi-channel structure over its single-channel counterpart. The proposed device led to a 3-time increase in maximum current density and peak normalized transconductance as compared to the best previously reported IPGFETs. Moreover, we numerically and experimentally explore the origin of the gate control in single- and multi-channel IPGs.

This chapter is based on the paper "Multi-channel AlGaN/GaN in-plane-gate field-effect transistors" by Catherine ERINE, Jun Ma, Giovanni Santoruvo, and Elison Matioli published in IEEE Electron Device Letters [16]. Catherine Erine has fabricated devices, performed numerical and experimental characterization and has written the paper. Catherine Erine and Giovanni Santurovo have elaborated the device design. Jun Ma has grown the heterostructures.

All the subsections with reference in the title are entirely taken from the corresponding paper.

5.1 Motivation [16]

Multi-channel high-electron mobility heterostructures with low sheet resistance offer a promising platform for decreasing the on-resistance of high electron mobility transistors (HEMTs) without increasing the device footprint[18], [19], [24], [25]. However, efficient electrostatic control of multiple channels by conventional top-gate structures is quite challenging and usually comes at the expense of low transconductance values due to a large negative V_{th} required to turn off all the channels by the top gate [19]. Thus, alternative gate geometries able to control and take advantage of the high conductivity of multiple two-dimensional electron gases are of interest. In addition to the tri-gate [12], [85] (castellated FET [24], [25]) and double-gate (BRIDGEFET [86], [87]) structures reported in the literature, we present a device that combines highly conductive multi-channel structure with in-plane gate geometry employing a pure lateral control of the channel: multi-channel in-plane-gate field effect transistor.

In an in-plane-gate field-effect transistor (IPGFET) [74], [78]–[84], the 2DEG channels in a nanowire are actuated by means of an electric field applied on the sidewalls of the nanowire by lateral in-plane 2DEG gates (Fig. 5.1). All the metallic contacts are ohmic. In-plane-geometry offers an advantage in terms of lower intrinsic gate capacitance compared to planar, double- and tri-gates, and is proposed for high-frequency applications[74], [78]–[81].

Single-channel IPGFETs based on III-V and III-N semiconductors reported in the literature demonstrated efficient control of the channel by side gates, along with high normalized transconductances (g_m) and current densities (I_d) [74]. For practical applications, the limited

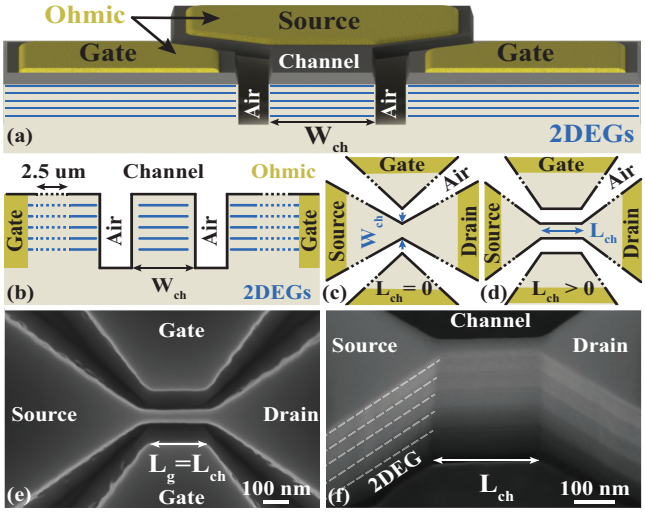

Figure 5.1 – (a) 3-dimensional schematic and (b) cut perpendicular to the channel of the multi-channel IPGFET; (c) top-view schematic of a 0 nm -long IPGFET and (d) top-view schematic of an IPGFET with non-zero channel length; (e) top-view and (f) 30°-tilted SEM image of a 250 nm-long and 60 nm-wide multi-channel IPGFET showing five stacked 2DEGs.

absolute current and transconductance in a single nanowire require a large number of parallel devices connected by air-bridges [88], which may lead to high parasitics. One of the ways to address this issue is by vertically stacking multiple 2DEGs within the same device channel which increases I_d and g_m of an individual device and thus reduces the amount of parasitics due to the interconnections.

In this work, we present a multi-channel in-plane-gate field effect transistor to efficiently and simultaneously control multiple parallel 2DEG channels. Optimized devices demonstrated a 3-time increase in on-current density with almost no shift in threshold voltage compared to the best reported single-channel IPGFET [74], leading to 3.7x-gain in normalized peak transconductance. In addition, we numerically analyze the precise mechanism of the gate

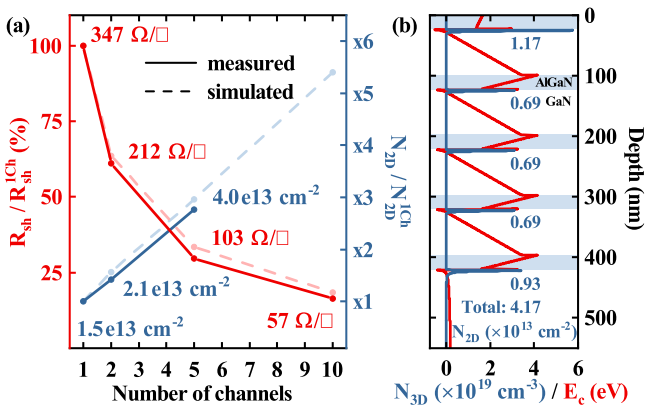

Figure 5.2 – (a) Measured (solid) and simulated (dashed) carrier concentrations and sheet resistances in different multi-channel structures. (b) Simulated band structure and carrier concentration (N_{3D}) of the five-channel wafer chosen for device fabrication. Sheet carrier concentration in each channel (N_{2D}) obtained by integrating N_{3D} in the quantum well is indicated.

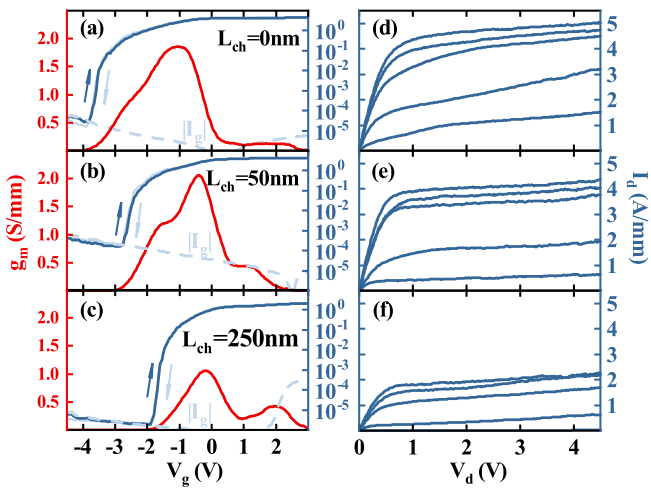

Figure 5.3 – Logarithmic scale double sweep transfer and transconductance at V_d = 5 V ((a) - (c)) and output characteristic at V_g = - 2 V: 1 V: 2 V ((d) - (f)) of devices with L_{ch} of 0 nm, 50 nm and 250 nm normalized to the nanowire width (63 nm, 35 nm and 67 nm correspondingly). Short (0 nm, 50 nm) channel devices show saturation current densities above 4 A/mm along with tranconductances above 2 S/mm.

control in IPGFETs and identify the lateral electric field as the main source of the channel control in MC-IPGFETs.

5.2 Heterostructure design and device fabrication [16]

A series of multi-channel wafers with 1, 2, 5, and 10 periods of 23 nm $Al_{0.3}Ga_{0.7}N$ /1 nm AlN/ 75 nm i-GaN were grown over templates of 1.6 um i-GaN/ 300 nm AlN on 2-inch sapphire substrates. The sheet resistance (R_{sh}) was reduced from 347 Ω/sq for the one-channel structure to 57 Ω/sq for the ten-channel one, while preserving mobilities over 1400 cm^2/V×s for multi-channel structures.

Sheet carrier concentrations scaled linearly with the number of channels (Fig. 5.2 (a)). Numerical simulations performed using material parameters from [76] and surface Fermi level from [34] revealed 3 types of channels present in each structure: top channel (influenced by the top surface, N_{2D}=1.17×10^{13} cm^{-2}), bottom channel (influenced by the buffer, N_{2D}=0.93×10^{13} cm^{-2}) and middle channels that always had the same N_{2D}=0.69×10^{13} cm^{-2} in each structure as no intentional doping is present (Fig. 5.2 (b)). The linear dependence of N_{2D} on the number of channels can be given by $N_{2D}(N)=[1.17+0.93+0.69\times(N-2)]\times10^{13}$ cm^{-2} from the simulated data, which is within 5% agreement with the experimental values (Fig. 5.2 (a)).

The five-channel wafer offered a good compromise between the total depth of the structure (500 nm) and low sheet resistance (103 Ω/sq) and has been chosen for device fabrication. Total N_{2D} of 4.03 × 10^{13} cm^{-2} along with mobility of 1650 cm^2/V×s were extracted from Hall measurements.

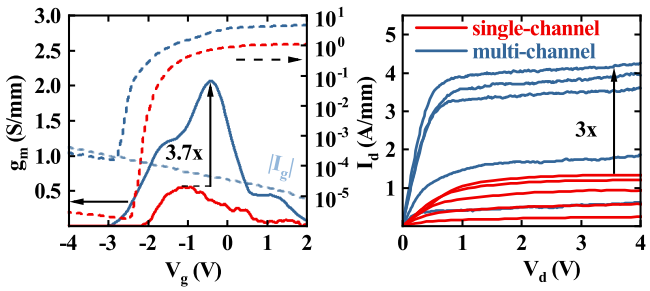

Figure 5.4 – Comparison between transfer (a) and output (b) characteristics of single- and multi-channel devices with L_{ch}=50 nm and W_{ch} of 40 nm and 35 nm correspondingly. Multi-channel device offers a 3.7-time gain in tranconductace and 3-time gain in saturation current density.

The IPGFET fabrication consists of only 2 major steps, resulting in an inherently self-aligned structure. First, nanowire channel and gates are defined by electron beam lithography using 6% hydrogen silsesquioxane (HSQ) resist followed by Cl_2-based inductively coupled plasma (ICP) etching to isolate the gate mesas from the channel. The second step consists of deposition of ohmic contacts for source, drain, and gate electrodes by one optical lithography followed by metal deposition, lift-off, and annealing. A metal stack consisting of Ti (200Å) /Al (1200Å) /Ti (400Å) /Ni (600Å) /Au (500Å) is deposited by electron-beam evaporation and annealed at 860°C resulting in contact resistance of 0.6 Ω·mm extracted by transmission line method (TLM).

5.3 Experimental Results [16]

A series of devices with nanowire lengths (L_{ch}) of 0 nm, 50 nm, 250 nm were fabricated. The gate length is always equal to the channel length, as the access regions are much wider than the channel. All the devices show excellent simultaneous control of all five channels with only one major transconductance peak (Fig. 5.3 (a) - (c)). Minor transconductance shoulders probably come from three different types of channels present in the structure (see section IV). A separate peak in the 250 nm-long device at 2 V could come from one of the channels or might be caused by gate leakage that increases close to this point. The On/Off ratios for these devices were 10^5, 10^4, 10^6 respectively, and off-current was equal to the gate leakage, indicating good gate control at all lengths (Fig. 5.3 (a) - (c)). Even though no passivation or surface treatment was used, the hysteresis in all the devices was very small (< 0.1 V, Fig. 5.3 (a) - (c)). The maximum drain current was reduced as wire length was increased, from 5.07 A/mm for a 0 nm-long channel to 2.27 A/mm for a 250 nm-long one (Fig. 5.3 (d) - (f)) as expected in a usual HEMT. The 50 nm-long device offers a good compromise between high current density and transconductance and serves for comparison with the reference single-channel IPGFET with the same dimensions from [74]. Multi-channel device delivered a 3-time increase in on-current (Fig. 5.4 4(b)) without major (less than 1V) shift in threshold voltage (Fig. 5.4 (a)) as compared to the equivalent single-channel device. This increase corresponds to the 3.4x smaller sheet resistance observed in the multi-channel wafer with respect to the

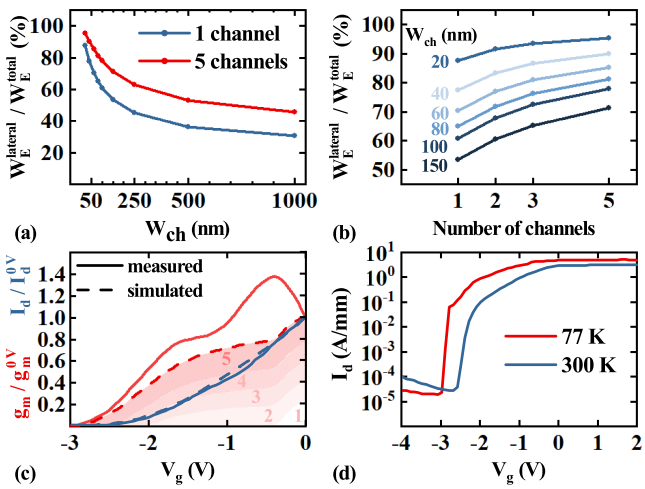

Figure 5.5 – (a) Fraction of the total electrostatic energy used for lateral control as a function of channel width for single- and multi-channel IPGFETs with gate to channel separation of 60 nm. (b) Fraction of the total electrostatic energy used for lateral control as a function of number of channels for different W_{ch} and gate-to-channel separation of 60 nm. (c) Simulated and measured transfer characteristics and transconductance of 50 nm-long and 40 nm-wide IPGFET normalised to the values at $V_g = 0$ V. The split of the total simulated transconductance in separate channels (1 - the bottom-most) is shown. (d) Transfer characteristic of a MC-IPGFET at room temperature and 77 K.

single-channel one. A 3.7x increase in transconductance with respect to the equivalent single channel device (Fig. 5.4 (a)) indicates no loss in gate control efficiency. As compared to the best device reported in the literature [74] (20 nm wide, 50 nm long, shallow etched), a 3-time gain in transconductance is observed.

The maximum absolute current of 320 μA and transconductance of 120 μS were achieved for a 0 nm-long 63 nm-wide device, which is 3.2- and 4- times higher than in the best single-channel IPGFET [74], which reduces by 4 the number of devices needed for a given output current.

5.4 Simulation Results [16]

The possible mechanisms behind the control of IPGFETs include: the in-plane field from gate 2DEGs [79]–[81], surface trap assisted control[89] and back-gating through the traps from the bottom[90]. The former is a quick mechanism giving rise to a low capacitance of in-plane gates[78], while the others may lead to undesirable slow charging/discharging of buffer traps in poorly designed devices[91] and even to the total loss of control at low temperatures[89].

In a multi-channel IPGFET, bottom control should be less pronounced as the bottom-most channel screens the upper ones from a potential back gate. Moreover, vertical depletion of multiple channels is impossible with voltages below several tens of volts according to experimental data from [19]. To confirm this hypothesis, we performed a numerical estimation of the fraction of electrostatic energy stored in the lateral part of device (mainly between gate

and channel) $W_E^{lateral}$ to the total electrostatic energy (including the portion stored in the buffer and used for backgating) W_E^{total}. The ratio of the two above-mentioned energies is equal to the ratio of lateral-to-total capacitance coupling the gate and the channel and quantifies the part of the control due to lateral field. As expected, the part of lateral control decreases with the channel width (for a fixed gate-to-channel distance of 60 nm in this case). However, as shown in Fig. 5.5 (a), over 80% of electrostatic energy is used for lateral control in five-channel IPGFETs with W_{ch} ≤80 nm. For single-channel devices, only the 20 nm-wide device has the same ratio. For a given channel width, increasing the number of channels leads to an increase of the lateral control (Fig. 5.5 (b)). These results suggest that MC-IPGFETs are less prone to backgating from the buffer.

Furthermore, to prove that the pure lateral field-effect control can fully explain the performance of multi-channel IPGFETs, we have performed a 3D TCAD simulation using Silvaco ATLAS with the gate completely insulated from the channel by an ideal dielectric (no leakage allowed) eliminating the possibility of back gating. Previously used heterostructure parameters were unchanged except for the piezoelectric polarization that was adjusted to accommodate the strain relaxation occurring in small AlGaN/GaN nanowires[75], [92]. The average N_{2D} in the nanowire channel was monitored as a function of gate voltage (V_g) and normalized to the value at V_g = 0 V in order to compare with experimental data. Full depletion of the nanowire gives a linear scale V_{th}=-2.85 V, very close to the one observed in the experiment (Fig. 5.5 (c)). Moreover, we also simulated the variation versus V_g of the carrier density and transconductance due to each channel separately. When decreasing V_g the channels turn-off from top to bottom. The first one is the top-most (1st, V_{th}=-0.35 V), then comes the 2nd (V_{th}=-2.05 V), then very soon and simultaneously the 3d and the 4th (V_{th} = -2.3 V) , and, finally, the 5th (the bottom-most, V_{th}=-2.85 V, equal to the V_{th} of the device). The carrier distribution among channels at zero gate voltage was different due to the presence of the sidewalls that influence strongly carrier concentrations in such a small nanowire, but still, 3 groups of channels were present: top, bottom and three very similar middle ones.

To exclude the surface trap assisted mechanism, we have measured the transfer characteristic of an MC-IPGFET at 77 K (Fig. 5.5 (d)). As opposed to [89] no loss of control was observed, only a slight shift of threshold voltage and a steeper subthreshold slope. A good agreement between the experiment and simulation data allows us to conclude that the behavior of the multi-channel IPGFET can be explained by the lateral field-effect control of the channel.

5.5 Future Work

The main direction for future work is the experimental demonstration of a scaled-up device for direct high-frequency characterization.

Furthermore, as IPGs employ no Schottky metal, it could be interesting to characterize their high-temperature behavior. Indeed, when exposed to very high temperature, GaN transistors usually face problems mostly due to the decomposition and diffusion of the gate metal

(bubbling, leakage). Ohmic contacts are way more resistant to temperature and environments.

In addition, one could use regrown n++-GaN gates instead of metallic ones, obtaining a fully metal-free transistor. Regrown bridges could also solve the problem of scaling-up.

Moreover, the open nanowire sidewalls could be used as sensors. As the main resistance drop in an IPG occurs at the nanowire, even a small variation of the sidewall depletion due to the change of the occupation of the sidewall states could lead to significant conductance variations.

5.6 Conclusion [16]

In this work, we demonstrated multi-channel single nanowire IPGFETs. The multi-channel heterostructure provided increased carrier density while preserving high mobility, leading to current densities as high as 4.35 A/mm. The efficient control of the multiple-2DEG-channel by the in-plane gate resulted in 2.05 S/mm peak transconductance. The proposed device led to a 3-time increase in maximum current density and peak normalized transconductance as compared to the best previously reported IPGFETs. Numerical simulations and low-temperature characterization suggest that the observed behavior comes from the side field-effect control with no trap-related effects involved. Multi-channel IPGFETs offer an alternative way to control multiple highly conductive 2DEG channels and open a promising opportunity for new devices with increased current density and reduced intrinsic gate capacitance.

6 Conclusion

In this thesis, an extensive study of multi-channel and single-channel high-electron mobility heterostructures was performed. An analytical model for carrier concentrations in each of its multiple 2DEG channels is derived. General rules for the multi-channel stack design for a given application are presented.

Field management techniques based on the super-junction effect are explored and a novel devices concept - intrinsic polarization super junction transistor is proposed and described analytically and numerically. Those devices decouple off-state performance from the on-state conductivity, resolving the fundamental trade-off between the on-resistance and breakdown voltage and potentially breaking GaN 1D material limit.

Electronic transport in single- and multi-channel HEMT nanowires is explored. Performances of the devices employing those nanowires are presented. A model explaining temperature-dependent behavior of carrier concentration in single-channel HEMT nanowires is elaborated. The proposed model could be a useful tool for investigating sidewall surface states behavior in nanowire transistors.

Finally, an alternative gating technique for MC-HEM heterostructure - in-plane-gate - is proposed and verified experimentally. Multi-channel in-plane-gate field-effect transistors offer reduced gate capacitance, potentially interesting for RF applications.

Results of this thesis contribute to the understanding and optimization of MC-HEMT transistors for power electronics applications.

A Calculations and details of the model derivation [36]

A.1 Model for Undoped structures

A.1.1 General case and middle channels

Gauss law (Displacement continuity):

$$\begin{aligned} &-\epsilon_{ch}E_{ch}^{(i-1)} + \epsilon_b E_b^{(i)} = q(p^{(i)} - \Delta\sigma) \\ &-\epsilon_b E_b^{(i)} + \epsilon_{ch}E_{ch}^{(i)} = q(\Delta\sigma - n^{(i)}) \\ &i = \overline{1,N} \quad E_{ch}^{(0)} = E_{cap} \quad E_{ch}^{(N)} = E_{buff} \end{aligned} \tag{A.1}$$

where $\Delta\sigma = \sigma_b - \sigma_{ch}$, σ_b, σ_{ch} - total (spontaneous + piezo) polarization charge densities in barrier/channel correspondingly, q - absolute value of electron charge, $E_{b/ch}^{(i)}$ electric fields in barrier/channel in i^{th} period from the top, considered positive if pointing from cap to barrier, $\epsilon_{ch/b}$ absolute permittivities of corresponding layers. Cap and buffer are considered to be made from the same material as the channel.

From this, one can get expressions for $n^{(i)}$ and $p^{(i)}$

$$\begin{aligned} p^{(i)} &= \Delta\sigma - \frac{\epsilon_{ch}E_{ch}^{(i-1)} - \epsilon_b E_b^{(i)}}{q} \quad i = \overline{1,N} \\ n^{(i)} &= \Delta\sigma - \frac{\epsilon_{ch}E_{ch}^{(i)} - \epsilon_b E_b^{(i)}}{q} \quad i = \overline{1,N} \end{aligned} \tag{A.2}$$

Express $E_{ch/b}^{(i)}$ using the continuity of the Fermi level (remembering that energy drop is $-q\Delta V$):

$$\begin{aligned} -qd_b E_b^{(i)} &= E_g^{ch} + \Delta E_{f,v}^{(i)} + \Delta E_{f,c}^{(i)} \quad i = \overline{1,N} \\ qd_{ch}E_{ch}^{(i)} &= E_g^{ch} + \Delta E_{f,c}^{(i)} + \Delta E_{f,v}^{(i+1)} \quad i = \overline{1,N-1} \end{aligned} \tag{A.3}$$

leading to the following expressions:

$$
\begin{aligned}
p^{(i)} &= \Delta\sigma - \frac{1}{q^2}\left[\frac{\epsilon_{ch}}{d_{ch}}\left(E_g^{ch} + \Delta_{c,i-1}^{v,i}\right) + \frac{\epsilon_b}{d_b}\left(E_g^{ch} + \Delta_{c,i}^{v,i}\right)\right] \\
&\qquad\qquad\qquad\qquad\qquad\qquad i = \overline{2,N} \\
n^{(i)} &= \Delta\sigma - \frac{1}{q^2}\left[\frac{\epsilon_{ch}}{d_{ch}}\left(E_g^{ch} + \Delta_{c,i}^{v,i+1}\right) + \frac{\epsilon_b}{d_b}\left(E_g^{ch} + \Delta_{c,i}^{v,i}\right)\right] \\
&\qquad\qquad\qquad\qquad\qquad\qquad i = \overline{1,N-1} \\
\Delta_{c,l}^{v,k} &= \Delta E_{f,v}^{(k)} + \Delta E_{f,c}^{(l)}
\end{aligned}
\tag{A.4}
$$

$\Delta E_{f,v}^{(k)}$ and $\Delta E_{f,c}^{(l)}$ are defined generally (they can be positive or negative). Those quantities are positive if 2DEG/2DHG is present at the corresponding interface and negative if not. One can notice that if 2DEG/2DHG is present at the interface those quantities will be much smaller than bandgap (200-500 meV for $\Delta E_{f,c}^{(k)}$ and <20-50 meV for $\Delta E_{f,v}^{(l)}$) and in the first approximation can be neglected. If better precision is needed one can assume all $\Delta_{v,l}^{c,k}$ equal and choose $\Delta_{v,l}^{c,k} = \Delta_{avg}^{sim}$ - averaged over all geometries under consideration sum of conduction and valence band penetrations through the Fermi level for middle channels:

$$
\Delta_{avg}^{sim} = \frac{1}{d_{ch}^{max} - d_{ch}^{min}} \int_{d_{ch}^{min}}^{d_{ch}^{max}} \frac{1}{d_b^{max} - d_b^{min}} \int_{d_b^{min}}^{d_b^{max}} \Delta_{c,mid}^{v,mid} \, dd_b dd_{ch} \tag{A.5}
$$

The latter approach gives almost an ideal match between simulation and model.

However, if 2DEG/2DHG is absent from corresponding interface $\Delta E_{f,c}^{(i)}$ / $\Delta E_{f,v}^{(i)}$ can not be neglected anymore or replaced by a constant and should be expressed from the condition $n^{(i)} = 0$ / $p^{(i)} = 0$.

Those formulas give the solution for all the channels except the last and the first that should be treated separately.

One should notice that the assumption of $n^{(i)}$ and $p^{(i)}$ being sheet charges leads to the fact that $\Delta E_{f,c/v}^{(i)}$ is not the difference between bottom of conduction band and Fermi level but rather between the energy axis intercept of linear conduction band profile and bottom of the conduction/valence band at the corresponding interface. However, the effective thickness of 2DEG being way smaller (~1 nm) than channel thickness (>10 nm) this assumption does not introduce a significant error.

A.1.2 Superlattice

For a superlattice $p^{(i)} = n^{(j)}\ \forall i, j$ (if not the field will grow infinitely) and all $\Delta E_{f,c}^{(k)}$ and $\Delta E_{f,v}^{(l)}$ are equal leading to $\Delta_{v,l}^{c,k} = \Delta\ \forall k, l$. This yields a particularly simple solution:

$$p = -n = \Delta\sigma - \frac{E_g^{ch} + \Delta}{q^2}\left[\frac{\epsilon_{ch}}{d_{ch}} + \frac{\epsilon_b}{d_b}\right] \tag{A.6}$$

Notice also that solving $n = 0$ yields a criterion for the 2DEG/2DHG to appear in the superlattice. It turns out that middle channels in a finite multi-channel structure can be treated as superlattice in most cases.

A.1.3 The bottom most channel

Let's write the expression for $n^{(N)}$ combining (A.1), (A.2) and (A.3)

$$n^{(N)} = \Delta\sigma - \frac{\epsilon_{ch}E_{buff} + \frac{\epsilon_b}{d_b}\left[E_g^{ch} + \Delta_{c,N}^{v,N}\right]}{q^2} \tag{A.7}$$

Whatever is d_{buff} the total drop through the buffer - $E_{buff}d_{buff}$ - is finite which is possible only if E_{buff} is at least $O(\frac{1}{d_{buff}})$. So E_{buff} can be neglected as usually buffer is large enough.

$$n^{(N)} = \Delta\sigma - \frac{E_g^{ch} + \Delta_{c,N}^{v,N}}{q^2}\frac{\epsilon_b}{d_b} \tag{A.8}$$

Again, when 2DEG is present $\Delta_{c,N}^{v,N}$ can be either neglected or replaced by a constant (as shown in the main text). This constant turns out to be the same as for middle channels. $n^{(N)}$ is independent from channel thickness and depends linearly on $\frac{1}{d_b}$.

One can notice that this solution is exactly the same as for an uncapped single-channel structure[46] with $d_{cap} = 0$ and $E_g^{ch} + \Delta E_{f,v}^{(N)}$ taken as Schottky barrier height.

A.1.4 The top most channel

Let's write the expression for $p^{(1)}$ combining (A.1), (A.2) and (A.3)

$$p^{(1)} = \Delta\sigma - \frac{\epsilon_{ch}E_{cap} - \frac{\epsilon_b}{d_b}\left(E_g^{ch} + \Delta_{c,1}^{v,1}\right)}{q^2} \tag{A.9}$$

One can get an expression for E_{cap} from continuity of Fermi level in the cap:

$$q\Phi_b + d_{cap}E_{cap} - E_g^{ch} - \Delta E_{f,v}^{(1)} = 0 \tag{A.10}$$

leading to

$$p^{(1)} = \Delta\sigma - \frac{E_g^{ch} + \Delta_{c,1}^{v,1}}{q^2}\left[\frac{\epsilon_{ch}}{d_{cap}} + \frac{\epsilon_b}{d_b}\right] + \frac{q\Phi_b + \Delta E_{f,c}^{(1)}}{q^2}\frac{\epsilon_b}{d_{cap}} \tag{A.11}$$

Depending on the cap thickness and Schottky barrier height $p^{(1)}$ may be zero or not. If it is non zero one can use the same argument as before to neglect $\Delta_{v,l}^{c,k}$ or replace it with a constant. Then the problem is solved and one has all the carrier densities. However, if $p^{(1)} = 0$ one can not neglect $\Delta E_{f,v}^{(1)}$ (as it becomes negative and large). In that case, let's express $\Delta E_{f,v}^{(1)}$ from the condition $p^{(1)} = 0$ and plug it into the expression (A.15) for $n^{(1)}$. After a careful calculation one gets:

$$\begin{aligned} n^{(1)} = & \frac{\Delta\sigma - \frac{1}{q^2}\frac{\epsilon_b}{d_b}\left(q\Phi_b + \Delta E_{f,c}^{(1)}\right)}{1 + \frac{\epsilon_b}{\epsilon_{cap}}\frac{d_{cap}}{d_b}} - \\ & - \frac{E_g^{ch} + \Delta_{v,2}^{c,1}}{q^2}\frac{\epsilon_{ch}}{d_{ch}} \end{aligned} \tag{A.12}$$

The first term matches exactly the single channel with cap solution from [46] and the second accounts for the finite channel thickness (and thus non-zero "buffer" field). Considering $N = 1$ and $d_{ch} \to \infty$ (or $E_{ch} = 0$) leads to the single-channel solution[46].

A criterion for having non-zero $p^{(1)}$ (and the cap thickness delimiting the two cases) can also be provided. Assuming that at the moment when $p^{(1)}$ just starts to appear $\Delta E_{f,v}^{(1)} = 0$, one can easily deduce necessary barrier and cap thicknesses by solving $p^{(1)} = 0$.

A.1.5 Accounting for the AlN interlayer

Most of the modern III-N structures employ an AlN interlayer at barrier/channel interface to improve mobility and enhance carrier concentration. It is relatively easy to include this interlayer in the model. The interlayer is very thin (~ 1 nm) so no 2DHG forms at the barrier/interlayer interface.

Gauss law (Displacement continuity):

$$\begin{aligned}
&-\epsilon_{ch}E_{ch}^{(i-1)} + \epsilon_b E_b^{(i)} = q(p^{(i)} - \sigma_b + \sigma_{ch}) \\
&-\epsilon_b E_b^{(i)} + \epsilon_{int}E_{int}^{(i)} = q(\sigma_b - \sigma_{int}) \\
&-\epsilon_{int}E_{int}^{(i)} + \epsilon_{ch}E_{ch}^{(i)} = q(\sigma_{int} - \sigma_{ch} - n^{(i)}) \\
&i = \overline{1,N} \quad E_{ch}^{(0)} = E_{cap} \quad E_{ch}^{(N)} = E_{buff}
\end{aligned} \tag{A.13}$$

Summing up second and third equation and leaving the first unchanged in (A.13) results in exactly the same set of equations as (A.1) and ,thus, the expressions for carriers vs field (A.2) do not change. However, the expression for barrier field is now different. One needs to change (A.3) to account for a total drop in the barrier and the interlayer:

$$\begin{aligned}
-qd_bE_b^{(i)} &= E_g^{ch} + \Delta E_{f,v}^{(i)} + \Delta E_{f,c}^{(i)} + E_{int}^{(i)}d_{int} && i = \overline{1,N} \\
qd_{ch}E_{ch}^{(i)} &= E_g^{ch} + \Delta E_{f,c}^{(i)} + \Delta E_{f,v}^{(i+1)} && i = \overline{1,N-1}
\end{aligned} \tag{A.14}$$

Using the second equation in (A.13) to express $E_{int}^{(i)}$ as a function of $E_b^{(i)}$ and plugging it into (A.14) provides the expression for $E_b^{(i)}$. From that arises again an expression similar to (A.15):

$$\begin{aligned}
p^{(i)} &= \left[\Delta\sigma + \frac{\sigma_{int} - \sigma_b}{1 + \frac{\epsilon_{int}}{\epsilon_b}\frac{d_b}{d_{int}}}\right] - \\
&- \frac{1}{q^2}\left[\frac{\epsilon_{ch}}{d_{ch}}\left(E_g^{ch} + \Delta_{c,i-1}^{v,i}\right) + \frac{1}{\frac{d_b}{\epsilon_b} + \frac{d_{int}}{\epsilon_{int}}}\left(E_g^{ch} + \Delta_{c,i}^{v,i}\right)\right] \\
&\qquad i = \overline{2,N} \\
n^{(i)} &= \left[\Delta\sigma + \frac{\sigma_{int} - \sigma_b}{1 + \frac{\epsilon_{int}}{\epsilon_b}\frac{d_b}{d_{int}}}\right] - \\
&- \frac{1}{q^2}\left[\frac{\epsilon_{ch}}{d_{ch}}\left(E_g^{ch} + \Delta_{c,i}^{v,i+1}\right) + \frac{1}{\frac{d_b}{\epsilon_b} + \frac{d_{int}}{\epsilon_{int}}}\left(E_g^{ch} + \Delta_{c,i}^{v,i}\right)\right] \\
&\qquad i = \overline{1,N-1} \\
\Delta_{c,l}^{v,k} &= \Delta E_{f,v}^{(k)} + \Delta E_{f,c}^{(l)}
\end{aligned} \tag{A.15}$$

These expressions differ from (A.15) by the following changes:

$$\begin{aligned} \Delta\sigma &\longrightarrow \Delta\sigma + \frac{\sigma_{int} - \sigma_b}{1 + \frac{\epsilon_{int}}{\epsilon_b}\frac{d_b}{d_{int}}} \\ \frac{\epsilon_b}{d_b} &\longrightarrow \frac{1}{\frac{d_b}{\epsilon_b} + \frac{d_{int}}{\epsilon_{int}}} \end{aligned} \tag{A.16}$$

As d_{int} is usually at least 5-10 times smaller than d_b and their permittivities are similar the second substitution makes almost no change. Thus the effect of interlayer consists mostly in increasing of $\Delta\sigma$ by $\frac{\sigma_{int}-\sigma_b}{1+\frac{\epsilon_{int}}{\epsilon_b}\frac{d_b}{d_{int}}}$ and thus just shifting the carrier concentration for a given barrier thickness. This substitution is also valid for the top and bottom channels.

A.2 Model for doped structures

A.2.1 General case and middle channels

When doping is considered the field is not constant anymore so attention should be paid to write (A.1) using field at appropriate points as well as to use the quadratic potential profile to calculate drops in (A.3). Now period index (i) refers to a coordinate shift by $i(d_b + d_{ch})$ from the origin chosen at cap/first barrier interface.

Gauss law (Displacement continuity):

$$\begin{aligned} &-\epsilon_{ch}E_{ch}^{(i-1)}[d_b + d_{ch}] + \epsilon_b E_b^{(i)}[0] = q(p^{(i)} - \Delta\sigma) \\ &-\epsilon_b E_b^{(i)}[d_b] + \epsilon_{ch}E_{ch}^{(i)}[d_b] = q(\Delta\sigma - n^{(i)}) \\ &i = \overline{1, N} \\ &E_{ch}^{(0)}[d_b + d_{ch}] = E_{cap}[0] \quad E_{ch}^{(N)}[d_b] = E_{buff}[N(d_b + d_{ch})] \end{aligned} \tag{A.17}$$

(A.17) gives carrier concentrations vs field dependence:

$$\begin{aligned} p^{(i)} &= \Delta\sigma - \frac{\epsilon_{ch}E_{ch}^{(i-1)}[d_b + d_{ch}] - \epsilon_b E_b^{(i)}[0]}{q} \qquad i = \overline{1, N} \\ n^{(i)} &= \Delta\sigma - \frac{\epsilon_{ch}E_{ch}^{(i)}[d_b] - \epsilon_b E_b^{(i)}[d_b]}{q} \qquad i = \overline{1, N} \end{aligned} \tag{A.18}$$

The Fermi level continuity yields:

$$\begin{aligned} q\Delta V_b^{(i)} &= E_g^{ch} + \Delta E_{f,v}^{(i)} + \Delta E_{f,c}^{(i)} \quad i = \overline{1,N} \\ -q\Delta V_{ch}^{(i)} &= E_g^{ch} + \Delta E_{f,c}^{(i)} + \Delta E_{f,v}^{(i+1)} \quad i = \overline{1,N-1} \end{aligned} \tag{A.19}$$

One can write potential drops $\Delta V_{ch}^{(i)}$ and $\Delta V_b^{(i)}$ from Poisson equation, use (A.19) and then get expression for $E_{ch}^{(i)}[d_b]$ and $E_b^{(i)}[0]$.

$$\begin{aligned} qE_{ch}^{(i)}[d_b] &= \frac{1}{d_{ch}}\left(E_g^{ch} + \Delta_{c,i}^{v,i+1} - \frac{q(N_D^{ch} - N_A^{ch})}{\epsilon_{ch}}\frac{d_{ch}^2}{2}\right) \\ qE_b^{(i)}[0] &= -\frac{1}{d_b}\left(E_g^{ch} + \Delta_{c,i}^{v,i+1} + \frac{q(N_D^{b} - N_A^{b})}{\epsilon_{b}}\frac{d_{b}^2}{2}\right) \\ \Delta_{c,l}^{v,k} &= \Delta E_{f,v}^{(k)} + \Delta E_{f,c}^{(l)} \end{aligned} \tag{A.20}$$

Leading to

$$\begin{aligned} q\Delta V_b^{(i)} &= V^{(i)}[d_b] - V^{(i)}[0] = -qE_b^{(i)}[0] - \frac{q^2(N_D^b - N_A^b)}{\epsilon_b}\frac{d_b^2}{2} \\ -q\Delta V_{ch}^{(i)} &= V^{(i)}[d_b + d_{ch}] - V^{(i)}[d_b] = qE_{ch}^{(i)}[d_b]d_{ch} + \frac{q^2(N_D^{ch} - N_A^{ch})}{\epsilon_{ch}}\frac{d_{ch}^2}{2} \end{aligned} \tag{A.21}$$

Using Poisson equation for electric field and (A.20) yields $E_{ch}^{(i)}[d_b + d_{ch}]$ and $E_b^{(i)}[d_b]$

$$\begin{aligned} qE_{ch}^{(i)}[d_b + d_{ch}] &= \frac{1}{d_{ch}}\left(E_g^{ch} + \Delta_{v,i+1}^{c,i} + \frac{q(N_D^{ch} - N_A^{ch})}{\epsilon_{ch}}\frac{d_{ch}^2}{2}\right) \\ qE_b^{(i)}[d_b] &= -\frac{1}{d_b}\left(E_g^{ch} + \Delta_{v,i+1}^{c,i} - \frac{q(N_D^{b} - N_A^{b})}{\epsilon_{b}}\frac{d_{b}^2}{2}\right) \end{aligned} \tag{A.22}$$

Now everything is obtained to get carrier expressions:

$$\begin{aligned} p^{(i)} = \Delta\sigma - \frac{1}{q^2}\left[\frac{\epsilon_{ch}}{d_{ch}}\left(E_g^{ch} + \Delta_{c,i-1}^{v,i}\right) + \frac{\epsilon_b}{d_b}\left(E_g^{ch} + \Delta_{c,i}^{v,i}\right)\right] - \\ - \frac{(N_D^{ch} + N_A^{ch})d_{ch} + (N_D^b - N_A^b)d_b}{2} \quad i = \overline{2,N} \\ n^{(i)} = \Delta\sigma - \frac{1}{q^2}\left[\frac{\epsilon_{ch}}{d_{ch}}\left(E_g^{ch} + \Delta_{c,i}^{v,i+1}\right) + \frac{\epsilon_b}{d_b}\left(E_g^{ch} + \Delta_{c,i}^{v,i}\right)\right] + \\ + \frac{(N_D^{ch} - N_A^{ch})d_{ch} + (N_D^b - N_A^b)d_b}{2} \quad i = \overline{1,N-1} \end{aligned} \tag{A.23}$$

It is easy to see that concentrations are the same as for undoped case minus (for holes)/plus

(for electrons) half of the total doping. So when doping the structure which has holes in the undoped state, half of the total doping goes to compensate holes and another half to enhance electrons in case of n doping and vise versa for p doping. All this is valid only if 2DHGs are still present in the structure (light enough doping). The situation when they are not is considered further.

A.2.2 Superlattice

In case of superlattice again we can write a very simple solution:

$$\begin{aligned} p &= \Delta\sigma - \frac{E_g^{ch} + \Delta}{q^2}\left[\frac{\epsilon_{ch}}{d_{ch}} + \frac{\epsilon_b}{d_b}\right] - \\ &\quad - \frac{(N_D^{ch} - N_A^{ch})d_{ch} + (N_D^b - N_A^b)d_b}{2} \\ n &= \Delta\sigma - \frac{E_g^{ch} + \Delta}{q^2}\left[\frac{\epsilon_{ch}}{d_{ch}} + \frac{\epsilon_b}{d_b}\right] + \\ &\quad + \frac{(N_D^{ch} - N_A^{ch})d_{ch} + (N_D^b - N_A^b)d_b}{2} \end{aligned} \tag{A.24}$$

And again it turns out to be the solution for the middle channels in a finite multi-channel if 2DHGs are present.

A.2.3 Top channel

Similarly to the undoped case the top channel has to be treated separately. First the case $p^{top} \neq 0$.

Gauss + Fermi level continuity in the cap + Poisson:

$$\begin{aligned} p^{(1)} &= \Delta\sigma - \frac{1}{q}\left(\epsilon_{ch}E_{cap}[0] - \epsilon_b E_b[0]\right) \\ \Delta V_{cap} &= -\frac{1}{q}\left(E_g^{ch} + q\Phi_b - \Delta E_{f,v}^{(1)}\right) = \\ &= -E_{cap}[0] - \frac{q}{\epsilon_{ch}}\left(N_D^{cap} - N_A^{cap}\right)\frac{d_{cap}^2}{2} \end{aligned} \tag{A.25}$$

Finally, using (A.20) for $E_b[0]$ one gets:

$$\begin{aligned} p^{(1)} = \Delta\sigma - \frac{E_g^{ch} + \Delta_{c,1}^{v,1}}{q^2}\left[\frac{\epsilon_{ch}}{d_{cap}} + \frac{\epsilon_b}{d_b}\right] + \frac{q\Phi_b + \Delta E_{f,c}^{(1)}}{q^2}\frac{\epsilon_b}{d_b} - \\ - (N_D^b - N_A^b)\frac{d_b}{2} - (N_D^{cap} - N_A^{cap})\frac{d_{cap}}{2} \end{aligned} \tag{A.26}$$

If $p^{top} = 0$ but other 2DHGs are present (namely $p^{(2)} \neq 0$) similarly to the undoped case we express $\Delta E^{(1)}_{f,v}$ from the condition $p^{(1)} = 0$ and plug it in the general expression for $n^{(1)}$ and we obtain:

$$n^{(1)} = \frac{\Delta\sigma - (N_D^b - N_A^b)\frac{d_b}{2} - (N_D^{cap} - N_A^{cap})\frac{d_{cap}}{2} - \frac{q\Phi_b + \Delta E^{(1)}_{f,c}}{q^2}\frac{\epsilon_b}{d_b} - \frac{E_g^{ch} + \Delta^{c,1}_{v,2}}{q^2}\frac{\epsilon_{ch}}{d_{ch}} + (N_D^b - N_A^b)d_b + (N_D^{ch} - N_A^{ch})\frac{d_{ch}}{2} + (N_D^{cap} - N_A^{cap})\frac{d_{cap}}{2}}{1 + \frac{\epsilon_b}{\epsilon_{ch}}\frac{d_{cap}}{d_b}} \tag{A.27}$$

This expression is equivalent to the one presented in ([46]). After usual assumptions for Δ one can use it directly as thin cap case when 2DHGs are present in the middle channels. However, if middle channel 2DHGs are also absent one has to find a way to express $\Delta E^{(2)}_{f,v}$ independently. This situation is discussed below.

A.2.4 Bottom channel

Similarly to the undoped cae:

$$n^{(N)} = \Delta\sigma - \frac{1}{q}\left(\epsilon_{ch}E_{buff}[W_{dep}^{buff}] - \epsilon_b E_b^{(N)}[d_b]\right) \tag{A.28}$$

where W_{dep}^{buff} is a point such that $E_{buff}[W_{dep}^{buff}] = 0$.

From above follows the expression for $n^{(N)}$:

$$n^{(N)} = \Delta\sigma - \frac{E_g^{ch} + \Delta^{v,N}_{c,N}}{q^2}\frac{\epsilon_b}{d_b} + (N_D^b - N_A^b)\frac{d_b}{2} + (N_D^{buff} - N_A^{buff})W_{dep}^{buff} \tag{A.29}$$

A.2.5 No 2DHGs: middle channels

In the undoped structure $p^{mid} = 0$ is equivalent to $n^{mid} = 0$ and such structures do not present practical interest (what for one would use multi-channel with empty middle channels). In the doped case this is not true, thus it is necessary to consider the case when $p^{(i)} = 0\ \forall\ i$ and derive corresponding $n^{(i)}$. The inverse situation (no 2DEGs but only 2DHGs present) is not considered here as it is not present in current applications, however, one should be able to derive expressions for this case in a similar way.

$p^{(i)} = 0$ implies that corresponding $\Delta E_{f,v}^{(i)}$ can not be simply kicked out anymore as it is negative with unknown magnitude. However, one can notice that:

$$\begin{aligned} n^{(i)} - p^{(i)} = n^{(i)} =& (N_D^b - N_A^b)d_b + (N_D^{ch} - N_A^{ch})d_{ch} - \\ & - \frac{1}{q^2}\frac{\epsilon_{ch}}{d_{ch}}\left(\Delta E_{f,v}^{(i+1)} - \Delta E_{f,v}^{(i)}\right) \end{aligned} \tag{A.30}$$

And from conditions $p^{(i+1)} = p^{(i)} = 0$ one can express $\Delta E_{f,v}^{(i)}$ and $\Delta E_{f,v}^{(i+1)}$ and find out that:

$$\begin{aligned} \Delta E_{f,v}^{(i+1)} - \Delta E_{f,v}^{(i)} = q^2 \Bigg[& \frac{\epsilon_{ch}}{d_{ch}}\left(\Delta E_{f,c}^{(i-1)} - \Delta E_{f,c}^{(i)}\right) + \\ & + \frac{\epsilon_b}{d_b}\left(\Delta E_{f,c}^{(i)} - \Delta E_{f,c}^{(i+1)}\right)\Bigg] \end{aligned} \tag{A.31}$$

As 2DEGs are present in peridos $i-1,\ i,\ i+1$, $\Delta E_{f,c}^{(i-1)} \approx \Delta E_{f,c}^{(i)} \approx \Delta E_{f,c}^{(i+1)}$ and thus $\Delta E_{f,v}^{(i+1)} - \Delta E_{f,v}^{(i)} \approx 0$ leading to the expression for middle channel carrier densities:

$$n^{(i)} = (N_D^b - N_A^b)d_b + (N_D^{ch} - N_A^{ch})d_{ch} \quad i = \overline{2, N-1} \tag{A.32}$$

Thus, in such a structure the 2DEG density simply equals total net n doping introduced in the structure and is completely independent from channel thickness. N_D, d_b, d_{ch} that delimit the case described by equation (A.23) from the one described by equation (A.32) are the ones that satisfy the relation $p_{undoped}^{mid} = [(N_D^b - N_A^b)d_b + (N_D^{ch} - N_A^{ch})d_{ch}]/2$.

A.2.6 No 2DHGs: bottom channel

For the bottom most channel equation (A.30) doesn't make sense as $\Delta E_{f,v}^{(N+1)}$ is undefined. Thus, one has to explicitly express $\Delta E_{f,v}^{(N)}$ from the condition $p^{(N)} = 0$ in (A.23) and plug it in the equation (A.29). After a careful calculation and assuming $\Delta E_{f,c}^{(N-1)} - \Delta E_{f,c}^{(N)} \approx 0$ for the same reasons as before one gets:

$$\begin{aligned} n^{(N)} =& \frac{\Delta\sigma - (N_D^b - N_A^b)\frac{d_b}{2} - (N_D^{ch} - N_A^{ch})\frac{d_{ch}}{2}}{1 + \frac{\epsilon_b}{\epsilon_{ch}}\frac{d_{ch}}{d_b}} + \\ & + (N_D^b - N_A^b)d_b + (N_D^{ch} - N_A^{ch})\frac{d_{ch}}{2} + \\ & + (N_D^{buff} - N_A^{buff})W_{dep}^{buff} \end{aligned} \tag{A.33}$$

The first term is a quite unexpected addition to the total net n doping represented by other

terms. First, it turns out that last channel is different from middle ones (and can be both more and less populated). Second, in this case the last channel concentration depends on channel thickness.

A.2.7 No 2DHGs: top channel

In case there is no 2DHGs at all in the system one needs to express $\Delta E^{(2)}_{f,v}$ and plug it in expression (A.27). After simplifying by setting $\Delta E^{(1)}_{f,c} \approx \Delta E^{(2)}_{f,c}$ the following expression is obtained:

$$\begin{aligned} n^{(1)} = & \frac{\Delta\sigma - (N_D^b - N_A^b)\frac{d_b}{2} - (N_D^{cap} - N_A^{cap})\frac{d_{cap}}{2} - \frac{q\Phi_b + \Delta E^{(1)}_{f,c}}{q^2}\frac{\epsilon_b}{d_b}}{1 + \frac{\epsilon_b}{\epsilon_{ch}}\frac{d_{cap}}{d_b}} - \\ & - \frac{\Delta\sigma - (N_D^b - N_A^b)\frac{d_b}{2} - (N_D^{ch} - N_A^{ch})\frac{d_{ch}}{2}}{1 + \frac{\epsilon_b}{\epsilon_{ch}}\frac{d_{ch}}{d_b}} + \\ & + (N_D^b - N_A^b)d_b + (N_D^{ch} - N_A^{ch})\frac{d_{ch}}{2} + (N_D^{cap} - N_A^{cap})\frac{d_{cap}}{2} \end{aligned} \tag{A.34}$$

A.3 Error definition

The average absolute error (A.E.) in a given optimization region was defined according to the following formula:

$$A.E. = \frac{1}{N} \sum_{\text{all } d_b,\, d_{ch} \text{ such that } n^{mid} > thr} |n^{simulation} - n^{model}| \tag{A.35}$$

Where thr is the chosen optimization region threshold: 5×10^{12} cm^{-2} for high density optimization region and and a wider one - all the structures with 1×10^{12} cm^{-2} for the low density one. N is the number of points averaged.

The average relative error (R.E.) in a given optimization region is defined in a similar way as the mean value of relative errors under the same conditions:

$$R.E. = \frac{1}{N} \sum_{\text{all } d_b,\, d_{ch} \text{ such that } n^{mid} > thr} \frac{|n^{simulation} - n^{model}|}{n^{simulation}} \tag{A.36}$$

A.4 Simulation details

All the simulations were performed using commercially available NextNano software with standard database parameters. Important parameters are listed in Table I. Difference in carrier

concentrations obtained (<1×10^{12} cm^{-2}) with Poisson-Schrodinger and Poisson only solutions for reference structures with carrier densities exceeding 1×10^{12} cm^{-2} (model application region) was within the model error. As fully coupled solution is very time consuming, only Poisson solution was employed for additional points.

Table A.1 – Material parameters used.

	GaN	$Al_{0.3}GaN$	$In_{0.17}AlN$
E_g^{ch} [eV]	3.44	3.96	4.87
$\Delta\sigma$ [cm^{-2}]	0	1.49×10^{13}	2.5×10^{13}
ϵ [1]	10.1	9.641	9.56

Table A.2 – Summary of the model: expressions to use in each case.

		Top		**Middle**		**Bottom**	
		n^{top}	p^{top}	n^{mid}	p^{mid}	n^{bot}	p^{bot}
Undoped	$p=0$	(12)	0	0	0	N/A [I]	0
	$p\neq0$	(4)	(9)	(4)	(4)	(8)	(4)
Doped	$p^{top}=0$ [II]	(27)	0	(23)	(23)	(29)	(23)
	$p=0\ \forall i$	(34)	0	(32)	0	(33)	0
	$p\neq0\ \forall i$	(26)	(23)	(23)	(23)	(29)	(23)

Bibliography

[1] (), [Online]. Available: https://www.nobelprize.org/prizes/physics/2014/summary/.

[2] Yole Development, "GaN RF Market: Applications, Players, Technology and Substrates 2020", 2020.

[3] ——, "GaN Power 2021: Epitaxy, Devices, Applications and Technology Trends report", 2021.

[4] U. K. Mishra, L. Shen, T. E. Kazior, and Y.-F. Wu, "Gan-based rf power devices and amplifiers", *Proceedings of the IEEE*, vol. 96, no. 2, pp. 287–305, 2008. DOI: 10.1109/JPROC.2007.911060.

[5] (), [Online]. Available: https://www.electronicproducts.com/gan-provides-revolutionary-improvements-in-power/.

[6] (), [Online]. Available: https://www.pi-innovo.com/gan/#.

[7] (), [Online]. Available: https://www.yankodesign.com/2021/05/25/ankers-tiny-65w-gan-charger-compresses-a-laptop-charging-brick-to-the-size-of-an-ice-cube/.

[8] ON Semiconductor, "The Difference Between GaN and SiC Transistors", 2020.

[9] (), [Online]. Available: https://nexgenpowersystems.com/verticalgan/.

[10] B. J. Baliga, *Fundamentals of Power Semiconductor Devices*, 1st ed. Springer US, 2008, ISBN: 978-0-387-47314-7.

[11] L. Nela, J. Ma, C. Erine, P. Xiang, T.-H. Shen, V. Tileli, T. Wang, K. Cheng, and E. Matioli, "Multi-channel nanowire devices for efficient power conversion", *Nature Electronics*, vol. 4, no. 4, pp. 284–290, Apr. 2021, ISSN: 2520-1131. DOI: 10.1038/s41928-021-00550-8. [Online]. Available: https://doi.org/10.1038/s41928-021-00550-8.

[12] J. Ma, C. Erine, M. Zhu, N. Luca, P. Xiang, K. Cheng, and E. Matioli, "1200 v multi-channel power devices with 2.8 •mm on-resistance", in *2019 IEEE International Electron Devices Meeting (IEDM)*, 2019, pp. 4.1.1–4.1.4. DOI: 10.1109/IEDM19573.2019.8993536.

[13] D. J. C. Wood, *Polarization Effects in Semiconductors*, 1st ed. Springer US, 2008, ISBN: 978-0-387-68319-5.

[14] L. Nela, J. Ma, C. Erine, P. Xiang, T.-H. Shen, V. Tileli, T. Wang, K. Cheng, and E. Matioli, "Multi-channel nanowire devices for efficient power conversion", *Nature Electronics*, Mar. 2021, ISSN: 2520-1131. DOI: 10.1038/s41928-021-00550-8. [Online]. Available: https://doi.org/10.1038/s41928-021-00550-8.

[15] Y. Cao, K. Wang, G. Li, T. Kosel, H. Xing, and D. Jena, "Mbe growth of high conductivity single and multiple aln/gan heterojunctions", *Journal of Crystal Growth*, vol. 323, no. 1, pp. 529–533, 2011, Proceedings of the 16th International Conference on Molecular Beam Epitaxy (ICMBE), ISSN: 0022-0248. DOI: https://doi.org/10.1016/j.jcrysgro.2010.12.047. [Online]. Available: https://www.sciencedirect.com/science/article/pii/S002202481001208X.

[16] C. Erine, J. Ma, G. Santoruvo, and E. Matioli, "Multi-channel algan/gan in-plane-gate field-effect transistors", *IEEE Electron Device Letters*, vol. 41, no. 3, pp. 321–324, 2020. DOI: 10.1109/LED.2020.2967458.

[17] P. Sohi, J.-F. Carlin, M. D. Rossell, R. Erni, N. Grandjean, and E. Matioli, "High conductivity InAlN/GaN multi-channel two-dimensional electron gases", *Semiconductor Science and Technology*, vol. 36, no. 5, p. 055 020, Apr. 2021. DOI: 10.1088/1361-6641/abf3a7. [Online]. Available: https://doi.org/10.1088/1361-6641/abf3a7.

[18] J. Ma, G. Kampitsis, P. Xiang, K. Cheng, and E. Matioli, "Multi-channel tri-gate gan power schottky diodes with low on-resistance", *IEEE Electron Device Letters*, vol. 40, no. 2, pp. 275–278, 2019. DOI: 10.1109/LED.2018.2887199.

[19] J. Ma, C. Erine, P. Xiang, K. Cheng, and E. Matioli, "Multi-channel tri-gate normally-on/off algan/gan moshemts on si substrate with high breakdown voltage and low on-resistance", *Applied Physics Letters*, vol. 113, no. 24, p. 242 102, 2018. DOI: 10.1063/1.5064407. eprint: https://doi.org/10.1063/1.5064407. [Online]. Available: https://doi.org/10.1063/1.5064407.

[20] C. Erine, J. Ma, G. Santoruvo, and E. Matioli, "Multi-channel algan/gan in-plane-gate field-effect transistors", *IEEE Electron Device Letters*, vol. 41, no. 3, pp. 321–324, 2020. DOI: 10.1109/LED.2020.2967458.

[21] L. Nela, H. K. Yildirim, C. Erine, R. Van Erp, P. Xiang, K. Cheng, and E. Matioli, "Conformal passivation of multi-channel gan power transistors for reduced current collapse", *IEEE Electron Device Letters*, pp. 1–1, 2020. DOI: 10.1109/LED.2020.3038808.

[22] K. Shinohara, C. King, E. Regan, M. P. Gomez, J. Bergman, A. Carter, A. Arias, M. Urteaga, B. Brar, R. Page, R. Chaudhuri, M. Islam, H. G. Xing, and D. Jena, "(invited) GaN-based multiple 2deg channel BRIDGE (buried dual gate) HEMT technology for high power and linearity", *ECS Transactions*, vol. 92, no. 4, pp. 103–108, Jul. 2019. DOI: 10.1149/09204.0103ecst. [Online]. Available: https://doi.org/10.1149%2F09204.0103ecst.

[23] K. Shinohara, C. King, E. J. Regan, J. Bergman, A. D. Carter, A. Arias, M. Urteaga, B. Brar, R. Page, R. Chaudhuri, M. Islam, H. Xing, and D. Jena, "Gan-based multi-channel transistors with lateral gate for linear and efficient millimeter-wave power amplifiers",

in *2019 IEEE MTT-S International Microwave Symposium (IMS)*, 2019, pp. 1133–1135. DOI: 10.1109/MWSYM.2019.8700845.

[24] J. Chang, S. Afroz, K. Nagamatsu, K. Frey, S. Saluru, J. Merkel, S. Taylor, E. Stewart, S. Gupta, and R. Howell, "The super-lattice castellated field-effect transistor: a high-power, high-performance rf amplifier", *IEEE Electron Device Letters*, vol. 40, no. 7, pp. 1048–1051, 2019. DOI: 10.1109/LED.2019.2917285.

[25] R. S. Howell, E. J. Stewart, R. Freitag, J. Parke, B. Nechay, H. Cramer, M. King, S. Gupta, J. Hartman, M. Snook, I. Wathuthanthri, P. Ralston, K. Renaldo, H. G. Henry, and R. C. Clarke, "The super-lattice castellated field effect transistor (slcfet): a novel high performance transistor topology ideal for rf switching", in *2014 IEEE International Electron Devices Meeting*, 2014, pp. 11.5.1–11.5.4. DOI: 10.1109/IEDM.2014.7047033.

[26] M. Xiao, Y. Ma, Z. Du, X. Yan, R. Zhang, K. Cheng, K. Liu, A. Xie, E. Beam, Y. Cao, H. Wang, and Y. Zhang, "5 kv multi-channel algan/gan power schottky barrier diodes with junction-fin-anode", in *2020 IEEE International Electron Devices Meeting (IEDM)*, 2020, pp. 5.4.–5.4.

[27] S. Heikman, S. Keller, D. S. Green, S. P. DenBaars, and U. K. Mishra, "High conductivity modulation doped algan/gan multiple channel heterostructures", *Journal of Applied Physics*, vol. 94, no. 8, pp. 5321–5325, 2003. DOI: 10.1063/1.1610244. eprint: https://aip.scitation.org/doi/pdf/10.1063/1.1610244. [Online]. Available: https://aip.scitation.org/doi/abs/10.1063/1.1610244.

[28] Y. Cao, K. Wang, G. Li, T. Kosel, H. Xing, and D. Jena, "Mbe growth of high conductivity single and multiple aln/gan heterojunctions", *Journal of Crystal Growth*, vol. 323, no. 1, pp. 529–533, 2011, Proceedings of the 16th International Conference on Molecular Beam Epitaxy (ICMBE), ISSN: 0022-0248. DOI: https://doi.org/10.1016/j.jcrysgro.2010.12.047. [Online]. Available: https://www.sciencedirect.com/science/article/pii/S002202481001208X.

[29] D. Liu, "Design, fabrication and characterizationof inalas/ingaas/inasp composite channel hemts", dissertation, The Ohio State University, 2008. [Online]. Available: https://www.researchgate.net/publication/267259044_DESIGN_FABRICATION_AND_CHARACTERIZATION_OF_INALASINGAASINASP_COMPOSITE_CHANNEL_HEMTS.

[30] (), [Online]. Available: https://www.st.com/content/st_com/en/about/innovation---technology/GaN.html.

[31] A. Nakajima, P. Liu, M. Ogura, T. Makino, K. Kakushima, S.-i. Nishizawa, H. Ohashi, S. Yamasaki, and H. Iwai, "Generation and transportation mechanisms for two-dimensional hole gases in gan/algan/gan double heterostructures", *Journal of Applied Physics*, vol. 115, no. 15, p. 153 707, 2014. DOI: 10.1063/1.4872242. eprint: https://doi.org/10.1063/1.4872242. [Online]. Available: https://doi.org/10.1063/1.4872242.

[32] R. Chaudhuri, S. J. Bader, Z. Chen, D. A. Muller, H. G. Xing, and D. Jena, "A polarization-induced 2d hole gas in undoped gallium nitride quantum wells", *Science*, vol. 365, no. 6460, pp. 1454–1457, 2019, ISSN: 0036-8075. DOI: 10.1126/science.aau8623. eprint: https://science.sciencemag.org/content/365/6460/1454.full.pdf. [Online]. Available: https://science.sciencemag.org/content/365/6460/1454.

[33] L. P., K. K., I. H., N. A, M. T., O. M, N. S., and O. H., in *1st IEEE Work. Wide Bandgap Power Devices Appl. WiPDA 2013)*, 2013.

[34] J. P. Ibbetson, P. T. Fini, K. D. Ness, S. P. DenBaars, J. S. Speck, and U. K. Mishra, "Polarization effects, surface states, and the source of electrons in algan/gan heterostructure field effect transistors", *Applied Physics Letters*, vol. 77, no. 2, pp. 250–252, 2000. DOI: 10.1063/1.126940. eprint: https://doi.org/10.1063/1.126940. [Online]. Available: https://doi.org/10.1063/1.126940.

[35] Y. Qian, F. Shang, Q. Wan, and Y. Yan, "A molecular dynamics study on indentation response of single crystalline wurtzite gan", *Journal of Applied Physics*, vol. 124, no. 11, p. 115 102, 2018. DOI: 10.1063/1.5041738. eprint: https://doi.org/10.1063/1.5041738. [Online]. Available: https://doi.org/10.1063/1.5041738.

[36] C. Erine, L. Nela, A. Miranzadeh, and E. Matioli, "Simple analytical model for multi-channel high-electron-mobility iii-n heterostructures", *Journal of Applied Physics*, 2021. DOI: submitted.

[37] L. Nela, C. Erine, A. Miranzadeh, and E. Matioli, "Intrinsic polarization super junctions: application to single and multi-channel structures", 2021. DOI: submitted.

[38] S. Han, J. Song, and R. Chu, "Design of gan/algan/gan super-heterojunction schottky diode", *IEEE Transactions on Electron Devices*, vol. 67, no. 1, pp. 69–74, 2020. DOI: 10.1109/TED.2019.2953843.

[39] S. .-W. Han, J. Song, S. H. Yoo, Z. Ma, R. M. Lavelle, D. W. Snyder, J. M. Redwing, T. N. Jackson, and R. Chu, "Experimental demonstration of charge-balanced gan super-heterojunction schottky barrier diode capable of 2.8 kv switching", *IEEE Electron Device Letters*, pp. 1–1, 2020. DOI: 10.1109/LED.2020.3029619.

[40] H. Ishida, D. Shibata, H. Matsuo, M. Yanagihara, Y. Uemoto, T. Ueda, T. Tanaka, and D. Ueda, "Gan-based natural super junction diodes with multi-channel structures", in *2008 IEEE International Electron Devices Meeting*, 2008, pp. 1–4. DOI: 10.1109/IEDM.2008.4796636.

[41] H. Ishida, D. Shibata, M. Yanagihara, Y. Uemoto, H. Matsuo, T. Ueda, T. Tanaka, and D. Ueda, "Unlimited high breakdown voltage by natural super junction of polarized semiconductor", *IEEE Electron Device Letters*, vol. 29, no. 10, pp. 1087–1089, 2008. DOI: 10.1109/LED.2008.2002753.

[42] J. Ma and E. Matioli, "Slanted tri-gates for high-voltage gan power devices", *IEEE Electron Device Letters*, vol. 38, no. 9, pp. 1305–1308, 2017. DOI: 10.1109/LED.2017.2731799.

[43] H. Morkoc, *Handbook of Nitride Semiconductors and Devices*. Willey, 2008, ISBN: 978-3-527-40839-9.

[44] J. Qu, J. Li, and G. Zhang, "Algangan heterostructure grown by metalorganic vapor phase epitaxy", *Solid State Communications*, vol. 107, no. 9, pp. 467–470, 1998, ISSN: 0038-1098. DOI: https://doi.org/10.1016/S0038-1098(98)00253-1. [Online]. Available: https://www.sciencedirect.com/science/article/pii/S0038109898002531.

[45] Y. Cordier, M. Hugues, P. Lorenzini, F. Semond, F. Natali, and J. Massies, "Electron mobility and transfer characteristics in algan/gan hemts", *physica status solidi (c)*, vol. 2, no. 7, pp. 2720–2723, 2005. DOI: https://doi.org/10.1002/pssc.200461470. eprint: https://onlinelibrary.wiley.com/doi/pdf/10.1002/pssc.200461470. [Online]. Available: https://onlinelibrary.wiley.com/doi/abs/10.1002/pssc.200461470.

[46] E. T. Yu, X. Z. Dang, L. S. Yu, D. Qiao, P. M. Asbeck, S. S. Lau, G. J. Sullivan, K. S. Boutros, and J. M. Redwing, "Schottky barrier engineering in iii–v nitrides via the piezoelectric effect", *Applied Physics Letters*, vol. 73, no. 13, pp. 1880–1882, 1998. DOI: 10.1063/1.122312. eprint: https://doi.org/10.1063/1.122312. [Online]. Available: https://doi.org/10.1063/1.122312.

[47] C. Buchheim, R. Goldhahn, G. Gobsch, K. Tonisch, V. Cimalla, F. Niebelschütz, and O. Ambacher, "Electric field distribution in ganalgangan heterostructures with two-dimensional electron and hole gas", *Applied Physics Letters*, vol. 92, no. 1, p. 013 510, 2008. DOI: 10.1063/1.2830836. eprint: https://aip.scitation.org/doi/pdf/10.1063/1.2830836. [Online]. Available: https://aip.scitation.org/doi/abs/10.1063/1.2830836.

[48] J. Yan, X. Wang, Q. Wang, S. Qu, H. Xiao, E. Peng, H. Kang, C. Wang, C. Feng, H. Yin, L. Jiang, B. Li, Z. Wang, and X. Hou, "Two-dimensional electron and hole gases in inxga1xn/alyga1yn/gan heterostructure for enhancement mode operation", *Journal of Applied Physics*, vol. 116, no. 5, p. 054 502, 2014. DOI: 10.1063/1.4891732. eprint: https://doi.org/10.1063/1.4891732. [Online]. Available: https://doi.org/10.1063/1.4891732.

[49] L. Guo, X. Wang, C. Wang, H. Xiao, J. Ran, W. Luo, X. Wang, B. Wang, C. Fang, and G. Hu, "The influence of 1nm aln interlayer on properties of the al0.3ga0.7n/aln/gan hemt structure", *Microelectronics Journal*, vol. 39, no. 5, pp. 777–781, 2008, ISSN: 0026-2692. DOI: https://doi.org/10.1016/j.mejo.2007.12.005. [Online]. Available: https://www.sciencedirect.com/science/article/pii/S0026269207004065.

[50] P. Pampili and P. J. Parbrook, "Doping of iii-nitride materials", *Materials Science in Semiconductor Processing*, vol. 62, pp. 180–191, 2017, Advanced doping methods in semiconductor devices and nanostructures, ISSN: 1369-8001. DOI: https://doi.org/10.1016/j.mssp.2016.11.006. [Online]. Available: https://www.sciencedirect.com/science/article/pii/S1369800116305054.

[51] L. Nela, C. Erine, A. Miranzadeh, and E. Matioli, "Intrinsic polarization super junctions: application to single and multi-channel structures", 2021. DOI: submitted.

[52] (), [Online]. Available: https://www.lakeshore.com/docs/default-source/product-downloads/application-notes/2001-cs-max-qmsa-with-heterostructures.pdf?sfvrsn=f535f341_3.

[53] T. Fujihira, "Theory of semiconductor superjunction devices", *Japanese Journal of Applied Physics*, vol. 36, no. Part 1, No. 10, pp. 6254–6262, Oct. 1997. DOI: 10.1143/jjap.36.6254. [Online]. Available: https://doi.org/10.1143/jjap.36.6254.

[54] F. Udrea, G. Deboy, and T. Fujihira, "Superjunction power devices, history, development, and future prospects", *IEEE Transactions on Electron Devices*, vol. 64, no. 3, pp. 713–727, 2017. DOI: 10.1109/TED.2017.2658344.

[55] (), [Online]. Available: https://www.infineon.com/cms/en/product/power/mosfet/500v-900v-coolmos-n-channel-power-mosfet/.

[56] H. Ishida, D. Shibata, M. Yanagihara, Y. Uemoto, H. Matsuo, T. Ueda, T. Tanaka, and D. Ueda, "Unlimited high breakdown voltage by natural super junction of polarized semiconductor", *IEEE Electron Device Letters*, vol. 29, no. 10, pp. 1087–1089, 2008. DOI: 10.1109/LED.2008.2002753.

[57] H. Ishida, D. Shibata, H. Matsuo, M. Yanagihara, Y. Uemoto, T. Ueda, T. Tanaka, and D. Ueda, "Gan-based natural super junction diodes with multi-channel structures", in *2008 IEEE International Electron Devices Meeting*, 2008, pp. 1–4. DOI: 10.1109/IEDM.2008.4796636.

[58] A. Nakajima, K. Adachi, M. Shimizu, and H. Okumura, "Improvement of unipolar power device performance using a polarization junction", *Applied Physics Letters*, vol. 89, no. 19, p. 193 501, 2006. DOI: 10.1063/1.2372758. eprint: https://doi.org/10.1063/1.2372758. [Online]. Available: https://doi.org/10.1063/1.2372758.

[59] A. Nakajima, Y. Sumida, M. H. Dhyani, H. Kawai, and E. M. Narayanan, "Gan-based super heterojunction field effect transistors using the polarization junction concept", *IEEE Electron Device Letters*, vol. 32, no. 4, pp. 542–544, 2011. DOI: 10.1109/LED.2011.2105242.

[60] H. Kawai, S. Yagi, S. Hirata, F. Nakamura, T. Saito, Y. Kamiyama, M. Yamamoto, H. Amano, V. Unni, and E. M. S. Narayanan, "Low cost high voltage gan polarization superjunction field effect transistors", *physica status solidi (a)*, vol. 214, no. 8, p. 1 600 834, 2017. DOI: https://doi.org/10.1002/pssa.201600834. eprint: https://onlinelibrary.wiley.com/doi/pdf/10.1002/pssa.201600834. [Online]. Available: https://onlinelibrary.wiley.com/doi/abs/10.1002/pssa.201600834.

[61] B. Shankar and M. Shrivastava, "Safe operating area of polarization super-junction gan hemts and diodes", *IEEE Transactions on Electron Devices*, vol. 66, no. 10, pp. 4140–4147, 2019. DOI: 10.1109/TED.2019.2933362.

[62] A. Nakajima, P. Liu, M. Ogura, T. Makino, K. Kakushima, S.-i. Nishizawa, H. Ohashi, S. Yamasaki, and H. Iwai, "Generation and transportation mechanisms for two-dimensional hole gases in gan/algan/gan double heterostructures", *Journal of Applied Physics*, vol. 115, no. 15, p. 153 707, 2014. DOI: 10.1063/1.4872242. eprint: https://doi.org/10.1063/1.4872242. [Online]. Available: https://doi.org/10.1063/1.4872242.

[63] A. Colón, E. A. Douglas, A. J. Pope, B. A. Klein, C. A. Stephenson, M. S. Van Heukelom, A. Tauke-Pedretti, and A. G. Baca, "Demonstration of a 9kv reverse breakdown and 59m-cm2 specific on-resistance algan/gan schottky barrier diode", *Solid-State Electronics*, vol. 151, pp. 47–51, 2019, ISSN: 0038-1101. DOI: https://doi.org/10.1016/j.sse.2018.10.009. [Online]. Available: https://www.sciencedirect.com/science/article/pii/S0038110118304106.

[64] Y. Uemoto, D. Shibata, M. Yanagihara, H. Ishida, H. Matsuo, S. Nagai, N. Batta, M. Li, T. Ueda, T. Tanaka, and D. Ueda, "8300v blocking voltage algan/gan power hfet with thick poly-aln passivation", in *2007 IEEE International Electron Devices Meeting*, 2007, pp. 861–864. DOI: 10.1109/IEDM.2007.4419085.

[65] B. Song, M. Zhu, Z. Hu, K. Nomoto, D. Jena, and H. G. Xing, "Design and optimization of gan lateral polarization-doped super-junction (lpsj): an analytical study", in *2015 IEEE 27th International Symposium on Power Semiconductor Devices IC's (ISPSD)*, 2015, pp. 273–276. DOI: 10.1109/ISPSD.2015.7123442.

[66] B. Song, M. Zhu, Z. Hu, E. Kohn, D. Jena, and H. G. Xing, "Gan lateral polarsjs: polarization-doped super junctions", in *72nd Device Research Conference*, 2014, pp. 99–100. DOI: 10.1109/DRC.2014.6872316.

[67] A. Nakajima, P. Liu, M. Ogura, T. Makino, K. Kakushima, S.-i. Nishizawa, H. Ohashi, S. Yamasaki, and H. Iwai, "Generation and transportation mechanisms for two-dimensional hole gases in gan/algan/gan double heterostructures", *Journal of Applied Physics*, vol. 115, no. 15, p. 153 707, 2014. DOI: 10.1063/1.4872242. eprint: https://doi.org/10.1063/1.4872242. [Online]. Available: https://doi.org/10.1063/1.4872242.

[68] P. Liu, K. Kakushima, H. Iwai, A. Nakajima, T. Makino, M. Ogura, S. Nishizawa, and H. Ohashi, "Characterization of two-dimensional hole gas at gan/algan heterointerface", in *The 1st IEEE Workshop on Wide Bandgap Power Devices and Applications*, 2013, pp. 155–158. DOI: 10.1109/WiPDA.2013.6695585.

[69] R. Chaudhuri, S. J. Bader, Z. Chen, D. A. Muller, H. G. Xing, and D. Jena, "A polarization-induced 2d hole gas in undoped gallium nitride quantum wells", *Science*, vol. 365, no. 6460, pp. 1454–1457, 2019, ISSN: 0036-8075. DOI: 10.1126/science.aau8623. eprint: https://science.sciencemag.org/content/365/6460/1454.full.pdf. [Online]. Available: https://science.sciencemag.org/content/365/6460/1454.

[70] L. Nela, C. Erine, M. V. Oropallo, and E. Matioli, "Figures-of-merit of lateral gan power devices: modeling and comparison of hemts and psjs", DOI: submitted.

[71] B. J. Baliga, "Gallium nitride devices for power electronic applications", *Semiconductor Science and Technology*, vol. 28, no. 7, p. 074 011, Jun. 2013. DOI: 10.1088/0268-1242/28/7/074011. [Online]. Available: https://doi.org/10.1088/0268-1242/28/7/074011.

[72] W. Fulop, "Calculation of avalanche breakdown voltages of silicon p-n junctions", *Solid-State Electronics*, vol. 10, no. 1, pp. 39–43, 1967, ISSN: 0038-1101. DOI: https://doi.org/10.1016/0038-1101(67)90111-6. [Online]. Available: https://www.sciencedirect.com/science/article/pii/0038110167901116.

[73] G. Santoruvo, A. Allain, D. Ovchinnikov, and E. Matioli, "Magneto-ballistic transport in gan nanowires", *Applied Physics Letters*, vol. 109, no. 10, p. 103 102, 2016. DOI: 10.1063/1.4962332. eprint: https://doi.org/10.1063/1.4962332. [Online]. Available: https://doi.org/10.1063/1.4962332.

[74] G. Santoruvo and E. Matioli, "In-plane-gate gan transistors for high-power rf applications", *IEEE Electron Device Letters*, vol. 38, no. 10, pp. 1413–1416, 2017. DOI: 10.1109/LED.2017.2737658.

[75] J. Ma, G. Santoruvo, L. Nela, T. Wang, and E. Matioli, "Impact of fin width on tri-gate gan moshemts", *IEEE Transactions on Electron Devices*, vol. 66, no. 9, pp. 4068–4074, 2019. DOI: 10.1109/TED.2019.2925859.

[76] J. Piprek, *Nitride Semiconductor Devices: Principles and Simulation*. 2007, ISBN: 9783527610723.

[77] D. Jena, R. Page, J. Casamento, P. Dang, J. Singhal, Z. Zhang, J. Wright, G. Khalsa, Y. Cho, and H. G. Xing, "The new nitrides: layered, ferroelectric, magnetic, metallic and superconducting nitrides to boost the GaN photonics and electronics eco-system", *Japanese Journal of Applied Physics*, vol. 58, no. SC, SC0801, May 2019. DOI: 10.7567/1347-4065/ab147b. [Online]. Available: https://doi.org/10.7567/1347-4065/ab147b.

[78] D. K. de Vries, P. Stelmaszyk, and A. D. Wieck, "Intrinsic and extrinsic capacitances of in-plane-gated transistors", *Journal of Applied Physics*, vol. 79, no. 10, pp. 8087–8090, 1996. DOI: 10.1063/1.362364. eprint: https://doi.org/10.1063/1.362364. [Online]. Available: https://doi.org/10.1063/1.362364.

[79] J. S. McLean, A. D. Wieck, M. Bleder, and K. Ploog, "High frequency characteristics of in-plane-gate transistors", *Applied Physics Letters*, vol. 61, no. 11, pp. 1324–1325, 1992. DOI: 10.1063/1.107580. eprint: https://doi.org/10.1063/1.107580. [Online]. Available: https://doi.org/10.1063/1.107580.

[80] K. Ogawa, J. Allam, N. de B. Baynes, J. R. A. Cleaver, T. Mishima, and I. Ohbu, "Ultrafast characterization of an in-plane gate transistor integrated with photoconductive switches", *Applied Physics Letters*, vol. 66, no. 10, pp. 1228–1230, 1995. DOI: 10.1063/1.113245. eprint: https://doi.org/10.1063/1.113245. [Online]. Available: https://doi.org/10.1063/1.113245.

[81] K. Ogawa, J. Allam, N. D. B. Baynes, J. R. A. Cleaver, T. Mishima, and I. Ohbu, "Ultrafast characterization of in-plane-gate field-effect transistors: parasitics in laterally gated transistors", *Optical and Quantum Electronics*, vol. 28, no. 7, pp. 907–917, Jul. 1996, ISSN: 1572-817X. DOI: 10.1007/BF00820156. [Online]. Available: https://doi.org/10.1007/BF00820156.

[82] A. D. Wieck and K. Ploog, "In-plane-gated quantum wire transistor fabricated with directly written focused ion beams", *Applied Physics Letters*, vol. 56, no. 10, pp. 928–930, 1990. DOI: 10.1063/1.102628. eprint: https://doi.org/10.1063/1.102628. [Online]. Available: https://doi.org/10.1063/1.102628.

[83] J. Nieder, A. D. Wieck, P. Grambow, H. Lage, D. Heitmann, K. v. Klitzing, and K. Ploog, "One-dimensional lateral-field-effect transistor with trench gate-channel insulation", *Applied Physics Letters*, vol. 57, no. 25, pp. 2695–2697, 1990. DOI: 10.1063/1.103803. eprint: https://doi.org/10.1063/1.103803. [Online]. Available: https://doi.org/10.1063/1.103803.

[84] A. D. Wieck and K. Ploog, "High transconductance in-plane-gated transistors", *Applied Physics Letters*, vol. 61, no. 9, pp. 1048–1050, 1992. DOI: 10.1063/1.107712. eprint: https://doi.org/10.1063/1.107712. [Online]. Available: https://doi.org/10.1063/1.107712.

[85] S. Arulkumaran, G. I. Ng, C. M. Manojkumar, K. Ranjan, K. L. Teo, O. F. Shoron, S. Rajan, S. B. Dolmanan, and S. Tripathy, "In0.17al0.83n/aln/gan triple t-shape fin-hemts with gm=646 ms/mm, ion=1.03 a/mm, ioff=1.13 µa/mm, ss=82 mv/dec and dibl=28 mv/v at vd=0.5 v", in *2014 IEEE International Electron Devices Meeting*, 2014, pp. 25.6.1–25.6.4. DOI: 10.1109/IEDM.2014.7047109.

[86] K. Shinohara, C. King, A. D. Carter, E. J. Regan, A. Arias, J. Bergman, M. Urteaga, and B. Brar, "Gan-based field-effect transistors with laterally gated two-dimensional electron gas", *IEEE Electron Device Letters*, vol. 39, no. 3, pp. 417–420, 2018. DOI: 10.1109/LED.2018.2797940.

[87] K. Shinohara, C. King, E. Regan, M. P. Gomez, J. Bergman, A. Carter, A. Arias, M. Urteaga, B. Brar, R. Page, R. Chaudhuri, M. Islam, H. G. Xing, and D. Jena, "(invited) GaN-based multiple 2deg channel BRIDGE (buried dual gate) HEMT technology for high power and linearity", *ECS Transactions*, vol. 92, no. 4, pp. 103–108, Jul. 2019. DOI: 10.1149/09204.0103ecst. [Online]. Available: https://doi.org/10.1149/09204.0103ecst.

[88] G. Ulliac, S. Garidel, J.-P. Vilcot, and P. Tilmant, "Air-bridge interconnection and bondpad process for non-planar compound semiconductor devices", *Microelectronic Engineering*, vol. 81, no. 1, pp. 53–58, 2005, ISSN: 0167-9317. DOI: https://doi.org/10.1016/j.mee.2005.02.006. [Online]. Available: https://www.sciencedirect.com/science/article/pii/S0167931705000687.

[89] T.-H. Chung, W.-H. Lin, Y.-K. Chao, S.-W. Chang, and S.-Y. Lin, "In-plane gate transistors with a 40-μm -wide channel width", *IEEE Electron Device Letters*, vol. 33, no. 8, pp. 1129–1131, 2012. DOI: 10.1109/LED.2012.2199735.

[90] M. S. Nikoo, A. Jafari, and E. Matioli, "On-chip high-voltage sensors based on trap-assisted 2deg channel control", *IEEE Electron Device Letters*, vol. 40, no. 4, pp. 613–615, 2019. DOI: 10.1109/LED.2019.2898043.

[91] M. Samizadeh Nikoo, G. Santoruvo, C. Erine, A. Jafari, and E. Matioli, "On the dynamic performance of laterally gated transistors", *IEEE Electron Device Letters*, vol. 40, no. 7, pp. 1171–1174, 2019. DOI: 10.1109/LED.2019.2920116.

[92] O. Landré, D. Camacho, C. Bougerol, Y. M. Niquet, V. Favre-Nicolin, G. Renaud, H. Renevier, and B. Daudin, "Elastic strain relaxation in gan/aln nanowire superlattice", *Phys. Rev. B*, vol. 81, p. 153 306, 15 Apr. 2010. DOI: 10.1103/PhysRevB.81.153306. [Online]. Available: https://link.aps.org/doi/10.1103/PhysRevB.81.153306.

c4therine.erine@gmail.com
Catherine Erine
+33 7 815 500 50
5, rue de l'Industrie
1020 Renens
Vaud, Switzerland

Catherine ERINE

- Advanced microfabrication (Clean room)
- Fabrication process development
- E-beam and photo lithography
- Dry and wet etching
- PECVD, LPCVD, ALD, e-beam evaporation
- Semiconductor device characterization

Education

2017 – Pres. **Swiss Federal Institute of Technology (EPFL), Lausanne, Switzerland,** *PhD, 4 years*

2016 - 2017 **Pierre and Marie Curie University (UPMC), France,**
Master "Material Science and Nano-Objects", 1 year

2013 - 2017 **École Polytechnique (X), Palaiseau, France,** *Ingénieur Polytechnicien, 4 years*

2009 - 2013 **St. Petersburg State University, Russia,** *Applied Mathematics, 3.5 years*

Core experience

2017 – Pres. **PowerLab, École Polytechnique Féderale de Lausanne (EPFL), Switzerland,** *PhD, 4 years,* **"Heterostructure design and field management in III-N HEM electronic devices"**

- Developed novel heterostrutures and device architectures for energy-efficient and cost-effective GaN based power electronics improving twice the performance of state-of-art GaN power HEMTs
- Fabricated and characterized micro electronic devices using cutting-edge clean room fabrication techniques (Ebeam and optical lithography, Etching, Thin film deposition, SEM, FIB, etc)
- Automated electrical measurements using Labview reducing measurement time by factor of ten
- Developed advanced cryo Hall measurement methods for nanowire-based devices
- Performed an extensive analytical and numerical optimization of heterostructures and devices using Silvaco ATLAS, Matlab and COMSOL paving the way to ultimate device optimization within the shortest possible time

2016 - 2017 **Mixed Unit CNRS-Thalès / Irradiated Solids Laboratory (LSI) , École Polytechnique, France,** *Full-time Intern, 8 months,* **"Electronic transport in magnetic semiconductor junctions"**

- Optimized the simulation code reducing the calculation time from hours to seconds
- Designed the experiment and performed the clean room fabrication
- Experimentally demonstrated a new type of asymmetric spin transport

Additional experience

2016 - 2017 **Condensed Matter Physics Laboratory (PMC), École Polytechnique, France,**
Part-time Intern, 3 months, **"Efficiency droop in LEDs"**

- Developed Matlab code for optimization of III—N LED efficiency in disordered junctions

2012 - 2013 **St. Petersburg State University, Departement of Applied Mathematics, Russia,**
Part-time Assistant researcher, **" Haar *wavelets applied to 1D signal processing* "**

- Improved the convergence speed estimation for signal approximations by Haar wavelets

Competences

Clean room fabrication
Advanced microfabrication
GaN power electronics
Semiconductor physics
Optoelectronics
III-N and III-V semiconductors
High-electron mobility heterostructures
Electrical device characterization
Cryogenic measurements
Semiconductor device simulation
Heterostructure design
Measurement automation
Data processing automation
Programming
Software development

Technical skills

Microfabrication

Electron Beam lithography (CD 15nm)
Proximity effect correction
Optical lithography (CD 1um)
Mask design
Reactive ion etching (RIE)
Inductively coupled plasma etching (ICP)
Ion beam etching (IBE)
Wet etching
Electron beam evaporation
Atomic layer deposition (ALD)
Plasma enhanced chemical vapor deposition (PECVD)

Material Characterization

Scanning electron microscopy (SEM)
Focused ion beam (FIB)
Atomic force microscopy (AFM)
Optical microscopy

Electrical Device Characterization

Transistor and diode DC characterization
CV measurements
Pulsed characterization
Low level electrical measurements
Advanced Hall measurements
Cryogenic measurements

Scientific Software

Matlab
TCAD Silvaco Atlas
Comsol
NextNano
Origin
LEdit
Igor
LaTex

Programming

Labview (Core I, II, III)
C++
Java
Python

Soft Skills

team work, multicultural environments, interdisciplinary research, strong analytical and problem/solving skills, time management, multiple projects management, scientific communication (written and oral)

Languages

English (fluent), **French** (fluent), **German** (beginner), **Russian** (mother tongue)

Academic achievements

- *11 journal papers published + 3 submitted, 1 book chapter, 7 conference papers*
- *Grand Prix de Stage de Recherche (École Polytechnique)*
- 5 academic excellence scholarships

Publications

- **C. Erine**, L. Nela, A. Miranzadeh, E. Matioli "Analytical model for multi-channel high-electron-mobility III-N heterostructures", **Journal of Applied Physics**, 2021, under revision
- L. Nela, **C. Erine**, A. Miranzadeh, E. Matioli "Design of AlGaN/GaN Intrinsic Polarization Super Junction Devices", **Applied Physics Express**, 2021, under revision
- M. Zhu, **C. Erine**, J. Ma, M.S. Nikoo, L. Nela, P. Sohi, E. Matioli "p-GaN Tri-Gate MOS Structure for Normally-Off GaN Power Transistors", **IEEE Electron Device Letters**, 2021, v. 42, n. 1
- L. Nela, J. Ma, **C. Erine**, P. Xiang, T.-H. Shen, V. Tileli, T. Wang, K. Cheng, E. Matioli "Multi-channel nanowire devices for efficient power conversion", **Nature Electronics**, 2021, n. 4
- L. Nela, N. Perera, **C. Erine**, E. Matioli "Performance of GaN Power Devices for Cryogenic Applications down to 4.2K", **IEEE Transactions on Power Electronics**, 2021, v. 36, n. 7
- L. Nela, R. F. P. van Erp, N. Perera, **C. Erine**, E. Matioli "Impact of Embedded Liquid Cooling on the Electrical Characteristics of GaN-on-Si Power Transistors", **IEEE Electron Device Letters**, 2021, under revision
- **C. Erine**, J. Ma, G. Santoruvo, E. Matioli "Multi-channel AlGaN/GaN In-plane-gate Field-effect Transistors", **IEEE Electron Device Letters**, 2020, v. 41, n. 3
- J. Ma, **C. Erine**, M. Zhu, L. Nela, P. Xiang, K. Cheng, E. Matioli "1200V Multi-channel Power Devices with 2.8 Ohm mm ON-resistance", **IEEE International Electron Device Meeting**, 2019
- J. Ma, **C. Erine**, P. Xiang, K. Cheng, E. Matioli "Multi-channel tri-gate normally-on/off AlGaN/GaN MOSHEMTs on Si substrate with high breakdown voltage and low ON-resistance", **Applied Physics Letters**, 2019, v. 113, n. 24
- L. Nela, H. K. Yildirim, **C. Erine**, R. F. P. van Erp, P.Xiang, K. Cheng, E. Matioli "Conformal Passivation of Multi-Channel GaN Power Transistors for Reduced Current Collapse", **IEEE Electron Device Letters**, 2020, v. 42, n. 1
- M. S. Nikoo, G. Santoruvo, **C. Erine**, A. Jafari, E. Matioli "On the Dynamic Performance of Laterally Gated Transistors", **IEEE Electron Device Letters**, 2019, v. 40, n. 7
- M. Zhu, J. Ma, L. Nela, **C. Erine**, E. Matioli "High-voltage Normally-off Recessed Tri-gate GaN Power MOSFET with Low ON-resistance", **IEEE Electron Device Letters**, 2019, v. 40, n. 8
- J. M. George, D. Q. To, T. Huong Dang, **E. Erina**, T.L. Hoai Nguyen, H.J. Drouhin, H. Jaffrès "Tunneling Magnetoresistance, Spin Transfer and Spinorbitronics with (Ga, Mn)As", **Spintronics Handbook**, 2nd edition, CRC Press, 2019
- T. Huong Dang, D. Q. To, **E. Erina**, T.L. Hoai Nguyen, V.I. Safarov, H.J. Drouhin, H. Jaffrès "Theory of the Anomalous Tunnel Hall Effect at Ferromagnet-Semiconductor Junctions", **Journal of Magnetism and Magnetic Materials**, 2017, v. 459
- **E. Erina**,"On Partial Fourier-Haar Sums with Arbitrary Dilation Factor", **Mathematical Notes**, 2012, v. 92, n. 5

Associational activity

- **President of Student Scientific Association** (École Polytechnique) 2014 – 2016,
  Organization of scientific visits for students and scientific events for general public
- **Organization team of the International Natural Sciences Tournament** 2012 and 2013 (Saint Petersburg State University)
  Organization of accommodation and logistical support for a 100+ person event

Extracurricular activities

- Catamaran Sailing (member of Swiss Sailing, Voile Libre Morges)
- Radio Controlled Sailing (member of Swiss Sailing, VRC du Rosel)
- High-altitude trekking (expeditions in Altai and Caucasus mountains, Everest base camp, Annapurna circuit)

Personal details

Age: 29 years
Driving license: B, since 2009
In Switzerland: since 2017 (4 years)
Working permit: B (EU citizen)
Citizensips: French, Russian